POLITECNICO DI TORINO





Master's Degree in Mechanical Engineering

Investigation of Total Pressure Distortion Reconstruction Methods from Velocimetry Data

Double Degree Programme with Cranfield University
MSc Thermal Power and Propulsion

Prof. Teresa Maria Berruti **Marco Fasano**

Dr. Pavlos Zachos

Dr. Tommaso Piovesan

ANNO ACCADEMICO 2025-2026



Faculty of Engineering and Applied Sciences
Thermal Power and Propulsion – Power, Propulsion and the Environment

MSc

Academic Year 2025 - 2026

Marco Fasano

Investigations of total pressure distortion reconstruction methods from velocimetry data

Supervisor: Dr. Pavlos Zachos
Associate Supervisor: Dr. Tommaso Piovesan
September 2026

This thesis is submitted in partial fulfilment of the requirements for the degree of MSc Thermal Power and Propulsion

© Cranfield University 2026. All rights reserved. No part of this publication may be reproduced without the written permission of the copyright owner.

Academic integrity declaration

I declare that:

- the thesis submitted has been written by me alone.
- the thesis submitted has not been previously submitted to this university or any other.
- that all content, including primary and/or secondary data, is true to the best of my knowledge.
- that all quotations and references have been duly acknowledged according to the requirements of academic research.

I understand that to knowingly submit work in violation of the above statement will be considered by examiners as academic misconduct.

Abstract

Modern aviation relies on Very High Bypass Ratio engines with ultra-short intakes to maximise propulsive efficiency. These compact nacelles are susceptible to boundary layer separation and ground vortex ingestion during static crosswind operations, generating intense total-pressure distortion at the engine face. Conventional intrusive pressure rakes lack the spatial resolution to capture these compact, unsteady flow structures. This thesis evaluates the accuracy of mathematically reconstructing the total-pressure field from non-intrusive velocimetry data as a high-resolution alternative for assessing aerodynamic compatibility. The study analysed numerical velocity fields and experimental Stereoscopic Particle Image Velocimetry measurements from a scaled short intake model under crosswind. Total pressure was reconstructed using a Direct Spatial Integration scheme with compressibility corrections. These reconstructed fields were artificially undersampled to simulate varying physical rake configurations, comparing traditional distortion descriptors and aeromechanical excitation indices against full-resolution baselines. Analyses demonstrated that standard discrete arrays, such as an eight-by-five probe configuration, suffered from spatial aliasing. These sparse grids consistently failed to intersect compact ground vortices, masking spatial non-uniformities and underestimating peak structural forcing. The non-intrusive reconstruction resolved these critical aerodynamic features. However, the Direct Spatial Integration algorithm introduced a systematic mathematical offset, overestimating the distortion coefficient by margins. This artifact resulted from the radial inward integration mathematically smearing boundary pressure deficits. These findings indicate that velocimetry-based pressure reconstruction represents a conservative and superior diagnostic tool for evaluating off-design aerodynamic distortion. While the inherent numerical offset requires calibration for clean flow regimes, the non-intrusive approach successfully eliminates the spatial blind spots and aerodynamic blockages of traditional physical instrumentation.

Keywords:

Intake, PIV, DSI, Metrics, Recovery, Crosswind

Acknowledgements

I would like to express my sincere gratitude to my supervisors, Dr. Pavlos Zachos and Dr. Tommaso Piovesan, for providing me with the opportunity to work on this research project. Their invaluable guidance, sharp insights, and continuous support have been instrumental throughout the preparation of this thesis.

I am also deeply grateful for the Double Degree Agreement between Cranfield University and my home institution, Politecnico di Torino. This partnership gave me the extraordinary chance to study abroad and broaden my academic horizons.

To the wonderful friends I have made here in Cranfield, thank you for the unforgettable moments, the shared laughs, and the mutual support during this year. You have made this experience truly worthwhile and helped this campus feel like a second home.

My most heartfelt thanks goes to my parents. Thank you for your unending emotional support, your countless sacrifices, and your unconditional belief in my potential. I could never have reached this milestone without your constant encouragement and guidance.

Table of Contents

Academic integrity declaration i
Abstract ii
Acknowledgements iii
List of Figures vii
List of Tables xi
List of Equations xiii
List of Abbreviations xiv
1 INTRODUCTION 1
1.1 Project Background 1
1.2 Aims and Objectives 3
2 LITERATURE REVIEW 5
2.1 Aero-Engine Intake Aerodynamics and Integration 5
2.1.1 Very High Bypass Ratio Engines and Short Intakes 5
2.1.2 Crosswind Operation and Flow Separation 7
2.1.3 Ground Vortex Formation 9
2.2 Flow Distortion and Conventional Measurement Limitations 11
2.2.1 Total Pressure Distortion Metrics 11
2.2.2 Intrusive Measurement Techniques 12
2.2.3 Non-Intrusive Velocimetry 13
2.3 Pressure-from-Velocity Reconstruction Theory 15
2.3.1 Governing Equations 15
2.3.2 Direct Spatial Integration 16
2.3.3 Compressibility Corrections 18
2.3.4 Alternative Methods 19
2.4 Sensitivities and Uncertainties in Reconstruction Methods 21
2.4.1 Spatial Resolution Dependency 21
2.4.2 Influence of Boundary Conditions 22
2.5 Research Gaps 25
3 METHODOLOGY 27
3.1 Scarf and Droop Aero Pitot Intake Model Experimental Setup 27
3.2 Direct Spatial Integration 34
3.3 MIDAS 37
3.4 Distortion Coefficient *DC60* 39
3.5 Aeromechanics 42
3.5.1 Flow-Induced Vibrations and Harmonic Excitation Index 42
3.5.2 MIDAS Validation 43
3.6 Analysis of the Datasets 46
4 COMPUTED DATASET ANALYSIS 49
4.1 Flow Conditions 49
4.2 Undersampling of Ground Truth 50

4.2.1 Diffusion Driven Separation 50
4.2.2 Attached Flow 52
4.2.3 Shock Driven Separation 55
4.3 Influence of Spatial Resolution on CFD Ground Truth 59
4.3.1 Diffusion Driven Separation 59
4.3.2 Attached Flow 60
4.3.3 Shock Driven Separation 62
4.4 Pressure Reconstruction from RANS Velocity Field 64
4.4.1 Diffusion Driven Separation 64
4.4.2 Attached Flow 68
4.4.3 Shock Driven Separation 72
4.5 Influence of Boundary Conditions 77
4.5.1 Evenly Distributed Boundary Conditions 77
4.5.2 Unevenly Distributed Boundary Conditions 81
4.6 Resolution by Resolution Comparison: Ground Truth vs Reconstructed Pressure Field 86
4.6.1 Diffusion Driven Separation 86
4.6.2 Attached Flow 88
4.6.3 Shock Driven Separation 90
4.7 Real Case Simulation: Notional Physical Rake vs Reconstruction Method 93
4.7.1 Diffusion Driven Separation 93
4.7.2 Attached Flow 95
4.7.3 Shock Driven Separation 96
4.8 Conclusions about the DC60 Study on Reconstructed Flowfields 98
4.9 Aeromechanics 100
4.9.1 Influence of Low Resolution on CFD Ground Truth for HEI 100
4.9.2 HEI Comparison: Ground Truth vs Reconstructed Pressure Field 104
4.9.3 Real Case Simulation: Notional Physical Rake vs Reconstruction Methods 113
4.10 Conclusions Regarding the CFD Dataset 118
5 PARTICLE IMAGE VELOCIMETRY DATASET ANALYSIS 121
5.1 Time-Averaged PIV Dataset and Flow Conditions 121
5.2 PIV Reconstructed Pressure Field 123
5.2.1 Diffusion Driven Separation 123
5.2.2 Attached Flow 125
5.2.3 Shock Driven Separation 128
5.3 Influence of Boundary Conditions 132
5.4 Conclusions Regarding PIV Dataset 135
6 CONCLUSIONS 136
6.1 Summary of Findings 136
6.2 Recommendations for Future Research 138

References 139
Appendices 144
Appendix A Ethical approval letter 144
Appendix B Complete Pictures 145

List of Figures

Figure 3-1 Exploded CAD view of the LST intake model. *(Image copyright of NIFTI Consortium.)* 27

Figure 3-2 CAD image of the assembled LST intake model. *(Image copyright of NIFTI Consortium.)* 28

Figure 3-3 Boundary-layer trips with a 45◦ wedge angle placed on the outer intake surface. *(Images copyright of NIFTI Consortium.)* 29

Figure 3-4 Schematic of the DNW-LST wind tunnel test section with the intake model installed. (Image copyright of NIFTI Consortium.)..... 30

Figure 3-5 Wind tunnel set-up for crosswind testing with a ground plane: (a) side view of the wind tunnel test section with the model installed above the ground plane. (Images copyright of NIFTI Consortium.) 31

Figure 3-6 Camera PIV setup. 33

Figure 3-7 Total pressure probes on the instrumented rake at the intake exit section (black markers) and circumferential static pressure taps used as boundary conditions for the pressure from velocity reconstruction. 33

Figure 3-8 CFD ground truth SAE spreadsheet vs. MIDAS for three flow conditions. 44

Figure 3-9 Reconstructed Pressure Field SAE spreadsheet vs. MIDAS for three flow conditions. 44

Figure 3-10 Some of the grid resolutions used to downsample the full resolution. 47

Figure 4-1 The three different flow conditions which will be analysed, CFD ground truth. 49

Figure 4-2 CFD ground truth pressure field at different resolutions of rakes and rings. 50

Figure 4-3 Numerical and visual representation of DC60 behaviour at different undersampled resolutions. 51

Figure 4-4 CFD ground truth pressure field at different resolutions of rakes and rings. 53

Figure 4-5 Numerical and visual representation of DC60 behaviour at different undersampled resolutions. 55

Figure 4-6 CFD ground truth pressure field at different resolutions of rakes and rings. 56

Figure 4-7 Numerical and visual representation of DC60 behaviour at different undersampled resolutions. 57

Figure 4-8 Absolute Delta DC60 (Full resolution - Undersampled)..... 60

Figure 4-9 Absolute Delta DC60 (Full resolution - Undersampled)..... 62

Figure 4-10 Absolute Delta DC60 (Full resolution - Undersampled)..... 63

Figure 4-11 Real pressure field vs. Reconstructed pressure field. 65

Figure 4-12 CFD reconstructed pressure field at different resolutions of rakes and rings..... 66

Figure 4-13 Reconstructed flowfield DC60 behaviour. 67

Figure 4-14 Comparison between reconstructed flowfield DC60 and ground truth flowfield DC60. 67

Figure 4-15 Real pressure field vs. Reconstructed pressure field. 69

Figure 4-16 CFD Reconstructed pressure field at different resolutions of rakes and rings..... 70

Figure 4-17 Reconstructed flowfield DC60 behaviour. 72

Figure 4-18 Comparison between reconstructed flowfield DC60 and ground truth flowfield DC60. 72

Figure 4-19 Real pressure field vs. Reconstructed pressure field. 73

Figure 4-20 CFD reconstructed pressure field at different resolutions of rakes and rings..... 74

Figure 4-21 Reconstructed flowfield DC60 behaviour. 76

Figure 4-22 Comparison between reconstructed flowfield DC60 and ground truth flowfield DC60. 76

Figure 4-23 Comparative contours with varying probes number. 78

Figure 4-24 DC60 variation with evenly distributed BC probes. 79

Figure 4-25 Absolute Delta between partial BC configurations and the full set of 180 probes..... 80

Figure 4-26 Circumferential pressure gradient for each of the flow conditions. 81

Figure 4-27 Comparative contours with unevenly distributed BC probes. 83

Figure 4-28 DC60 variation with unevenly distributed BC probes. 84

Figure 4-29 Absolute Delta between partial uneven BC configurations and the full set of 180 probes..... 85

Figure 4-30 Absolute Delta DC60 resolution by resolution. Reconstructed flowfield DC60 - ground truth. 88

Figure 4-31 Absolute Delta DC60 resolution by resolution. Reconstructed flowfield DC60 - ground truth. 90

Figure 4-32 Absolute Delta DC60 resolution by resolution. Reconstructed flowfield DC60 - ground truth. 92

Figure 4-33 Absolute Delta DC60 real case simulation. Full resolution reconstructed flowfield DC60 - Undersampled ground truth. 94

Figure 4-34 Absolute Delta DC60 real case simulation. Full resolution reconstructed flowfield DC60 - Undersampled ground truth. 96

Figure 4-35 Absolute Delta DC60 real case simulation. Full resolution reconstructed flowfield DC60 - Undersampled ground truth. 97

Figure 4-36 HEI undersampled Ground truth vs. Full resolution Ground truth. 101

Figure 4-37 HEI undersampled ground truth vs. Full resolution ground truth. 102

Figure 4-38 HEI undersampled ground truth vs. Full resolution ground truth. 103

Figure 4-39 8x5 HEI analysis CFD ground truth vs reconstructed field. 105

Figure 4-40 8x10 HEI analysis CFD ground truth vs reconstructed field. 105

Figure 4-41 12x5 HEI analysis CFD ground truth vs reconstructed field. 106

Figure 4-42 12x10 HEI analysis CFD ground truth vs reconstructed field. 106

Figure 4-43 180x49 HEI analysis CFD ground truth vs reconstructed field. ... 107

Figure 4-44 8x5 HEI analysis CFD ground truth vs reconstructed field. 108

Figure 4-45 8x10 HEI analysis CFD ground truth vs reconstructed field. 108

Figure 4-46 12x10 HEI analysis CFD ground truth vs reconstructed field. 109

Figure 4-47 12x10 HEI analysis CFD ground truth vs reconstructed field. 109

Figure 4-48 180x49 HEI analysis CFD ground truth vs reconstructed field. ... 110

Figure 4-49 8x5 HEI analysis CFD ground truth vs reconstructed field. 111

Figure 4-50 8x10 HEI analysis CFD ground truth vs reconstructed field. 111

Figure 4-51 12x5 HEI analysis CFD ground truth vs reconstructed field. 111

Figure 4-52 12x10 HEI analysis CFD ground truth vs reconstructed field. 112

Figure 4-53 180x49 HEI analysis CFD ground truth vs reconstructed field. ... 112

Figure 4-54 Real Case simulation: Reconstruction vs 8x5 rake - Diffusion Driven Separation. 114

Figure 4-55 Real Case simulation: Reconstruction vs 12x5 rake - Diffusion Driven Separation. 114

Figure 4-56 Real Case simulation: Reconstruction vs 8x5 rake - Attached Flow. 116

Figure 4-57 Real Case simulation: Reconstruction vs 12x5 rake - Attached Flow. 116

Figure 4-58 Real Case simulation: Reconstruction vs 8x5 rake - Shock Driven Separation. 117

Figure 4-59 Real Case simulation: Reconstruction vs 12x5 rake - Shock Driven Separation. 118

Figure 5-1 Total pressure reconstructed flowfield at different resolutions - Diffusion Driven Separation. 124

Figure 5-2 Reconstructed flowfield DC60 – Diffusion Driven Separation. 125

Figure 5-3 DC60 comparison reconstruction vs. rakes – Diffusion Driven Separation. 125

Figure 5-4 Total pressure reconstructed flowfield at different resolutions – Attached Flow. 127

Figure 5-5 Reconstructed flowfield DC60 – Attached Flow. 128

Figure 5-6 DC60 comparison reconstruction vs. rakes – Attached Flow. 128

Figure 5-7 Total pressure reconstructed flowfield at different resolutions – Shock Driven Separation. 130

Figure 5-8 Reconstructed flowfield DC60 – Shock Driven Separation. 131

Figure 5-9 DC60 comparison reconstruction vs. rakes – Shock Driven Separation. 131

Figure 5-10 Comparative contours between full set of boundary conditions and partial set. 133

Figure 5-11 Boundary conditions influence on DC60. 134

List of Tables

Table 3-1 Working conditions for both the datasets. 46

Table 4-1 ground truth DC60. 50

Table 4-2 ground truth DC60. 54

Table 4-3 ground truth DC60. 56

Table 4-4 Absolute Delta DC60 (Full Resolution - Undersampled). 60

Table 4-5 Absolute Delta DC60 (Full Resolution - Undersampled). 61

Table 4-6 Absolute Delta DC60 (Full Resolution - Undersampled). 62

Table 4-7 Comparison between reconstructed flowfield DC60 and ground truth flowfield DC60. 66

Table 4-8 Comparison between reconstructed flowfield DC60 and ground truth flowfield DC60. 71

Table 4-9 Comparison between reconstructed flowfield DC60 and ground truth flowfield DC60. 75

Table 4-10 DC60 variation with evenly distributed BC probes..... 79

Table 4-11 Absolute Delta between partial BC configurations and the full set of 180 probes..... 79

Table 4-12 BC probes angular position. 82

Table 4-13 DC60 variation with unevenly distributed BC probes..... 84

Table 4-14 Absolute Delta between partial uneven BC configurations and the full set of 180 probes. 84

Table 4-15 Absolute Delta DC60 resolution by resolution. Reconstructed flowfield DC60 - ground truth. 87

Table 4-16 Absolute Delta DC60 resolution by resolution. Reconstructed flowfield DC60 - ground truth. 89

Table 4-17 Absolute Delta DC60 resolution by resolution. Reconstructed flowfield DC60 - ground truth. 91

Table 4-18 Absolute Delta DC60 real case simulation. Full resolution reconstructed flowfield DC60 - Undersampled ground truth. 94

Table 4-19 Absolute Delta DC60 real case simulation. Full resolution reconstructed flowfield DC60 - Undersampled ground truth. 95

Table 4-20 Absolute Delta DC60 real case simulation. Full resolution reconstructed flowfield DC60 - Undersampled ground truth. 97

Table 5-1 DC60 comparison reconstruction vs. rakes – Diffusion Driven Separation. 124

Table 5-2 DC60 comparison reconstruction vs. rakes – Attached Flow. 127

Table 5-3 DC60 comparison reconstruction vs. rakes – Shock Driven Separation. 130

Table 5-4 Boundary condition influence on DC60. 133

List of Equations

(2-1)..... 7
(2-2)..... 11
(2-3)..... 11
(2-4)..... 15
(2-5)..... 16
(3-1)..... 34
(3-2)..... 35
(3-3)..... 36
(3-4)..... 39
(3-5)..... 40
(3-6)..... 41
(3-7)..... 43
(3-8)..... 43
(3-9)..... 43
(4-1)..... 81
(4-2)..... 81

List of Abbreviations

VHBPR	Very-High Bypass Ratio
UHBPR	Ultra-High Bypass Ratio
MFCR	Massflow Capture Ratio
S-PIV	Stereoscopic Particle Image Velocimetry
DSI	Direct Spatial Integration
PPE	Poisson Pressure Equation
AIP	Aerodynamic Interface Plane
$DC60$	Distortion Coefficient
L_i	Nacelle length
Di	Inner diameter
p	Static Pressure
p_0	Total Pressure
M	Mach Number
MIDAS	Modular Intake Distortion Analysis Software
EO	Engine Order
DFT	Discrete Fourier Transform
a_n and b_n	Fourier Coefficients
V_n	Absolute Forcing Vector Magnitude
HEI	Excitation Index
BC	Boundary Condition

1 INTRODUCTION

1.1 Project Background

The commercial aviation industry is increasingly driven by stringent environmental targets demanding drastic reductions in fuel burn, noise, and emissions. To achieve these goals, engine manufacturers are shifting toward Very High Bypass Ratio and Ultra High Bypass Ratio turbofan engines. While these engines significantly increase propulsive efficiency, their larger fan diameters introduce integration challenges by increasing the nacelle's overall wetted area, aerodynamic drag, and powerplant weight. To mitigate these penalties and fully realise the benefits of VHBPR architectures, the industry must transition toward compact nacelles featuring ultrashort intakes.

However, shortening the intake nacelle introduces profound aerodynamic challenges. Compact intakes possess a diminished internal diffusion capability, rendering them highly susceptible to boundary layer separation. This vulnerability is particularly critical during off-design operating conditions, such as static or low-speed ground operations under strong crosswinds. The aggressive turning of the airflow around the intake lip can induce severe flow separation and ingest powerful ground vortices. These phenomena generate severe total-pressure and swirl distortion at the Aerodynamic Interface Plane, which can severely compromise fan operability, reduce stability margins, and provoke aero-mechanical vibrations.

Assessing the aerodynamic compatibility between an aero-engine and its intake requires accurately characterising the non-uniform flow at the AIP. The problem this project aims to solve is pressure measurement at this critical interface. The current industry standard mostly relies on intrusive measurement techniques, specifically the installation of physical total-pressure sensor rakes, commonly employing an 8-rake by 5-ring configuration of probes.

This conventional methodology suffers from severe limitations when applied to the complex, unsteady flows typical of modern compact intakes. Physical rakes are inherently intrusive. Their physical presence introduces

aerodynamic blockage that can significantly alter the delicate flow characteristics they are intended to measure. To avoid unacceptably disrupting the flow, the number of sensors is strictly limited, resulting in low spatial and temporal resolutions. These sparse discrete points often fail to capture the full spatial complexity of the flow field, completely missing highly localised separations or the sharp pressure gradients of an ingested ground vortex.

To overcome the limitations of intrusive physical probes, the aerospace industry is increasingly turning to advanced non-intrusive methods like Stereoscopic Particle Image Velocimetry. S-PIV can capture the instantaneous velocity field across the entire annulus without introducing aerodynamic blockages, achieving a spatial resolution that is 200 to 300 times richer than traditional rakes.

Because the industry still requires pressure data to assess stability using standardised descriptors like the $DC60$, this project will use pressure reconstruction from S-PIV velocity data. By mathematically deriving the pressure fields from velocity measurements, this approach removes the need for intrusive rakes while capturing the true severity of flow non-uniformities. Ultimately, this research will analyse the influence of measurement resolution on distortion metrics, specifically comparing reconstructed flowfields to notional physical rakes via the $DC60$, to bridge the gap between modern optical diagnostics and established industrial standards.

1.2 Aims and Objectives

The primary aim of this research is to evaluate the feasibility and accuracy of reconstructing the total-pressure flow field at the Aerodynamic Interface Plane from non-intrusive velocity measurements in a short aero-engine intake operating under crosswind conditions. Ultimately, this project seeks to determine whether pressure-from-velocity reconstruction can serve as a reliable, high-resolution alternative to conventional intrusive pressure rakes for assessing intake-engine aerodynamic compatibility. To successfully achieve this aim, the research addresses several core objectives organised into sequential phases of implementation, analysis, and practical demonstration.

Implementation and Validation of Reconstruction Techniques

The first objective is to apply pressure-from-velocity reconstruction methods, specifically the DSI scheme with compressibility corrections. This phase uses high-fidelity numerical velocity data (RANS) as a baseline to compute both the static and total pressure fields at the AIP, ensuring the foundational methodology is sound.

Analysis of Spatial Resolution on Distortion Metrics

Building on the validated techniques, the research will systematically quantify how spatial undersampling affects the accuracy of critical distortion metrics. By comparing descriptors derived from full-resolution reconstructed fields against artificially undersampled grids, this phase evaluates impacts on key indicators, particularly the Distortion Coefficient $DC60$ and the aeromechanical Harmonic Excitation Index HEI.

Evaluation of Notional Physical Rakes

To ground the research in real-world testing scenarios, the study will compare the distortion metrics captured by simulated standard industrial rakes directly against the full-resolution pressure reconstructions. This objective will be rigorously tested across distinct operational regimes, including diffusion-driven separation, attached flow, and shock-driven separation.

Assessment of Boundary Condition Impacts

Parallel to the evaluation of testing hardware, the research investigates the sensitivity of the pressure reconstruction accuracy to its boundary inputs. This involves assessing the spatial distribution, quantity, and interpolation methods of the wall static pressure probes used as boundary conditions for the DSI algorithm.

Application on Experimental S-PIV Data

Finally, the project will apply the validated reconstruction methodology to experimental S-PIV datasets. This crucial step verifies the technique's capability to capture complex, highly localised flow features, such as ingested ground vortices, that sparse physical rakes inherently fail to resolve, thereby demonstrating the practical superiority of the proposed approach.

2 LITERATURE REVIEW

2.1 Aero-Engine Intake Aerodynamics and Integration

2.1.1 Very High Bypass Ratio Engines and Short Intakes

The commercial aviation industry is increasingly driven by stringent environmental and economic targets, such as the ACARE Flightpath 2050 goals, which demand drastic reductions in fuel burn, noise, and emissions [1]. To achieve these targets, engine manufacturers are shifting toward VHBPR and UHBPR [1]. By increasing the bypass ratio to values exceeding 15 and reducing the fan pressure ratio to below 1.4, these engines significantly increase propulsive efficiency and decrease specific fuel consumption [1]. Advanced architectures, such as geared turbofans, further enable these improvements by allowing the large-diameter fan and the low-pressure turbine to operate at their respective optimum rotational speeds, which limits fan tip speeds while achieving substantial noise reductions and optimal stage counts [1].

Despite the clear thermodynamic advantages of VHBPR engines, the requisite increase in fan diameter introduces significant aircraft integration challenges [2]. The larger engine size directly translates to a larger nacelle wetted area, which subsequently increases both aerodynamic drag and overall powerplant weight [2]. Studies have indicated that the aerodynamic drag and weight penalties associated with installing a conventionally proportioned nacelle on an ultra-high bypass engine can erode or even entirely offset the fuel savings provided by the advanced engine cycle [1]. Consequently, to fully realise the benefits of VHBPR engines, the industry must transition toward highly compact nacelles featuring ultrashort intakes [1]. While state-of-the-art intakes typically exhibit length-to-fan-diameter ratios between 0.5 and 0.65, future compact designs aim to reduce this ratio considerably below 0.5, and potentially as low as 0.25 to 0.4 [1].

Shortening the intake nacelle introduces profound aerodynamic challenges, primarily because the incoming airflow must be turned and diffused over a significantly reduced axial distance [3]. Compact intakes possess a

diminished internal diffusion capability, rendering them highly susceptible to boundary layer separation [1]. This vulnerability is particularly acute during off-design operating conditions, such as high angle-of-attack climbs or strong crosswinds, where aggressive streamline curvature around the inlet lip can induce supersonic over-speeds, shock waves, or severe diffusion-driven separation [1]. When flow separation occurs, it generates severe total pressure and swirl distortion at the aerodynamic interface plane [3]. Because the short duct lacks the length required to naturally attenuate these flow non-uniformities, the engine face is subjected to highly distorted airflow, which can severely compromise fan operability, reduce stability margins, and provoke aero-mechanical vibrations in the lightweight composite blades expected in future engines [3].

The reduced physical distance between the intake lip and the fan face in compact nacelles significantly amplifies the aerodynamic coupling between these two components [4]. Traditional intake design methodologies are often inadequate for short nacelles because the fan actively redistributes the upstream mass flux and alters the intake's separation characteristics [5]. While the fan's suction effect can favourably delay the onset of lip separation that would otherwise occur in an isolated intake [6], the unsteady pressure field and upstream-traveling perturbations from the fan blades can also destabilise the intake boundary layer, causing earlier flow separation under crosswind conditions [7]. Furthermore, a critical limiting mechanism in short intake design is the generation of high streamwise Mach numbers near the fan shroud [8]. Because a short inlet often lacks a distinct throat and the effective flow area continuously decreases up to the fan face, the flow continuously accelerates [8]. This local over-speed causes the rotor to operate close to a choked condition, imposing severe penalties on fan efficiency and eroding the anticipated propulsive benefits of the VHBPR architecture [8].

In addition to internal flow challenges, shortening the nacelle dramatically affects external aerodynamics during high-speed cruise [2]. To accommodate the necessary engine subsystems within a shorter axial length, the external fan cowl

must exhibit a higher degree of curvature [2]. This elevated curvature induces a rapid acceleration of the external flow, leading to higher peak Mach numbers over the nacelle forebody [9]. During transonic cruise, this acceleration can trigger the formation of strong shock waves on the nacelle's outer surface, resulting in severe wave drag penalties [10]. Consequently, the aerodynamic design of short nacelles represents a highly constrained multi-point optimisation problem [2]. Designers must carefully balance the competing requirements of maintaining a slender external profile to minimise wave drag at transonic cruise, while simultaneously providing sufficient inlet lip thickness and internal diffusion capability to prevent flow separation during low-speed, high-incidence operations [1].

2.1.2 Crosswind Operation and Flow Separation

During crosswind operations, particularly during static or low-speed ground conditions, a compact intake must capture and turn a large streamtube of air that often intersects with the ground plane [11]. This aggressive turning process generates significant streamline curvature and an asymmetrical flow field [12]. The interaction between the crosswind, the ground, and the engine's suction leads to the formation of a powerful ground vortex and an associated trailing vortex system on the leeward side of the intake, which are subsequently ingested by the engine [11]. In addition to these vortical structures, the crosswind flow must rapidly accelerate around the windward intake lip, rendering the boundary layer highly susceptible to severe separation [13]. Because the non-axisymmetric geometry of the intake, such as droop and scarf angles, interacts with the ground effect, this separation is typically biased toward the top half of the AIP on the windward side [3].

At a constant crosswind velocity, the aerodynamic behaviour of the intake is heavily dictated by the engine's mass flow rate, commonly expressed as the Mass Flow Capture Ratio [3].

$$MFCR = \frac{A_\infty}{A_{hi}} = \frac{\dot{m}}{\rho_\infty V_\infty A_{hi}} \quad \textbf{(2-1)}$$

Where ρ_∞ is the freestream air density and A_{hi} the intake highlight area [14]. As the mass flow rate increases, the intake flow transitions through three distinct, highly complex aerodynamic regimes: diffusion-driven separation, attached flow, and shock-induced separation [3].

2.1.2.1 Diffusion-Driven Separation

At low mass flow rates, the intake operates in a regime characterised by diffusion-driven separation [3]. Under these conditions, the flow decelerates strongly after passing the intake lip, but the peak isentropic Mach numbers on the intake surface remain entirely subsonic [15]. The subsequent adverse pressure gradient within the internal diffuser is too steep for the boundary layer to negotiate, causing it to detach and form a massive area of reversed flow on the windward side [15]. This separation creates a profound axial velocity deficit that extends over a large portion of the AIP, frequently covering up to 25% to 30% of the plane's radius and exhibiting a very wide circumferential footprint [3]. Because of this widespread flow blockage, diffusion-driven separation generates exceptionally high levels of time-averaged and peak swirl distortion, creating extensive regions of positive incidence angle variations at the fan face that pose a severe threat to fan operability and stability [3].

2.1.2.2 Attached Flow

As the mass flow rate is increased to intermediate values, the flow transitions into the attached flow regime [3]. In this optimal state, the size of the distorted region noticeably shrinks until the boundary layer fully reattaches to the lip and diffuser surfaces [3]. The flow arriving at the engine face remains mostly uniform and stable, with minor incidence angle variations [3]. In this regime, the primary source of flow distortion is no longer lip separation, but rather the localised influence of the counter-rotating ground vortex near the bottom of the intake [3].

2.1.2.3 Shock-Induced Separation

As the mass flow rate is further increased to high values, the extreme suction requirements force the incoming crosswind to accelerate so rapidly

around the windward lip that it reaches local supersonic velocities [15]. This localised supersonic patch terminates in a strong shock wave, which triggers a shock-induced separation of the boundary layer [15]. While this separation introduces sharp total pressure losses, its spatial topology at the AIP is fundamentally different from the diffusion-driven case [3]. Shock-induced separation tends to be tightly localised near the outer surface of the intake duct, closely following the origination point of the shock wave [3]. Consequently, it affects a significantly smaller radial and circumferential extent of the aerodynamic interface plane [3]. Although the shock wave introduces substantial flow unsteadiness and localised high-swirl regions, its reduced spatial footprint generally poses a comparatively lower overall risk of sustained rotor stall than the massive flow blockages created by diffusion-driven separation [3].

2.1.3 Ground Vortex Formation

When an aero-engine operates at high power during static or low-speed ground conditions, the intake's capture streamtube enlarges sufficiently to intersect with the ground surface [3]. This interaction creates a stagnation point on the ground where airflows converging from multiple directions meet [16]. Due to the intense suction of the engine, the flow turns and accelerates, concentrating ambient vorticity and vorticity generated along the intake's outer surface into a powerful swirling motion [3]. This swirling flow is stretched and drawn upward, entering the engine as a ground vortex [16]. Under crosswind conditions, this dynamic typically manifests as a single, intensely powerful vortex accompanied by a trailing vortex system on the leeward side of the nacelle [17].

The ingested ground vortex is an exceptionally compact and highly localised flow structure, typically occupying an area more than an order of magnitude smaller than the intake's inner cross-section [3]. Despite its small physical footprint, the vortex core harbours intense tangential velocities and sharp total-pressure deficits that can easily exceed 15%, creating extreme, localised flow distortion at the aerodynamic interface plane [3]. Because this vortex is highly unsteady, oscillating in response to the surrounding flow field, conventional intrusive measurement techniques like pressure rakes are vastly

inadequate [3]. Physical probes lack the necessary spatial and temporal resolution to resolve the tiny vortex core and can actually alter the delicate, complex flow patterns they are meant to measure [3].

Consequently, accurately capturing the intricate dynamics and sharp pressure gradients of the ground vortex requires advanced, high-resolution non-intrusive diagnostic tools, such as Stereoscopic Particle Image Velocimetry [3]. By providing thousands of simultaneous velocity vectors across the measurement plane, these high-fidelity techniques capture the exact spatial footprint of the vortex core, enabling designers to properly quantify the highly localised distortion events that pose severe risks to fan operability, blade stability, and foreign object ingestion [3].

2.2 Flow Distortion and Conventional Measurement Limitations

2.2.1 Total Pressure Distortion Metrics

The aerodynamic compatibility between an aero-engine and its intake is evaluated by characterising the flow at the AIP, which is a designated measurement cross-section located just upstream of the engine's fan or compressor face [18]. Because non-uniform airflow can severely compromise the performance and structural integrity of the engine's compression system, industry practice relies on specific numerical metrics to quantify the magnitude of flow distortion [3]. These metrics are derived from pressure data conventionally acquired using an array of probes arranged in a ring-and-rake configuration across the AIP [3]. Two of the most critical metrics used to assess this compatibility are the Intake Pressure Recovery and the Distortion Coefficient $DC60$.

$$IPR = \frac{\overline{p_{0\,AIP}}}{P_{0\,\infty}} \tag{2-2}$$

$$DC60 = \frac{\overline{p_{0\,AIP}} - \overline{p_{0\,60°}}}{\overline{q_{AIP}}} \tag{2-3}$$

Where $\overline{p_{0\,AIP}}$ is the area-averaged total pressure at the AIP, $P_{0\,\infty}$ denotes the freestream total pressure, $\overline{p_{0\,60°}}$ is the area averaged total pressure in the most distorted sector of 60° extent, and $\overline{q_{AIP}}$ is the area-averaged dynamic pressure at the AIP. Both metrics, IPR and $DC60$, were computed using an area-average method based on a ring-rake approach, following industrial practice [19].

The IPR serves as a fundamental measure of the intake's aerodynamic efficiency by quantifying the overall total-pressure loss. It is mathematically defined as the ratio of the area-averaged total pressure at the AIP to a reference total pressure, which is typically the freestream total pressure [3]. Essentially, the IPR indicates how much of the ambient free-stream stagnation pressure is successfully retained after the air has navigated the intake duct [1]. A lower IPR signifies greater total pressure losses, which are generally caused by entropy-

increasing phenomena such as boundary layer friction, shock waves, or severe flow separation [18].

While the IPR provides a macro-level view of pressure retention, it does not describe the spatial uniformity of the flow. For this, it's common to rely on the Distortion Coefficient, commonly referred to as $DC60$ [3]. Originally developed by Rolls-Royce, DC60 is a widely adopted industry standard used to measure the intensity of circumferential total-pressure distortion [20]. It specifically targets the most severely distorted region of the flow that is likely to trigger rotating stall or engine surge [3]. $DC60$ is calculated as the difference between the area-averaged total pressure across the entire AIP and the lowest average total pressure found within any 60-degree circumferential sector, with this difference subsequently normalised by the area-averaged dynamic pressure at the AIP [3]. By isolating the worst 60-degree sector, the $DC60$ metric provides a direct numerical indicator of peak spatial non-uniformity, which can then be compared against the specific distortion tolerance thresholds of the downstream aero-engine to ensure safe and stable operation [3].

2.2.2 Intrusive Measurement Techniques

The industry standard for evaluating intake-engine aerodynamic compatibility and quantifying flow distortion relies heavily on intrusive measurement techniques, specifically the installation of total-pressure and temperature sensor rakes at the AIP [3]. A conventional rake arrangement typically consists of an array of eight equally spaced rakes, each equipped with five or ten probes positioned at the centre of equal-area rings to capture the flow properties [18]. Because these discrete measurement points provide a sparse representation of the flow field, the acquired data can be linearly interpolated and area-averaged onto a denser polar grid, such as a *24x10* matrix, to calculate standardised distortion descriptors like the $DC60$ [3].

While this methodology is well-established for steady-state distortion assessment, it suffers from severe limitations when applied to the highly complex, unsteady flows typical of modern compact intakes. The primary drawback of

instrumented rakes is their inherently intrusive nature. Inserting physical probes and their supporting structures directly into the intake duct can significantly alter the very flow characteristics they are intended to measure [21]. The physical presence of the rakes introduces aerodynamic blockage, which strictly limits the maximum number of sensors that can be safely installed without unacceptably disrupting the flow or reducing engine performance. Furthermore, in regions where separated flow or vortical structures are present, the probes can distort the local flow patterns, leading to inherent measurement inaccuracies [3].

The restriction on sensor density results in exceptionally low spatial and temporal resolution compared to advanced non-intrusive optical methods like Stereoscopic Particle Image Velocimetry [18]. An *8x10* rake array provides only 80 discrete data points, which is frequently insufficient to capture the full spatial complexity of intake flow fields that feature highly localised separations and intense swirl [3]. This limitation becomes particularly critical when attempting to resolve small-scale, dynamic flow features such as the ingested ground vortex.

Because the ground vortex is a highly compact structure characterised by sharp, severe total-pressure deficits, the sparse grid of a conventional rake system can easily miss the vortex core entirely or fail to accurately resolve its steep pressure gradients [3]. Interpolating data from 80 points to a 24x10 grid cannot recreate the physical phenomena lost in the gaps between the physical probes. Consequently, relying solely on intrusive rake data can lead to a significant underestimation of peak distortion events, leaving the true magnitude of total-pressure loss and the dynamic, meandering behaviour of the ground vortex inadequately characterised [3].

2.2.3 Non-Intrusive Velocimetry

To overcome the severe limitations of intrusive physical probes, the aerospace industry has increasingly turned to S-PIV as the modern standard for advanced flow diagnostics [3]. As a laser-optical measurement technique, S-PIV is inherently non-intrusive, enabling the capture of the full complexity of the flow field without introducing aerodynamic blockages or altering the delicate flow structures they are trying to measure. This is achieved by seeding the airflow with

microscopic tracer particles and illuminating the target cross-section with pulsed laser sheets [3]. Multiple digital cameras, positioned at off-axis angles to mimic human binocular vision, record the instantaneous displacement of these particles, enabling the precise calculation of all three velocity components across the entire measurement plane [3].

The most profound advantage of S-PIV over traditional rake arrangements is its massive increase in spatial resolution. While a conventional *8x10* pressure rake provides only 80 discrete data points, a modern multi-camera S-PIV setup can generate upwards of 18000 simultaneous three-dimensional velocity vectors across the AIP. This yields a spatial resolution that is 200 to 300 times richer than that of traditional intrusive instrumentation, with vector spacings as fine as 1.5 millimetres [3].

This high-fidelity, synchronous data is crucial for assessing dynamic flow distortion in modern compact intakes. Because S-PIV captures the instantaneous velocity field across the entire annulus simultaneously, it can successfully resolve the highly localised and unsteady phenomena that physical rakes miss. It provides the necessary spatial density to accurately capture the sharp, steep velocity gradients of a ground vortex, as well as the topologies of diffusion-driven or shock-induced lip separations [3]. Furthermore, this rich, high-resolution velocity data serves as the critical foundation for advanced mathematical post-processing, enabling the reliable reconstruction of the instantaneous total-pressure fields and unsteady swirl metrics without ever disturbing the flow [3].

2.3 Pressure-from-Velocity Reconstruction Theory

2.3.1 Governing Equations

The extraction of pressure fields from measured velocity data relies on the fundamental physical relationship between these fluid properties, which is governed by the Navier-Stokes momentum equations [22]. When the velocity field is obtained experimentally, such as through PIV, the pressure becomes the primary unknown that can be deduced analytically by rearranging these governing fluid dynamics equations [23].

For an incompressible flow with constant density, the Navier-Stokes momentum equation can be arranged to isolate the pressure gradient. In this configuration, the pressure gradient ∇p is expressed as a balance against the fluid's acceleration and viscous forces [24]:

$$\nabla p = -\rho\left(\frac{\partial u}{\partial t} + (u \cdot \nabla)u\right) + \mu\nabla^2 u \quad \textbf{(2-4)}$$

In this expression, represents the fluid density, is the velocity vector, is time, and is the dynamic viscosity. The terms on the right side of the equation represent the local acceleration $\left(\frac{\partial u}{\partial t}\right)$, the convective acceleration $\left((u \cdot \nabla)u\right)$, and the viscous diffusion $(\mu\nabla^2 u)$. The combined sum of the local and convective accelerations is known as the material acceleration, which characterises the time rate of change of the velocity evaluated along the trajectory of a moving fluid particle [25].

In many fluid dynamics applications involving high Reynolds number flows, typically where $Re > 10^3$, the inertial forces strongly dominate the viscous forces in regions away from solid boundaries. Under these conditions, the viscous diffusion term is negligibly small and can be safely omitted from the calculation. Consequently, the pressure gradient becomes directly proportional to the material acceleration, allowing the calculation of the pressure gradient field purely

from the spatial and temporal derivatives of the measured velocity field combined with the fluid density [3].

Once the pressure gradient vector field is established, the pressure distribution itself is typically reconstructed using two primary mathematical techniques. The first technique is Direct Spatial Integration or DSI. Because the momentum equation describes a conservative vector field that is equal to the gradient of a potential function, which is the pressure, integrating the calculated pressure gradients along spatial paths across the flow domain results in the relative pressure differences [23].

The second fundamental approach involves solving the Poisson Pressure Equation or PPE. This equation is analytically derived by applying the mathematical divergence operator to the Navier-Stokes momentum equation [23]. By applying the incompressible continuity equation ($\nabla \cdot u = 0$), the viscous and temporal derivative terms are eliminated [26]. As a result, the Poisson equation simplifies to a form where the Laplacian of the pressure ($\nabla^2 p$) is entirely dictated by the divergence of the convective acceleration [23]:

$$\nabla^2 p = -\rho \nabla \cdot \big((u \cdot \nabla) u\big) \quad \textbf{(2-5)}$$

This transforms the pressure calculation into a boundary value problem, allowing the pressure field to be resolved globally across the domain provided that appropriate Dirichlet or Neumann boundary conditions are supplied in the form of known pressure or pressure gradient [23].

2.3.2 Direct Spatial Integration

The DSI method reconstructs the instantaneous pressure field by directly integrating the spatial pressure gradients derived from the Navier-Stokes momentum equations [18]. Unlike techniques that solve the Poisson Pressure Equation, the DSI method relies strictly on the spatial and temporal derivatives of the measured velocity field to deduce these gradients [3].

To perform this integration across a discretised measurement plane, such as a polar grid representing an engine intake, a space-marching technique is

conventionally employed [18]. The integration process fundamentally begins at the external boundary of the domain, where a known circumferential static-pressure distribution must be prescribed as a Dirichlet boundary condition [27]. Using this known boundary as the starting reference, the calculation iteratively proceeds radially inward toward the centre of the grid [18].

The mathematical core of this inward-marching process, often adapted from the method originally proposed by Baur and Köngeter, involves calculating the unknown static pressure at an internal node using the previously determined pressure values of its adjacent neighbours. The pressure at the target node is evaluated as the average of the integrated pressures from four neighbouring points [18]. To calculate the pressure contribution from each adjacent node, the algorithm uses a first-order Taylor polynomial. This polynomial determines the local pressure increment by multiplying the spatial pressure gradients which were already extracted from the velocity field, by the specific grid spacing in the radial and circumferential directions [3]. By averaging the results of these short integration paths from multiple adjacent nodes, the DSI scheme attempts to smooth out local uncertainties and measurement noise embedded in the velocity data [18].

However, because standard space-marching integration is highly susceptible to cumulative error propagation as it moves inward from the boundary, advanced forms of DSI known as omnidirectional integration have been developed. Methods such as the Circular Virtual Boundary or Rotating Parallel Ray algorithms establish virtual boundaries outside the actual flow domain to generate a dense, multi-directional network of integration guidelines [28]. The physical integration still starts and stops at the real domain boundaries, traveling in a "zig-zag" fashion along the real nodal points that lie closest to these virtual guidelines [29]. Every time an integration path crosses a specific internal node, the calculated pressure value is deposited into a data bin associated with that node [28]. Once all paths have been traced, the final pressure at any internal location is determined by averaging all the accumulated values within its bin. By effectively gathering pressure integrations from all possible directions with equal

weighting, this advanced DSI approach significantly minimises the influence of localised errors in the measured pressure gradient, providing a highly robust reconstruction of the pressure field [28].

2.3.3 Compressibility Corrections

The extraction of pressure from measured velocity fields conventionally relies on the assumption of constant fluid density, a simplification that is generally valid for low-speed flows where the Mach number remains below 0.3 [18]. However, as discussed in the context of compact intakes operating under severe crosswind conditions, high mass flow rates and MFCR force the incoming air to rapidly accelerate around the windward intake. This aggressive turning frequently pushes local velocities into the supersonic regime, terminating in strong shock waves and shock-induced boundary layer separation at the lip [3]. Under these high-speed conditions, the fundamental assumption of incompressibility completely fails because the isentropic flow assumption is severely violated in regions affected by shock waves and highly viscous shear layers [30]. Consequently, attempting to reconstruct the pressure field without accounting for compressibility at high MFCR values leads to substantial inaccuracies, particularly in the undisturbed, high-speed regions of the aerodynamic interface plane [14]. These density-related inaccuracies propagate directly into the calculation of critical distortion metrics, causing significant errors when evaluating total pressure deficits and overall distortion coefficients during shock-induced separation events [14].

To restore the accuracy of the DSI method in these highly compressible regimes, additional thermodynamic relations must be incorporated to model the variable density [30]. While one theoretical approach involves using the differential continuity equation to derive density directly from spatial velocity gradients, this method is highly sensitive to measurement noise and out-of-plane velocity errors, causing inaccuracies to rapidly accumulate along streamlines and disrupting the density computation. Instead, a more robust and widely adopted approach relies on combining the ideal gas law with the assumption of adiabatic flow [18].

By assuming that the total enthalpy remains constant throughout the flow field, the local static temperature can be mathematically expressed as a function of a known reference total temperature and the measured local velocity magnitude [31]. The ideal gas law is then used to substitute the density term in the Navier-Stokes momentum equations with this derived temperature relationship and the local static pressure. This elegant substitution allows the density to be evaluated dynamically at each grid node as a function of pressure and velocity [31]. Crucially, by manipulating these governing equations into a non-conservative form using the natural logarithm of pressure, the resulting pressure-integration procedure retains a fundamentally similar mathematical structure to the standard incompressible DSI algorithm [18].

Once the corrected static pressure field is obtained via this modified DSI integration, the total pressure field is subsequently calculated using standard compressible isentropic relations that incorporate the local Mach number and the ratio of specific heats [3]. Literature demonstrates that applying this specific compressibility correction to the DSI method significantly improves the accuracy of both the reconstructed pressure fields and the derived distortion descriptors across the entire engine operating range, successfully mitigating the extreme errors that would otherwise occur during high-speed, shock-induced separation [3].

2.3.4 Alternative Methods

While the Direct Spatial Integration method reconstructs the pressure field by evaluating and integrating pressure gradients along discrete spatial paths, the PPE approach takes the mathematical divergence of the momentum equations to formulate a global, elliptic boundary value problem [3]. Solving the PPE effectively acts as a global optimisation of the pressure-gradient field [24]. Because the PPE relies on the Laplacian operator, it inherently smooths out localised random measurement noise across the entire domain [32]. However, this global solution requires rigorous, well-defined Dirichlet or Neumann boundary conditions along the entirety of the domain's contour, whereas spatial integration only requires a known pressure reference at the starting boundaries [30].

Despite the mathematical elegance and global smoothing advantages of the PPE method, DSI is specifically preferred for studies involving high mass flow rates and compressibility effects due to the numerical limitations associated with the PPE. Attempting to adapt the Poisson Pressure Equation to account for variable fluid density introduces significant mathematical and numerical impracticalities [18]. In contrast, the DSI method can easily accommodate compressibility corrections by incorporating the ideal gas law and adiabatic flow assumptions [33]. By expressing the local density as a function of the derived temperature and static pressure, the DSI governing equations can be algebraically manipulated into a non-conservative form using the natural logarithm of pressure [18]. This strategic transformation retains a fundamentally similar algorithmic structure to the standard incompressible DSI scheme, making it a highly practical and robust choice for evaluating the complex, variable-density flows associated with shock-induced separations [18].

2.4 Sensitivities and Uncertainties in Reconstruction Methods

2.4.1 Spatial Resolution Dependency

The accuracy of pressure fields and distortion metrics reconstructed from PIV data is highly sensitive to the spatial resolution of the velocity measurements [23]. Existing literature demonstrates a complex trade-off between numerical truncation errors and the propagation of experimental velocity noise, which ultimately dictates an optimal spatial resolution for pressure reconstruction [23]. Studies analysing the error propagation dynamics have shown that when the spatial resolution is too coarse, numerical truncation errors dominate because finite-difference schemes fail to accurately approximate the underlying, sharp spatial gradients of the flow [26]. Conversely, at very fine spatial resolutions, the experimental error inherent in the PIV cross-correlation process becomes the dominant source of inaccuracy [34]. This dynamic often creates a V-shaped or L-shaped error curve depending on the specific mathematical formulation used for the pressure Poisson equation, meaning that indefinitely increasing the grid density can actually amplify random measurement noise and artificially inflate the derived pressure gradients [23]. Furthermore, the physical size of the PIV interrogation window inherently acts as a spatial low-pass filter; overly large windows smooth out the velocity fields, severely underestimating localised phenomena such as vorticity, swirling rates, and small-scale vortex population density [35].

This strict dependency on spatial density creates a profound gap between the raw, high-resolution grids generated by modern optical diagnostics and the heavily undersampled grids required to evaluate legacy intake distortion descriptors [3]. A modern Stereoscopic PIV setup can easily generate a dense polar grid, such as *180x49* points, yielding between 9000 and 18000 simultaneous velocity vectors across the aerodynamic interface plane. In contrast, historical industrial practice relies on physical total-pressure probes arranged in a sparse ring-and-rake configuration, typically an *8x10* array that provides a mere 80 discrete measurement points [3]. To compare modern S-PIV reconstructed pressure fields against these legacy industrial datasets, it is

necessary to artificially degrade high-resolution data. This is achieved by downsampling and interpolating the dense S-PIV grid onto the sparse *8x10* probe array, which is subsequently interpolated onto a slightly denser *24x10* grid to calculate standard stability metrics like the $DC60$ [3].

This undersampling compromises the fidelity of the aerodynamic analysis. Raw, high-resolution PIV grids are essential to accurately resolve highly compact flow features, such as the sharp total-pressure deficits associated with an ingested ground vortex or the clearly defined boundaries of diffusion-driven and shock-induced flow separations. When the reconstructed pressure data is downsampled to match the legacy rake resolution, these small-scale, intense flow features are either entirely missed by the sparse grid points or artificially smeared across the interpolation gaps [3]. Consequently, while undersampling is currently necessary to provide backward compatibility with established industrial metrics, it inherently masks the true severity of flow non-uniformities [14]. This gap underscores the urgent need for the aerospace industry to adopt new, high-density distortion descriptors that can fully exploit the rich spatial capabilities of modern velocimetry to ensure the safe operability of future compact engine intakes [3].

2.4.2 Influence of Boundary Conditions

The accuracy of pressure field reconstruction from velocity data is critically dependent on the definition, quantity, and placement of the boundary conditions. In experimental setups characterising compact aero-engine intakes, these boundary conditions are typically provided by an array of wall static pressure taps located at or near the Aerodynamic Interface Plane.

Previous studies and numerical sensitivity analyses have extensively evaluated the optimal number of these pressure probes required to generate a reliable circumferential pressure profile. While legacy test setups might rely on as few as six equispaced taps, investigations using CFD as a virtual testbed reveal that a six-probe configuration often fails to accurately capture localised static pressure peaks [18]. Research indicates that an eight to ten-probe configuration generally offers a strong compromise between global accuracy and the practical

constraints of installing numerous physical taps in a wind tunnel model. However, for capturing highly unsteady, dynamic flow fields, studies have shown that increasing the spatial resolution up to 18 boundary points is necessary to asymptotically improve the accuracy of reconstructed total pressure distortion descriptors, particularly the highly sensitive $DC60$ coefficient [27]. Furthermore, the specific mathematical interpolation scheme used to bridge the gaps between these discrete physical taps, such as Akima interpolation or cubic splines, plays a role in the accuracy. Literature notes that as long as simple polynomial regression with too few probes is avoided, the reconstruction remains relatively robust to the choice of the interpolation method [33].

A fundamental and well-documented limitation of the DSI method is its inherent susceptibility to cumulative error propagation. Because the standard DSI space-marching algorithm begins at the external boundary of the domain, where the known static pressure profile is imposed as a Dirichlet boundary condition and iteratively integrates radially inward toward the centre of the grid, any uncertainties, truncation errors, or measurement noise present in the velocity field are continuously compounded [18]. Consequently, errors accumulate significantly at each successive step of the algorithm as it moves away from the safety of the known boundary [14]. This radial error propagation frequently results in severe artificial distortions of the reconstructed total-pressure field near the centre of the domain. In the context of crosswind operations, this accumulation causes the DSI method to artificially deform the physical topology of the ingested ground vortex and frequently overestimate the severity of the total pressure deficits within the vortex core [3].

The placement of boundary conditions relative to highly separated flow regions or areas of intense pressure gradients also profoundly impacts the overall fidelity of the reconstruction. Sensitivity studies on boundary probe positioning reveal that missing a pressure measurement in a highly distorted sector, such as the lower quadrant of the intake affected by the ground vortex or regions subjected to shock-induced separation, can drastically degrade the global accuracy of the pressure field [33]. Not all boundary points exert the same

influence on the reconstruction. Points located near aggressive flow phenomena are critical for anchoring the integration.

Furthermore, literature examining the error dynamics of pressure solvers highlights that calculating Neumann boundary conditions directly from noisy PIV data near regions of massive separation or flow impingement introduces severe high-frequency spatial and temporal fluctuations into the domain. In highly separated regions, the velocity data is inherently chaotic and noisy. If the solver is forced to derive its boundary gradient from this corrupted data, massive errors immediately propagate inward [34]. Therefore, strategically placing highly accurate Dirichlet boundary conditions as physical static pressure taps, directly within or immediately adjacent to these sensitive, highly separated regions is considered to be critical. By explicitly anchoring the starting point of the integration with a known pressure value at these volatile locations, it is possible to prevent the chaotic velocity fluctuations of the separated shear layer from corrupting the boundary condition itself, thereby mitigating the severe downstream error propagation that would otherwise contaminate the entire reconstructed flow field [33].

2.5 Research Gaps

While advanced non-intrusive diagnostic techniques like S-PIV have successfully captured the complex, unsteady velocity fields of compact aero-engine intakes under crosswind conditions, current experimental practices and data processing methodologies still exhibit significant limitations [3]. A primary limitation in the existing literature is that industry standards for quantifying aerodynamic compatibility rely heavily on a sparse array of intrusive pressure sensors, which inherently lack the spatial and temporal resolution necessary to accurately capture highly dynamic flow features such as ingested ground vortices or massive flow separations [3].

To overcome these instrumentation limits, it has been necessary to derive pressure fields analytically from high-fidelity PIV velocity measurements. However, while pressure from velocity reconstruction is proven, there is a lack of systematic quantification regarding how spatial undersampling affects $DC60$ and IPR in crosswind intake flows across different separation regimes. High-resolution PIV grids are frequently downsampled to match legacy *8x10* rake configurations in order to compute traditional distortion descriptors. Yet, the extent to which this artificial degradation obscures peak distortion events during diffusion-driven, attached, or shock-induced flow conditions remains inadequately characterised [3].

Furthermore, a major technical hurdle in implementing these reconstruction methods, particularly the DSI scheme, is their inherent susceptibility to cumulative error propagation. Because the DSI algorithm integrates spatial pressure gradients from the domain boundaries inward, any uncertainties in the measured velocity field are continuously compounded, often leading to artificial deformations of structures like the ground vortex core [3]. The quality of the reconstructed pressure field is highly sensitive to the implementation of the boundary conditions, which typically rely on wall static pressure taps. Although the literature acknowledge that the number and type of boundary conditions impact the reconstruction, there is a distinct gap in the literature regarding the optimal strategic placement of boundary conditions while aiming to

mitigate DSI error propagation [33]. Strategically positioning physical pressure probes directly within or immediately adjacent to highly turbulent, separated sectors is thought to anchor the mathematical integration, preventing chaotic shear layer fluctuations from corrupting the entire reconstructed flow field.

3 METHODOLOGY

3.1 Scarf and Droop Aero Pitot Intake Model Experimental Setup

To generate the high-fidelity velocity and pressure data required for this study, both experimental and numerical campaigns were conducted using a scaled intake model. The test article was a 1/6.5 scaled non-axisymmetric short intake model representative of a modern UHBPR turbofan configuration. The geometry was designed by Rolls-Royce, and the physical model was manufactured by Deharde GmbH.

Geometrically, the model features a 3D drooped and scarfed configuration specifically designed to replicate the complex aerodynamic profiles of compact nacelles. It possesses a compact overall length-to-inner-diameter ratio of 0.332 and incorporates a non-rotating conical centre-body with a spinner-to-outer circumference ratio of 0.3. The modular physical model consists of several components, including the intake lip, the main duct body, the conical centre-body, support struts, and removable measurement rakes (see Figure 3-1 and Figure 3-2).

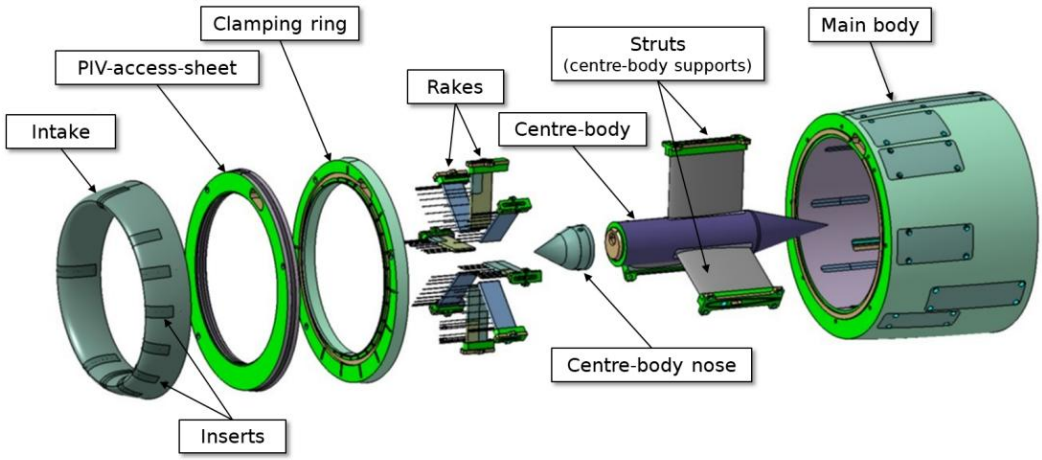


Figure 3-1 Exploded CAD view of the LST intake model. ***(Image copyright of NIFTI Consortium.)***

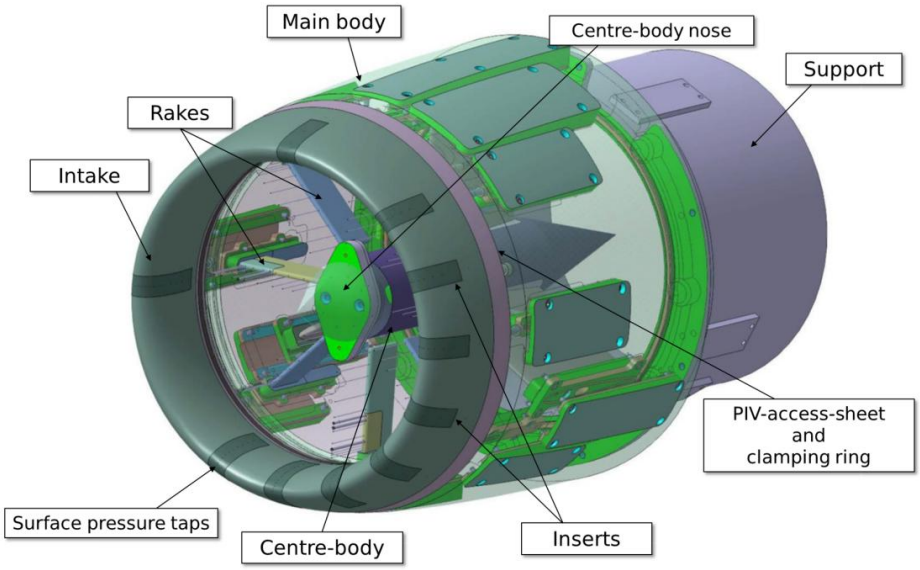


Figure 3-2 CAD image of the assembled LST intake model. ***(Image copyright of NIFTI Consortium.)***

Testing scaled models in wind tunnel environments inherently involves lower Reynolds numbers than those experienced by full-scale engines. To prevent premature laminar boundary layer separation on the outer surface of the intake, custom zigzag boundary-layer trips featuring a 45° wedge angle were installed (see Figure 3-3). This aerodynamic conditioning ensures that the flow reattachment behaviour over the intake lip properly scales to represent real-world VHBPR engine dynamics.

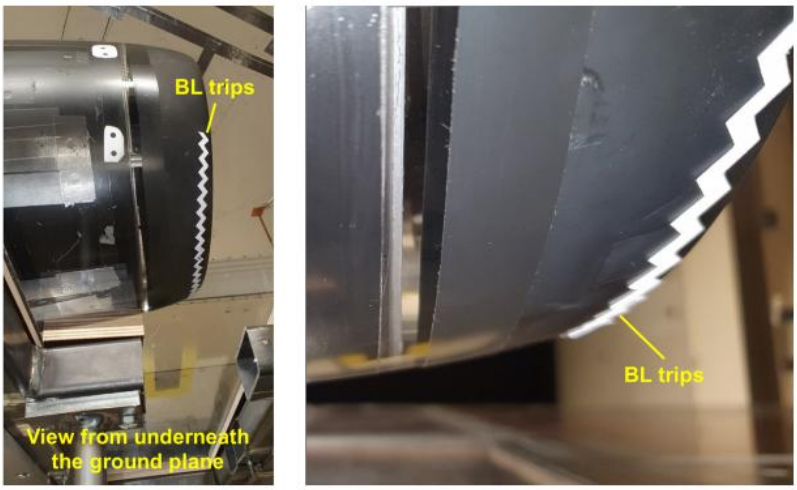


Figure 3-3 Boundary-layer trips with a 45◦ wedge angle placed on the outer intake surface. ***(Images copyright of NIFTI Consortium.)***

The experimental testing campaign was conducted in the Low-Speed wind Tunnel of the German-Dutch Wind Tunnels (DNW-LST) in Marknesse, Netherlands. This facility is an atmospheric, closed-return wind tunnel featuring a 3.022 m wide, 2.25 m high, and 5.75 m long exchangeable test section that delivers high flow quality with streamwise turbulence levels of approximately 0.02%.

The primary operating condition investigated using this model places it in a 90° crosswind at a velocity of 15 knots. To accurately simulate the severe flow distortions encountered during static ground operations or low-speed taxiing—such as ground vortex ingestion and diffusion-driven separation—the model was positioned in proximity to a ground plane. A flat ground plane board spanning the full wind tunnel width was installed below the model at a fixed vertical clearance of 77 mm from the cowl highlight (see Figure 3-4 and Figure 3-5).

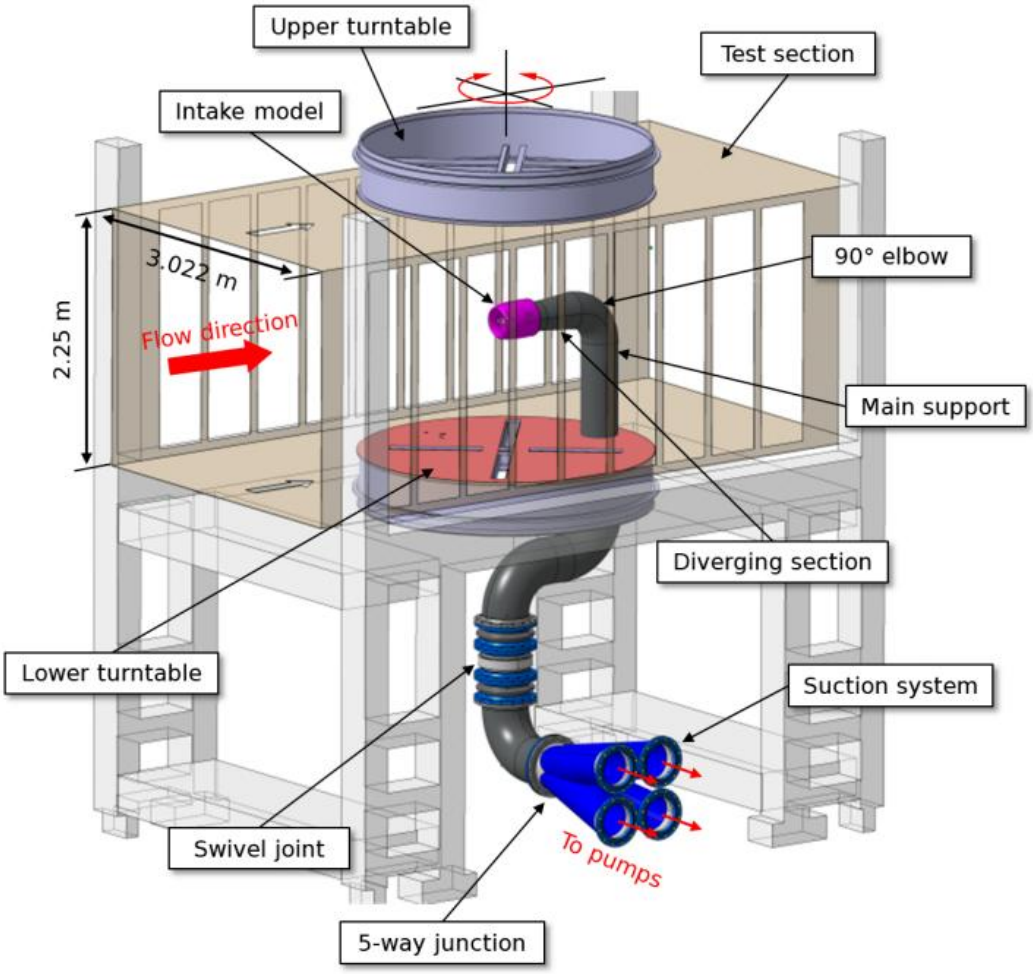


Figure 3-4 Schematic of the DNW-LST wind tunnel test section with the intake model installed. (Image copyright of NIFTI Consortium.)

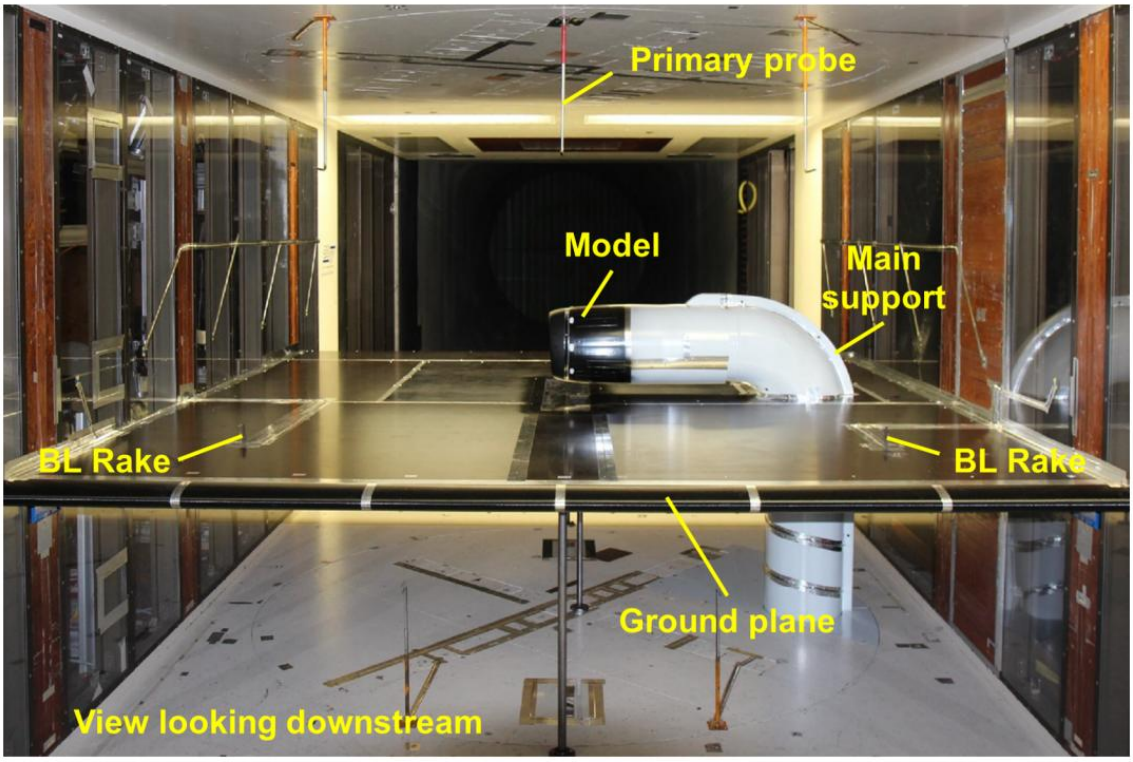


Figure 3-5 Wind tunnel set-up for crosswind testing with a ground plane: (a) side view of the wind tunnel test section with the model installed above the ground plane. (Images copyright of NIFTI Consortium.)

The physical model was structurally supported by a rotating 90-degree-bend suction pipeline featuring internal flow-splitting vanes and a diverging diffuser to prevent internal separation. Airflow was driven through this support pipeline by four external roots blower pumps located outside the facility, with the mass flow rate monitored in real-time by calibrated differential pressure flow stations.

Because the core objective of the methodology involved non-intrusive optical diagnostics, the intake model was specifically adapted to facilitate S-PIV measurements. A transparent ring was integrated into the duct's main body to allow the necessary optical access for laser light sheets to illuminate the Aerodynamic Interface Plane. Furthermore, to minimise laser reflections that could corrupt the PIV image acquisition and cause invalid velocity vectors, all internal and external surfaces of the model, including the intake lip, duct walls, spinner, and physical probes, were coated with a non-reflective matte black paint.

The multi-camera S-PIV system consisted of six LaVision Imager SCMOS cameras equipped with Canon 105 mm lenses and remote-controlled Scheimpflug mounts. These cameras were positioned on a rigid external framework outside the test section's glass window to eliminate flow interference, successfully achieving 98% visual coverage of the measurement plane. The camera setup is illustrated in Figure 3-6. Illumination was supplied by two Quantel Evergreen Nd:YAG lasers mounted on a traverse below the wind tunnel floor, projecting two 4 mm thick laser sheets up through transparent windows in both the ground board and the clear PIV-access ring in the cowl.

The airflow was globally seeded with a di-ethyl-hexyl sebacate (DEHS) aerosol, generating microscopic tracer droplets. For each test point, 1,000 double-frame double-pulse images were recorded at 15 Hz over a 66.7-second window.

While the focus of the optical diagnostics was non-intrusive reconstruction, the model was also heavily instrumented to capture physical pressure data. For total pressure validation, the model exit plane could be fitted with an intrusive rake assembly of 80 total-pressure probes distributed across eight equispaced radial spokes of 10 probes each. Crucially, these physical rakes and the centre-body support struts were fully removed during active S-PIV measurement runs to prevent aerodynamic wake disturbances and visual blockage.

Additionally, the model incorporated 24 static pressure taps to provide the wall boundary conditions required to mathematically integrate pressure fields from the S-PIV velocity data. These comprised 16 cowl wall taps equispaced at 22.5-degree intervals and 8 taps evenly distributed on the spinner centre-body, as mapped out in Figure 3-7.

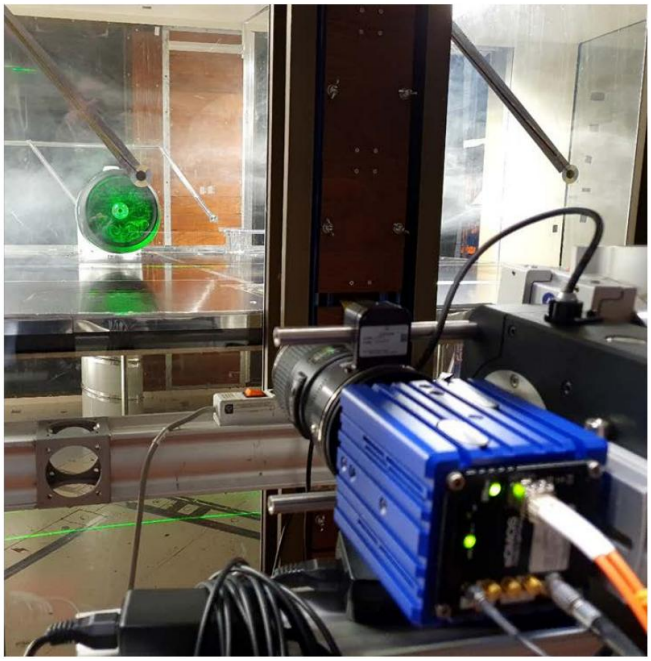


Figure 3-6 Camera PIV setup.

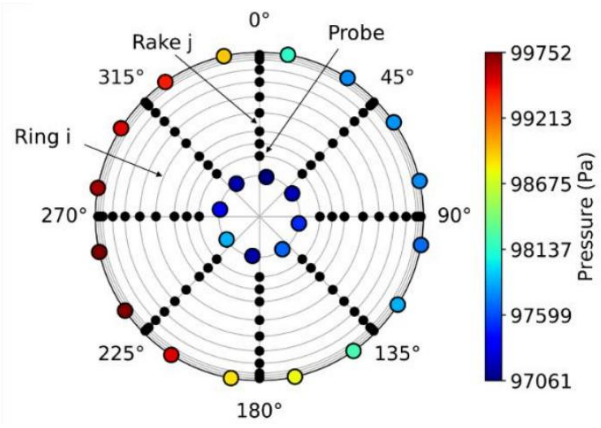


Figure 3-7 Total pressure probes on the instrumented rake at the intake exit section (black markers) and circumferential static pressure taps used as boundary conditions for the pressure from velocity reconstruction [14].

3.2 Direct Spatial Integration

The Direct Spatial Integration method reconstructs the instantaneous static pressure field by directly integrating the spatial pressure gradients derived from the Navier-Stokes momentum equations. Unlike techniques that formulate a global boundary value problem, such as the Poisson Pressure Equation, the DSI method relies strictly on the spatial and temporal derivatives of the measured velocity field to deduce these gradients.

The extraction of pressure relies on isolating the pressure gradient within the governing fluid dynamics equations. For the high Reynolds number flows typical of aero-engine intakes, inertial forces strongly dominate viscous forces. Under these conditions, the viscous diffusion term is negligibly small and can be omitted, simplifying the Navier-Stokes momentum equation to a balance between the pressure gradient and the material acceleration [14]:

$$\nabla p = -\rho\left(\frac{\partial u}{\partial t} + u \cdot \nabla u\right) \quad \textbf{(3-1)}$$

Because the Aerodynamic Interface Plane (AIP) features a circular geometry, the Cartesian velocity components (u, v, w) obtained from the PIV measurements or CFD simulations are converted into a cylindrical frame of reference (v_r, v_θ, w). The domain is subsequently discretised into a highly dense polar grid to match the rich spatial resolution of the S-PIV measurements.

Using the cylindrical formulation, the partial derivatives of velocity in the radial $\left(\frac{\partial}{\partial r}\right)$ and circumferential $\left(\frac{\partial}{\partial \theta}\right)$ directions are computed at each grid node using second-order central finite difference approximations.

Depending on the specific dataset being analysed and the capabilities of the measurement system, out-of-plane spatial gradients $\left(\frac{\partial u}{\partial z}\right)$ and temporal derivatives $\left(\frac{\partial u}{\partial t}\right)$ can either be included or omitted [14]. For instance, if only time-averaged steady-state numerical data or planar, non-tomographic PIV measurements are available, these terms are neglected, whereas time-resolved measurements allow the inclusion of the temporal acceleration component.

To perform the DSI across the discretised plane, a starting reference is required. A Dirichlet boundary condition is applied at the external boundary of the domain, consisting of a prescribed circumferential static-pressure distribution. In an experimental setting, this boundary distribution is generated by linearly interpolating the readings from the array of physical static-pressure taps positioned around the intake's inner wall.

With the boundary condition established, the DSI algorithm utilises an inward space-marching technique, adapted from the method originally proposed by Baur and Köngeter for a polar grid. The calculation iteratively proceeds radially inward from the outer duct wall toward the intake centre-body. The static pressure at an unknown internal node is calculated as the average of the integrated pressures from four previously determined neighbouring points [3]:

$$p_{i,j} = \frac{1}{4}\left[\left(p_{i+1,j-1} + \Delta p_{i+1,j-1}\right) + \left(p_{i+1,j} + \Delta p_{i+1,j}\right) + \left(p_{i+1,j+1} + \Delta p_{i+1,j+1}\right) + \left(p_{i,j-1} + \Delta p_{i,j-1}\right)\right] \quad \textbf{(3-2)}$$

The local pressure increments Δp along the integration paths are evaluated using a first-order Taylor polynomial. This polynomial multiplies the previously computed spatial pressure gradients by the grid spacing in the radial and circumferential directions ($\Delta r, \Delta\theta$). Averaging the integration paths from multiple adjacent nodes helps to smooth out local uncertainties and measurement noise embedded in the velocity data [3].

Compressibility Correction

The standard DSI scheme assumes a constant fluid density, a simplification valid only for low-speed flows (Ma < 0.3). However, the compact intake operating at high MFCR generates severe flow acceleration around the windward lip, pushing local velocities into the supersonic regime and terminating in shock waves.

To maintain reconstruction accuracy in these compressible regions, the DSI algorithm incorporates a thermodynamic density correction. By assuming adiabatic flow with constant total enthalpy, the local static temperature is

expressed as a function of a known reference total temperature and the measured velocity magnitude. The ideal gas law is then substituted into the momentum equations, allowing the fluid density to be evaluated dynamically at each grid node as a function of the local static pressure and velocity [31].

Once the corrected static pressure field is obtained via integration, the total pressure field p_0 is finally calculated at each node across the AIP using the standard compressible isentropic relation:

$$p_0 = p\left(1 + \frac{\gamma - 1}{2} M^2\right)^{\frac{\gamma}{\gamma - 1}} \quad \textbf{(3-3)}$$

3.3 MIDAS

Following the reconstruction of the total-pressure field at the AIP, the subsequent analysis of flow non-uniformities and the calculation of distortion metrics were performed using MIDAS (Modular Intake Distortion Analysis Software). MIDAS is a unified, Python-based framework developed at Cranfield University specifically designed to automate and standardise the analysis of intake flow distortion from heterogeneous datasets, including both CFD and S-PIV measurements [36]. In the context of this thesis, MIDAS serves as the core post-processing engine to evaluate the aerodynamic compatibility and structural forcing implications of the reconstructed pressure fields. The methodology for utilising MIDAS involves several key sequential steps:

Since modern S-PIV provides thousands of randomly distributed or highly dense data points, these must be mapped onto standardised grids to calculate established industrial metrics. MIDAS discretises the circular AIP into a defined number of radial rings and circumferential rakes. For this research, the software was used to mathematically simulate varying physical rake geometries by interpolating the dense reconstructed pressure fields onto these discrete probe locations. For unstructured or scattered data points, MIDAS interpolates the flow variables onto the selected ring-rake configuration using a Delaunay triangulation method [3].

Once the flow variables are mapped onto the specified ring-rake grid, MIDAS computes area-weighted averages across the AIP. The software features built-in automated routines to evaluate conventional total-pressure descriptors. Specifically, MIDAS was employed to calculate the Distortion Coefficient $DC60$. The software algorithms evaluate sector-averaged values around the annulus to locate the worst 60-degree sector, enabling the direct comparison of peak distortion levels between the full-resolution ground truth data and the artificially undersampled reconstructed fields.

Beyond steady-state aerodynamic metrics, MIDAS includes advanced frequency-domain and Engine Order analysis capabilities to assess the potential for turbomachinery forced-response excitation. Based on SAE ARP6912

methodology, MIDAS performs a discrete Fourier transform on the circumferential pressure distributions at each radial ring to extract the sine and cosine Fourier coefficients a_n and b_n. These coefficients are then used to calculate the forcing magnitude and the normalised HEI for each specific engine order.

3.4 Distortion Coefficient *DC60*

To quantify the severity of flow non-uniformity at the AIP, this thesis utilises the Distortion Coefficient, commonly referred to as $DC60$. Originally developed by Rolls-Royce, $DC60$ is a widely adopted industry standard used to measure the intensity of circumferential total-pressure distortion, specifically targeting the most severely distorted region of the flow that is likely to trigger rotating stall or engine surge.

The coefficient is mathematically defined as the difference between the area-averaged total pressure across the entire AIP and the lowest average total pressure found within any 60-degree circumferential sector, normalised by the area-averaged dynamic pressure at the AIP. [14]

$$DC_{60} = \frac{\overline{p_{0,AIP}} - \overline{p_{0,60°}}}{\overline{q_{AIP}}} \quad \textbf{(3-4)}$$

Where:

- $\overline{p_{0,AIP}}$ is the area-averaged total pressure at the AIP.
- $\overline{p_{0,60°}}$ is the area-averaged total pressure in the most distorted sector of 60° extent.
- $\overline{q_{AIP}}$ is the area-averaged dynamic pressure at the AIP.

Within this methodology, the calculation of the $DC60$ is automated using MIDAS. Because the $DC60$ is a sector-based descriptor, the algorithm computes area-weighted averages within a defined 60-degree circumferential window.

To locate the worst-case sector, this 60-degree window is rotated circumferentially around the annulus. Depending on the grid resolution being analysed, this rotation is performed at discrete angular increments, for example, steps of 5° to define up 72 overlapping sectors. The lowest area-averaged pressure extracted from all possible sector positions is then isolated and applied to the equation.

The core analytical function of the $DC60$ in this thesis is to serve as the comparative metric for evaluating the influence of spatial resolution on distortion assessment. Modern Stereoscopic PIV and CFD generate highly dense polar grids, yielding thousands of discrete data points. Conversely, historical industry practice relies on sparse physical rake arrays, typically an 8-rake by 5-ring configuration, yielding merely 40 discrete points. To evaluate the impact of spatial resolution and assess whether pressure-from-velocity reconstruction can bridge the information gap, a phased analytical framework is implemented using high-resolution CFD "ground truth" data as a baseline.

First, the isolated effect of low spatial resolution on the distortion descriptor is quantified by directly down sampling the full-resolution CFD ground truth baseline, modelled on a dense polar grid of 180 rakes and 49 rings, onto progressively sparser grid configurations. By computing the $DC60$ using purely the mathematically degraded CFD data, the error introduced strictly by a lack of physical probe density is isolated and assessed.

Second, the full-resolution velocity fields are passed through the pressure-from-velocity reconstruction algorithm to generate a high-resolution reconstructed pressure field. This reconstructed field is subsequently subjected to two separate $\Delta DC60$ analyses designed to evaluate different performance dimensions:

1. **Resolution-by-Resolution Comparison:** For every artificially downsampled grid configuration, the $DC60$ is calculated from both the degraded CFD ground truth and a matching, identically downsampled reconstructed array. The absolute discrepancy is computed as:

$$\Delta DC60_{resolution} = DC60_{reconstruction} - DC60_{CFD} \quad \textbf{(3-5)}$$

This isolates the concurrent mathematical vulnerabilities of the system, mapping out how discretisation truncation errors and intrinsic reconstruction errors scale together across individual spatial resolutions. Here three errors are influencing the result: the undersampling of ground

truth, the reconstruction error and the undersampling of the reconstructed Flowfield.

2. **Real Case Scenario Simulation:** To replicate an actual industrial test environment where a high-fidelity velocimetry reconstruction might replace standard physical diagnostic infrastructure, the $DC60$ computed from the full-resolution reconstructed pressure field *180x49* is compared directly against the $DC60$ calculated from individual, sparse physical rake arrays of variable density:

$$\Delta DC60_{real\ case} = DC60_{reconstructed,max} - DC60_{CFD,variable} \quad \textbf{(3-6)}$$

By plotting and comparing these unique discrepancies across different mass flow capture ratios, this thesis explicitly maps out how sparse physical instrumentation masks critical aerodynamic phenomena, such as highly localised ground vortices and establishes the operational boundaries and reliability of the aerodynamic interface plane velocimetry reconstruction technique.

3.5 Aeromechanics

3.5.1 Flow-Induced Vibrations and Harmonic Excitation Index

Beyond steady-state aerodynamic performance losses, non-uniform airflow entering the engine poses a severe structural threat. As the fan blades rotate through spatially distorted flow fields, they experience time-varying aerodynamic loads. This non-uniformity can synchronously force the blades at specific frequencies. If these frequencies align with the blades' natural structural frequencies, it can induce severe vibrations, high-cycle fatigue, and potentially catastrophic aerofoil failure [37].

To mathematically characterise the aeromechanical severity of the total-pressure distortion fields reconstructed in this thesis, the methodology follows the guidelines outlined in the SAE AIR8458 document to assess blade forced response. This involves decomposing the spatial non-uniformities into discrete harmonic components that directly correspond to specific Engine Orders. The calculation procedure is performed systematically for each radial ring across the AIP.

First, the circumferential total pressure distribution is extracted for a given ring. The resolution of this extraction is critical. To avoid spatial aliasing, the methodology strictly adheres to the Nyquist theorem, which dictates that the maximum Engine Order that can be accurately resolved is exactly half the number of circumferential rakes. For example, when evaluating a sparse notional 8-rake array, the maximum discernible harmonic is 4 EO, whereas the denser reconstructed grids allow for the evaluation of much higher frequency harmonics.

The airflow harmonics are then analytically described by extracting the order Fourier coefficients from the circumferential total-pressure data. A Discrete Fourier transform is applied to separate the pressure signal into its real and imaginary components, respectively cosine and sine, yielding the Fourier coefficients a_n and b_n. Using the extracted Fourier coefficients, the absolute forcing vector magnitude V_n for a specific engine order at a given radial ring is calculated as:

$$V_n = \sqrt{a_n^2 + b_n^2} \tag{3-7}$$

This magnitude represents the zero-to-peak amplitude of the aerodynamic forcing for that specific harmonic. To make the forcing magnitude comparable across different intake operating conditions and mass flow rates, it must be non-dimensionalised. This yields the Harmonic Excitation Index HEI_n. While the standard SAE AIR8458 methodology normalises this value using a face-averaged dynamic head defined by the difference between average total and static pressures ($Q_{avg} = P_{T,avg} - P_{S,avg}$), this thesis methodology utilises a modified approach leveraging the available velocity data. The forcing magnitude is instead normalised by the dynamic head calculated directly from the fluid density and velocity:

$$q = \frac{1}{2}\rho V^2 \tag{3-8}$$

$$HEI_n = \frac{V_n}{q} \tag{3-9}$$

By calculating the HEI_n for various spatial resolutions this methodology explicitly quantifies how spatial undersampling impacts the prediction of structurally critical forced-response vibrations, then an analysis following the one done on the $DC60$ metric is executed.

3.5.2 MIDAS Validation

SAE provides a standard Excel spreadsheet specifically designed to compute the HEI according to their established aeromechanical guidelines. However, given the vast amount of high-resolution data and the varying spatial resolutions evaluated in this thesis, performing these calculations via the standard Excel tool was impractical. Instead, the automated Python-based software MIDAS was employed to process the datasets.

To rigorously verify the reliability of the software's aeromechanical algorithms, a direct validation study was conducted by benchmarking the HEI outputs generated by MIDAS against the official SAE Excel spreadsheet.

Both computational tools evaluated pressure data extracted from a sparse, industry-standard *8x5* probe configuration. The comparison was systematically applied across the three core operating conditions analysed in this research to ensure algorithm stability under varying distortion intensities: diffusion-driven separation, attached flow, and shock-driven separation. To ensure absolute robustness, the harmonic indices were calculated and compared for both the baseline CFD ground truth pressure fields and the mathematically reconstructed pressure fields from RANS velocity field. For each flow condition and dataset, the order harmonic excitation indices extracted by MIDAS were plotted in bar charts directly alongside the benchmark results generated by the SAE Excel sheet. This visual and numerical comparison explicitly confirms that the HEI values computed by MIDAS perfectly match the results from the SAE spreadsheet across all evaluated engine orders and radial rings, as visible in Figure 3-8 and Figure 3-9.

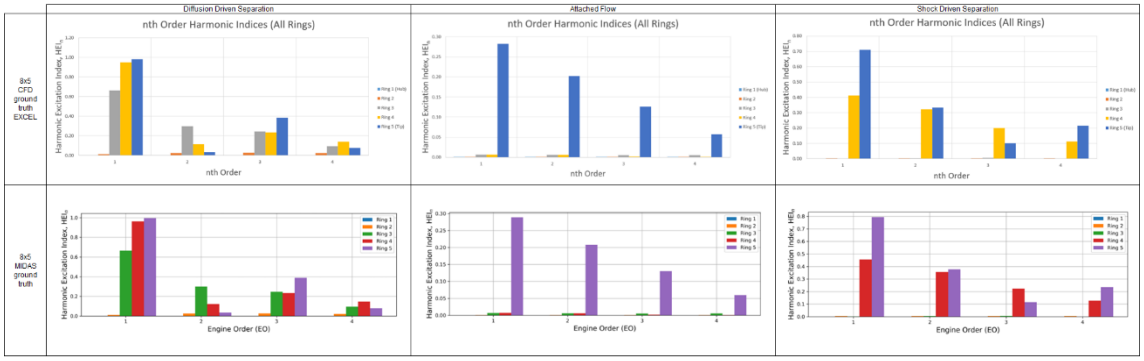


Figure 3-8 CFD ground truth SAE spreadsheet vs. MIDAS for three flow conditions.

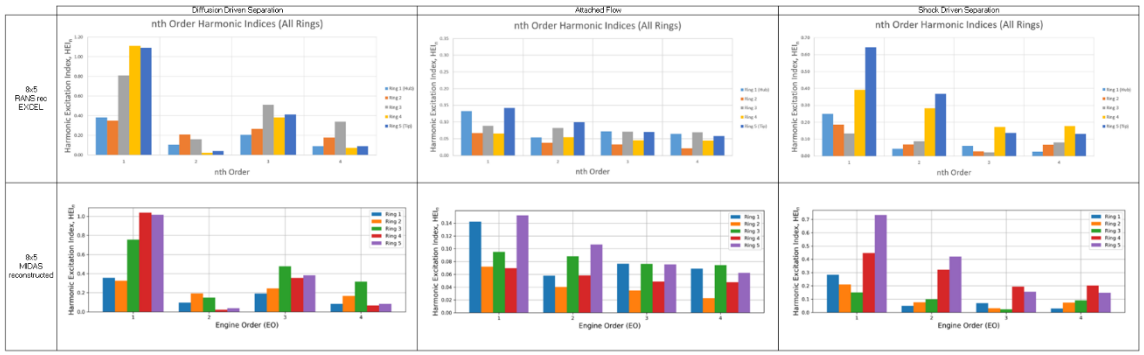


Figure 3-9 Reconstructed Pressure Field SAE spreadsheet vs. MIDAS for three flow conditions.

This comprehensive alignment proves that the MIDAS harmonic analysis routines function flawlessly and accurately mirror established industry standards, fully justifying its use as the primary computational engine for the subsequent spatial undersampling investigations in this thesis.

3.6 Analysis of the Datasets

To evaluate the accuracy of the pressure-from-velocity reconstruction method the methodology dictates a comparative analysis applied to two parallel datasets. A computed dataset acting as the test field, and an experimental Stereoscopic Particle Image Velocimetry (S-PIV) dataset. To ensure the reconstruction and distortion analysis methods are robust across all potential engine operating regimes, the datasets are evaluated across three distinct aerodynamic flow conditions. These conditions, visible in Table 3-1 Working conditions for both the datasets., represent varying levels of Mass Flow Capture Ratio and mass flow rates, all evaluated under a severe 90° crosswind at 15 knots. The analysis is performed on the following specific states for both datasets:

Table 3-1 Working conditions for both the datasets.

CASE	Characteristic	MFCR
RANS 1	Diffusion Driven Separation	5.93
PIV 1		7.83
RANS 2	Attached Flow	12.39
PIV 2		14.71
RANS 3	Shock Driven Separation	17.3
PIV 3		17.81

The first case is characterised by a massive, separated region and an ingested ground vortex. In the attached flow case, the flow is predominantly uniform with a small area of low momentum. Finally, the third case is characterised by severe flow acceleration around the intake lip resulting in supersonic patches and shock induced flow separation.

The core methodological step for evaluating spatial resolution involves artificially degrading the high-fidelity data. First, the full-resolution total-pressure field is established on a highly dense polar grid of 180 circumferential rakes by 49 radial rings.

Next, the analysis systematically undersamples this baseline into progressively sparser arrays to simulate various physical rake configurations. The data is downsampled onto specifically structured grids. The evaluated rake configurations include 8, 12, 24, 36, 72, and 180 rakes, combined with varying radial ring counts including 5, 10, 20, 30, 40, and 49 rings, a sample is shown in Figure 3-10, full set in Figure B-1. For each artificially degraded grid, the distortion metrics are recalculated at a circumferential resolution matching the undersampling (e.g., evaluating a 12-rake array uses a 30° sector resolution, while a 72-rake array uses a 5° resolution).

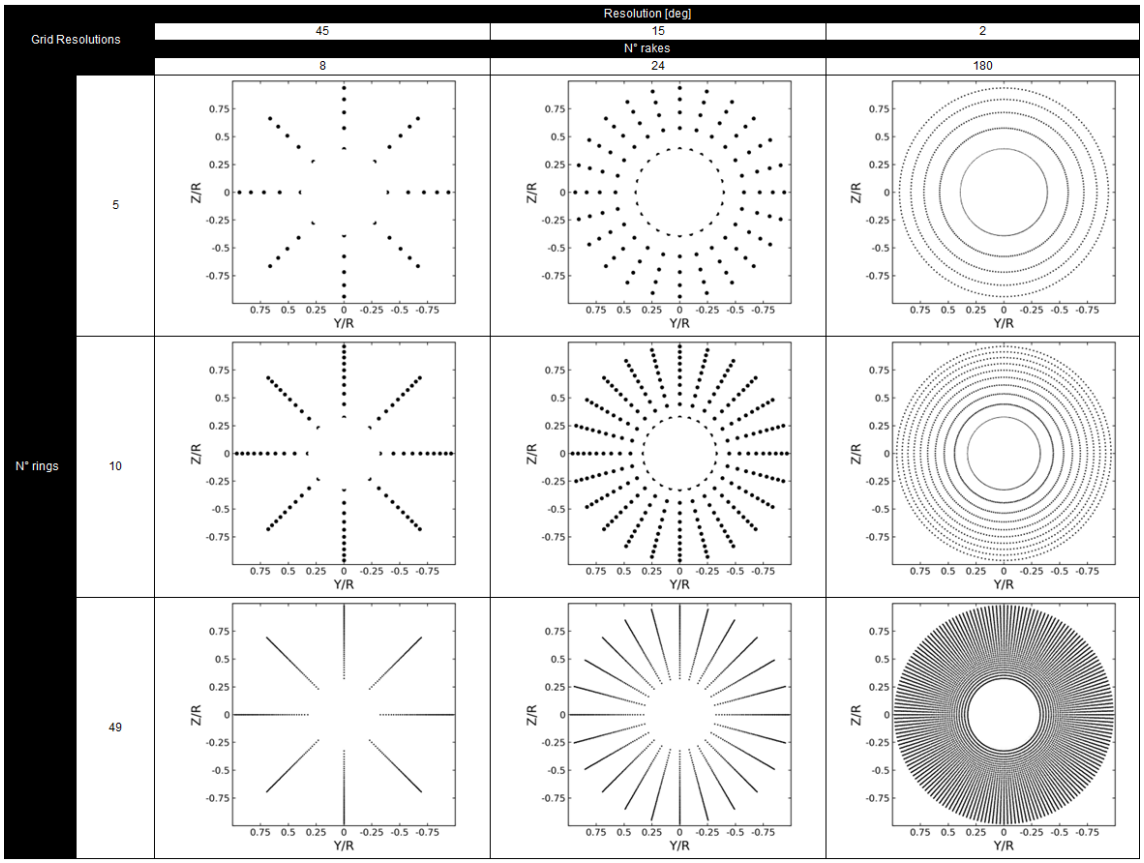


Figure 3-10 Some of the grid resolutions used to downsample the full resolution.

To quantify the shortcomings of traditional physical rakes versus the non-intrusive reconstruction method, the methodology relies on computing the absolute difference between the metrics derived from different resolutions and datasets. The total discrepancy observed in the distortion descriptors is isolated into three distinct sources of error:

The ground truth undersampling error

Evaluated by comparing the full-resolution CFD against its own undersampled grids to observe purely spatial truncation effects.

The intrinsic reconstruction error

Evaluated by comparing the full-resolution reconstructed field against the full-resolution CFD ground truth, resolution by resolution. Here the undersampling of ground truth error, the undersampling of the reconstructed flow, as well as the reconstruction error are stacking one upon the other.

Ultimately, the methodology simulates a real-world scenario by directly comparing a notional physical rake (e.g., an *8x5* array extracted from the ground truth) against the fully reconstructed flowfield. This last case will obviously lack of the blockage effect and measurement errors that would be always interfering with real world testing. By tracking how the metrics evolve as the number of simulated rakes increases from 8 up to 180 across the three distinct flow regimes, this analytical framework demonstrates whether an industry-standard physical rake fails to capture critical distortion features, such as the ground vortex, compared to a full-resolution S-PIV optical reconstruction.

4 COMPUTED DATASET ANALYSIS

4.1 Flow Conditions

The analysis of the computed dataset evaluates the intake model across three distinct aerodynamic flow conditions. These conditions represent varying levels of engine demand and are defined by their specific MFCR and corresponding mass flow rates. The three core operating states analysed are:

- Diffusion-Driven Separation, which occurs at a low mass flow rate, characterised by an MFCR of 5.93.
- Attached Flow, representing an intermediate, optimal state, this condition operates at an MFCR of 12.39.
- Shock-Driven Separation, reached at a high mass flow rate, featuring an MFCR of 17.3.

The baseline CFD ground truth pressure fields for each of these three respective operating conditions are visually detailed in Figure 4-1.

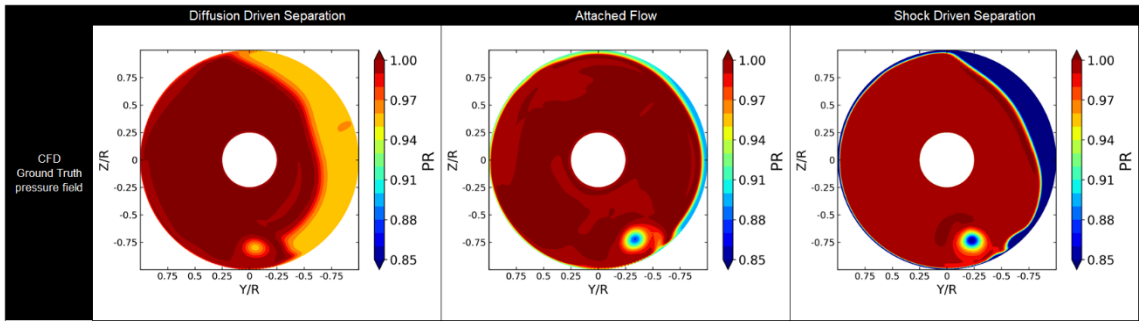


Figure 4-1 The three different flow conditions which will be analysed, CFD ground truth.

4.2 Undersampling of Ground Truth

4.2.1 Diffusion Driven Separation

By reconstructing the distortion indicators across varying virtual rake configurations, as shown in Figure 4-2 (full set in Figure B-2), distinct asymptotic trends and resolution thresholds were identified.

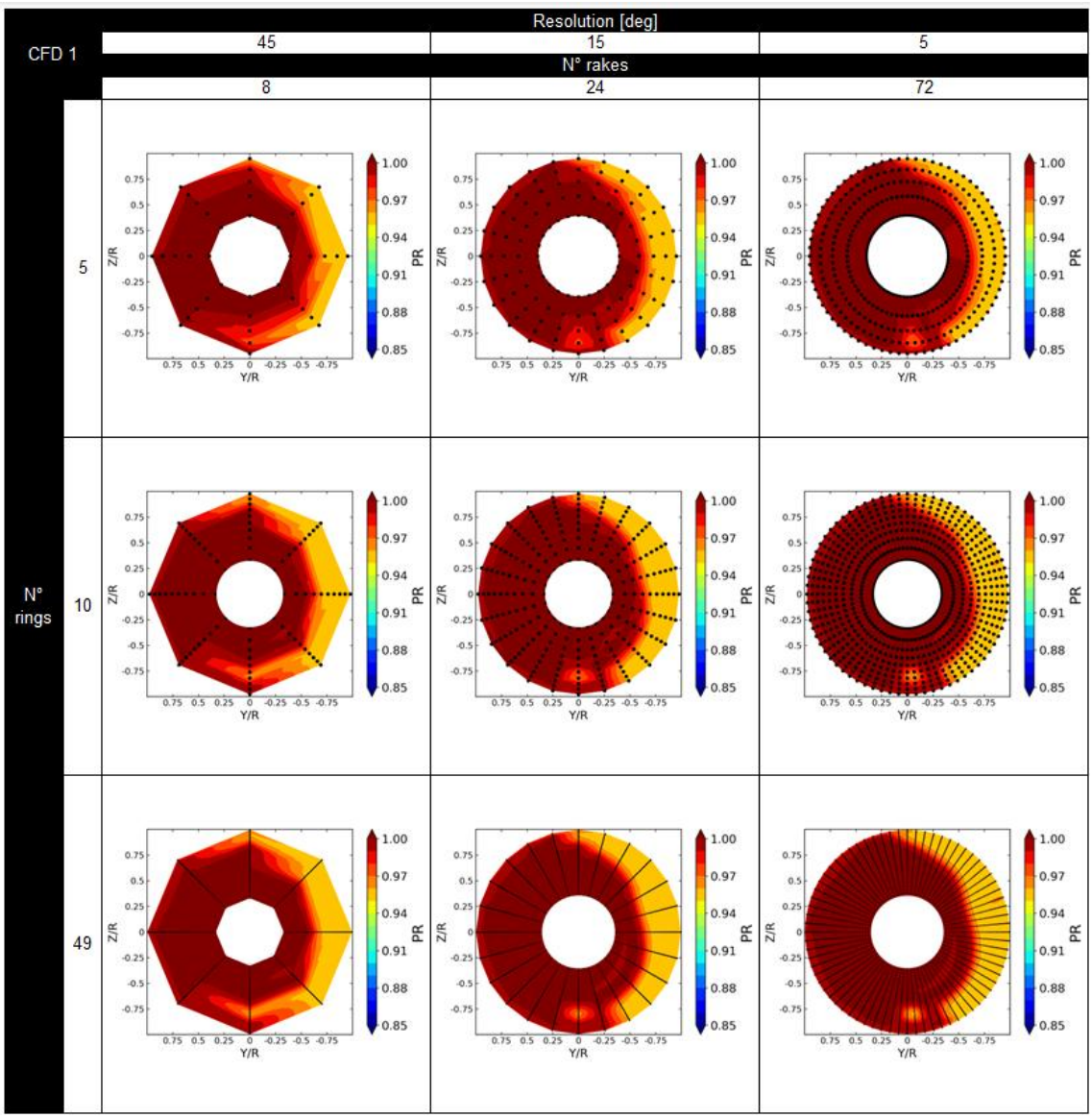


Figure 4-2 CFD ground truth pressure field at different resolutions of rakes and rings.

Table 4-1 ground truth DC60.

CFD 1 Ground Truth DC60		Resolution [deg]					
		45	30	15	10	5	2
		N° rakes					
		8	12	24	36	72	180
N° rings	5	0.500	0.529	0.565	0.568	0.569	0.570
	10	0.503	0.537	0.573	0.576	0.578	0.579
	20	0.499	0.532	0.568	0.572	0.573	0.574
	30	0.497	0.530	0.566	0.570	0.571	0.572
	40	0.497	0.530	0.566	0.570	0.572	0.573
	49	0.497	0.530	0.566	0.570	0.571	0.572

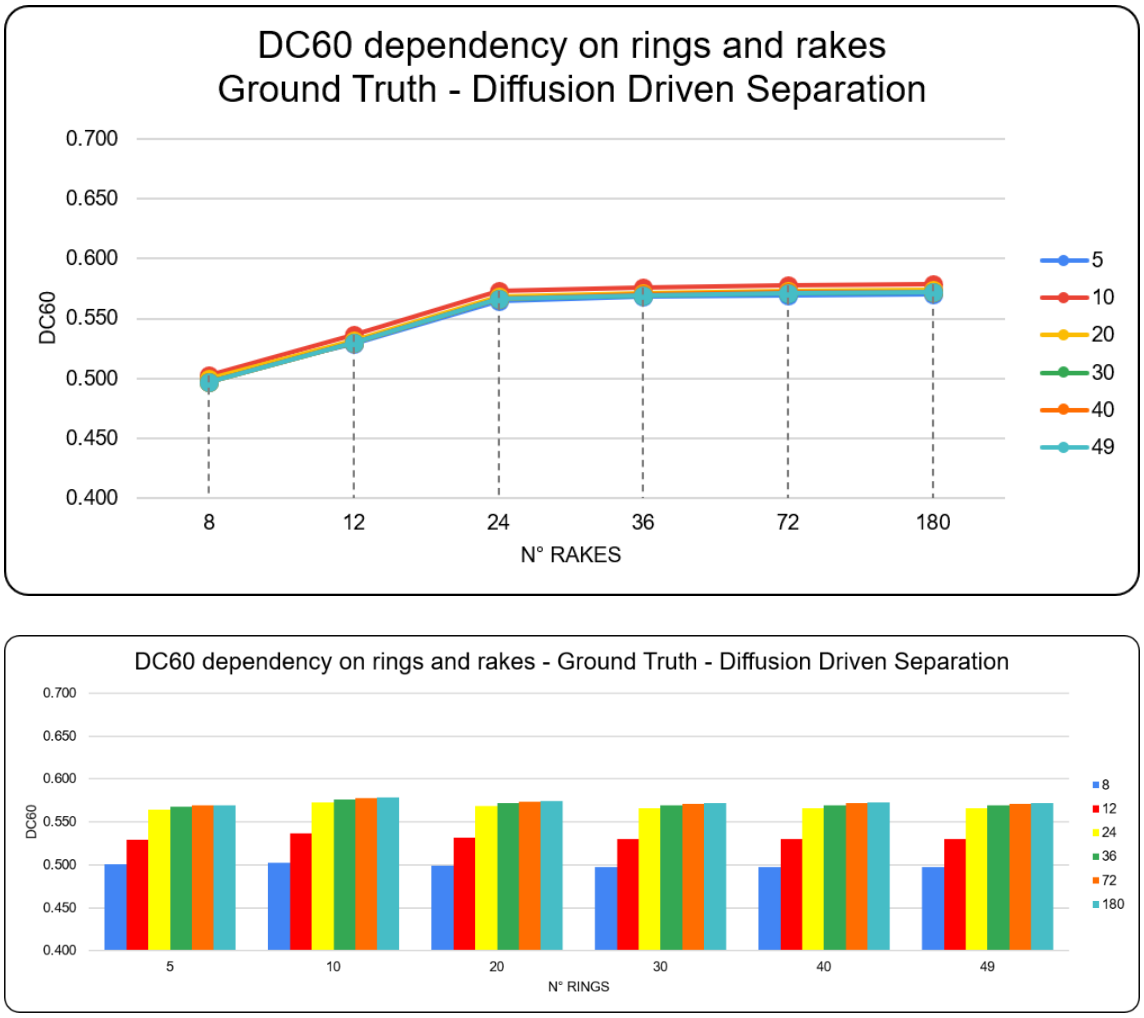


Figure 4-3 Numerical and visual representation of DC60 behaviour at different undersampled resolutions.

When evaluating the calculated distortion metrics as a function of the number of rakes, the data exhibits a characteristic convergence behaviour in Figure 4-3. At lower angular resolutions, the reconstructed fields underestimate

the distortion levels. As the number of rakes increases, the calculated values experience a sharp initial rise before gradually approaching an asymptotic plateau. This behaviour is primarily governed by the spatial scale of the aerodynamic characteristic of this flow regime. At lower rake counts, the virtual instrumentation mesh is too coarse to capture localised flow features. Specifically, the ground vortex falls entirely between the angular positions of the rakes, leading to a severe smoothing effect in the reconstructed total pressure field. The localised ground vortex is only effectively intercepted and resolved when the angular resolution is increased to 24 rakes or more. Beyond this critical threshold, further increases in the number of rakes yield diminishing returns, as the captured peak distortion values stabilise toward the true baseline CFD value.

In contrast to the highly sensitive angular resolution dependency, variations in the number of concentric rings demonstrate a notably lower impact on the overall accuracy of the distortion measurement. While a minimum radial density is required to map the boundary layer profile along the intake casing, increasing the ring count beyond the baseline configuration provides minimal correction to the calculated metrics. Consequently, for the diffusion-driven separation case, the distortion metric convergence is constrained by the circumferential spacing required to resolve the ground vortex, rather than the radial partitioning of the flow field.

4.2.2 Attached Flow

The analysis of the attached flow condition reveals an asymptotic convergence behaviour analogous to that observed in the diffusion-driven separation regime. However, the geometric undersampling, as shown in Figure 4-4 (full set in Figure B-3), in this optimal operating state introduces unique artificial scaling effects depending on whether the resolution is reduced angularly or radially.

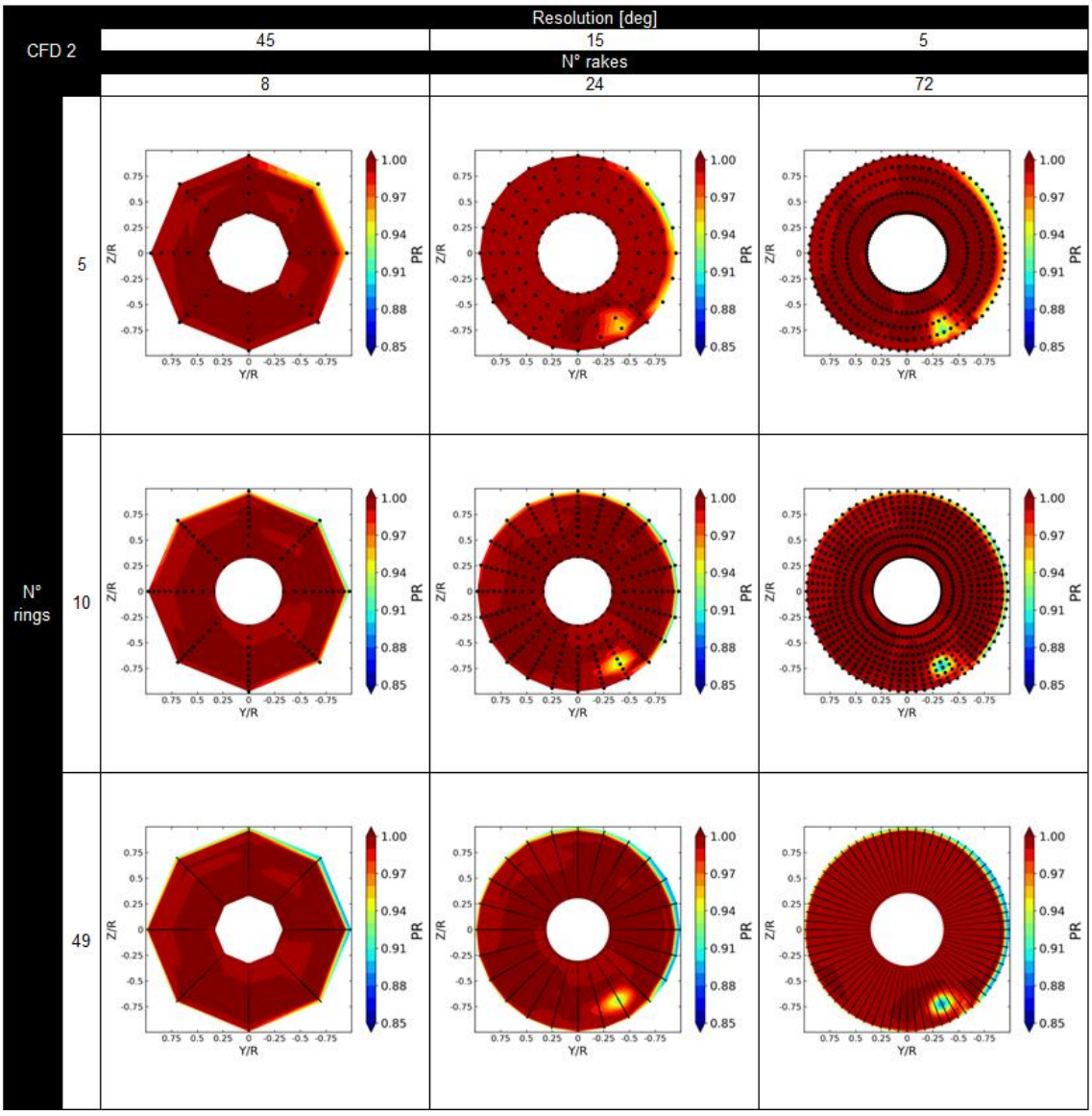


Figure 4-4 CFD ground truth pressure field at different resolutions of rakes and rings.

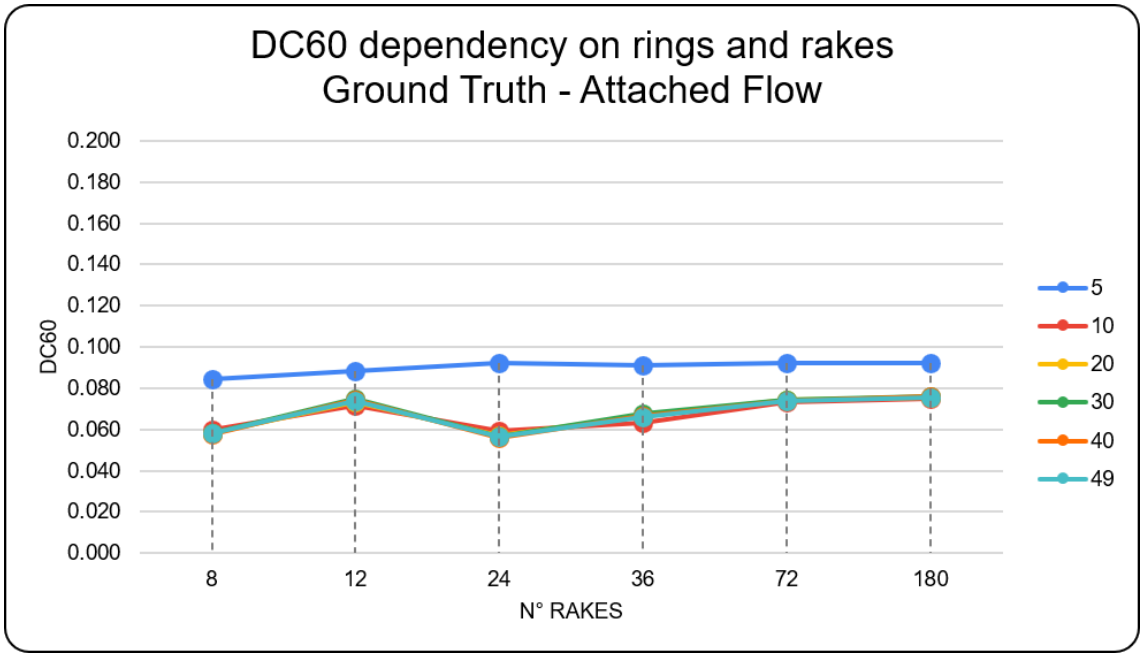
The capability of the virtual instrumentation to accurately detect and size the ground vortex remains highly dependent on the circumferential spacing of the rakes. At an extremely coarse resolution of 8 rakes, the instrumentation spacing is too wide to effectively intersect the localised ground vortex, causing the reconstructed field to miss this critical aerodynamic feature entirely. When the angular resolution is increased to 12 rakes, the virtual probes successfully intercept the vortex. However, the interpolation across the still relatively large angular gaps causes the vortex to be represented as spatially larger than its

physical bounds. This artificial broadening of the low-pressure region overestimates the magnitude of the distortion, leading to an artificially higher computed $DC60$ compared to the baseline ground truth.

Unlike the diffusion-driven separation case, radial undersampling plays a significantly more disruptive role in the attached flow condition. This sensitivity is driven by a distinct low-momentum area present on the windward side of the intake, induced by the presence of the wall.

Table 4-2 ground truth DC60.

CFD 2 Ground Truth DC60		Resolution [deg]					
		45	30	15	10	5	2
		N° rakes					
		8	12	24	36	72	180
N° rings	5	0.085	0.088	0.092	0.091	0.092	0.092
	10	0.060	0.072	0.060	0.063	0.073	0.075
	20	0.058	0.074	0.057	0.067	0.074	0.076
	30	0.058	0.075	0.056	0.068	0.074	0.076
	40	0.058	0.074	0.056	0.067	0.074	0.076
	49	0.058	0.074	0.056	0.066	0.074	0.076



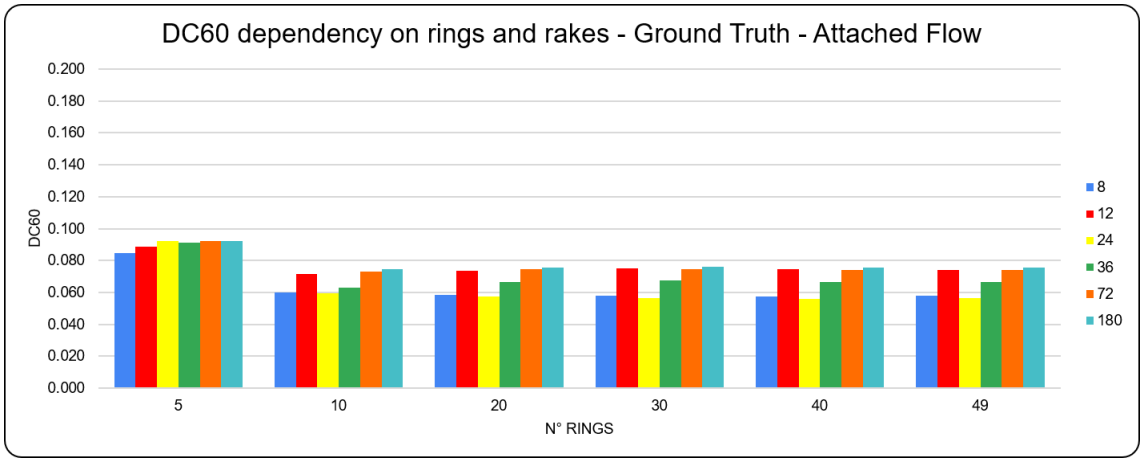


Figure 4-5 Numerical and visual representation of DC60 behaviour at different undersampled resolutions.

Using a coarse radial array of only 5 rings is insufficient to accurately capture the steep pressure gradients associated with this low-momentum zone near the wall. This lack of radial definition artificially enlarges the calculated low-momentum area and depresses the average total pressure recovery across the face. Consequently, the spatial smearing of the low-momentum region directly contributes to a further, artificial increase in the calculated $DC60$ metric.

4.2.3 Shock Driven Separation

The final condition analysed is the shock-driven separation regime. Geometric undersampling in this extreme suction state exhibits the familiar asymptotic convergence (Figure 4-6, full set in Figure B-4), yet it introduces specific quantitative deviations in the $DC60$ due to the severe flow separation characteristic of this operating point.

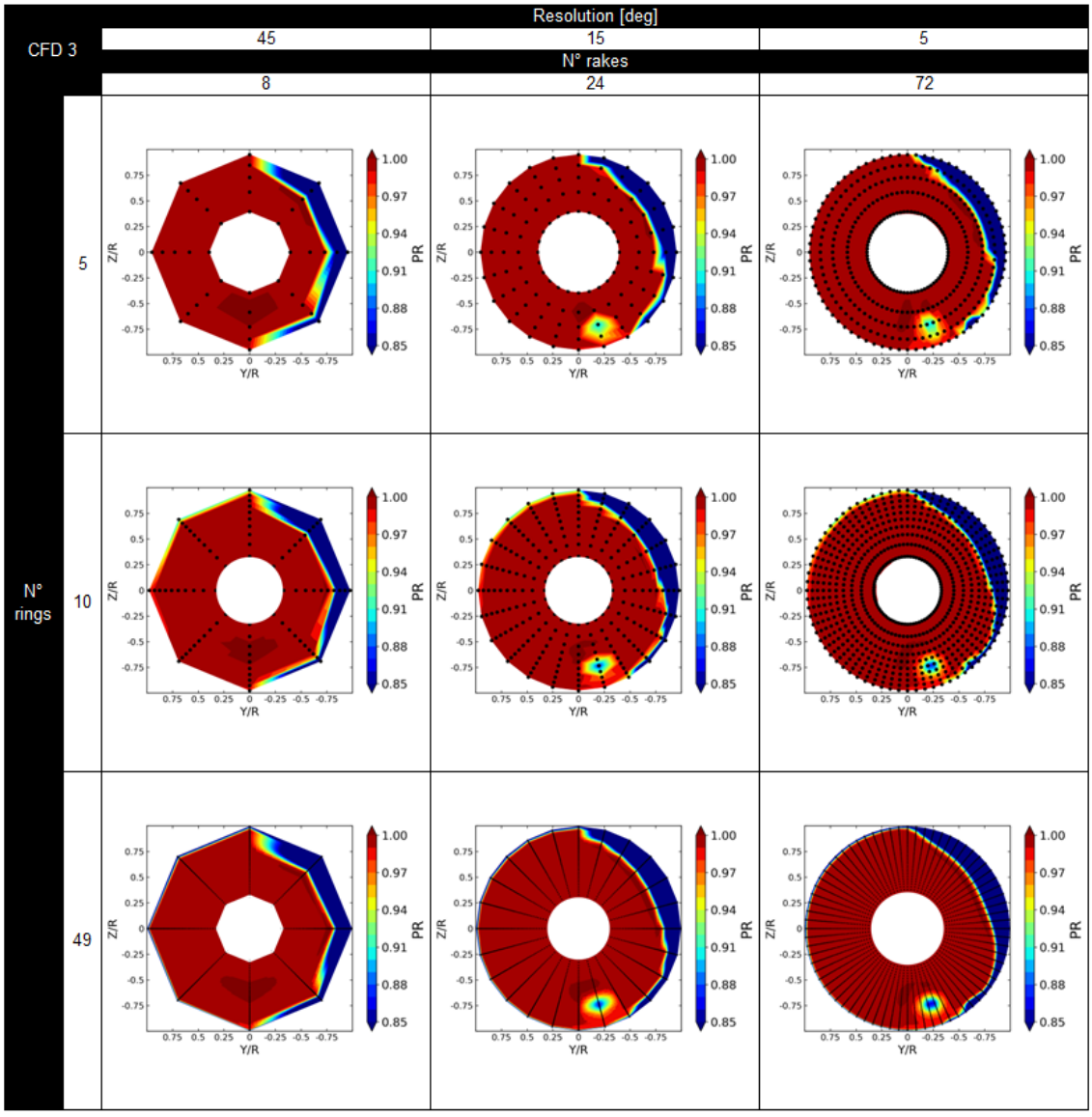


Figure 4-6 CFD ground truth pressure field at different resolutions of rakes and rings.

Table 4-3 ground truth DC60.

CFD 3 Ground Truth DC60		Resolution [deg]					
		45	30	15	10	5	2
		N° rakes					
		8	12	24	36	72	180
N° rings	5	0.319	0.365	0.370	0.374	0.377	0.378
	10	0.303	0.350	0.353	0.356	0.358	0.359
	20	0.297	0.343	0.346	0.350	0.352	0.352
	30	0.296	0.343	0.346	0.349	0.351	0.352
	40	0.295	0.342	0.345	0.348	0.350	0.351
	49	0.295	0.341	0.345	0.348	0.350	0.350

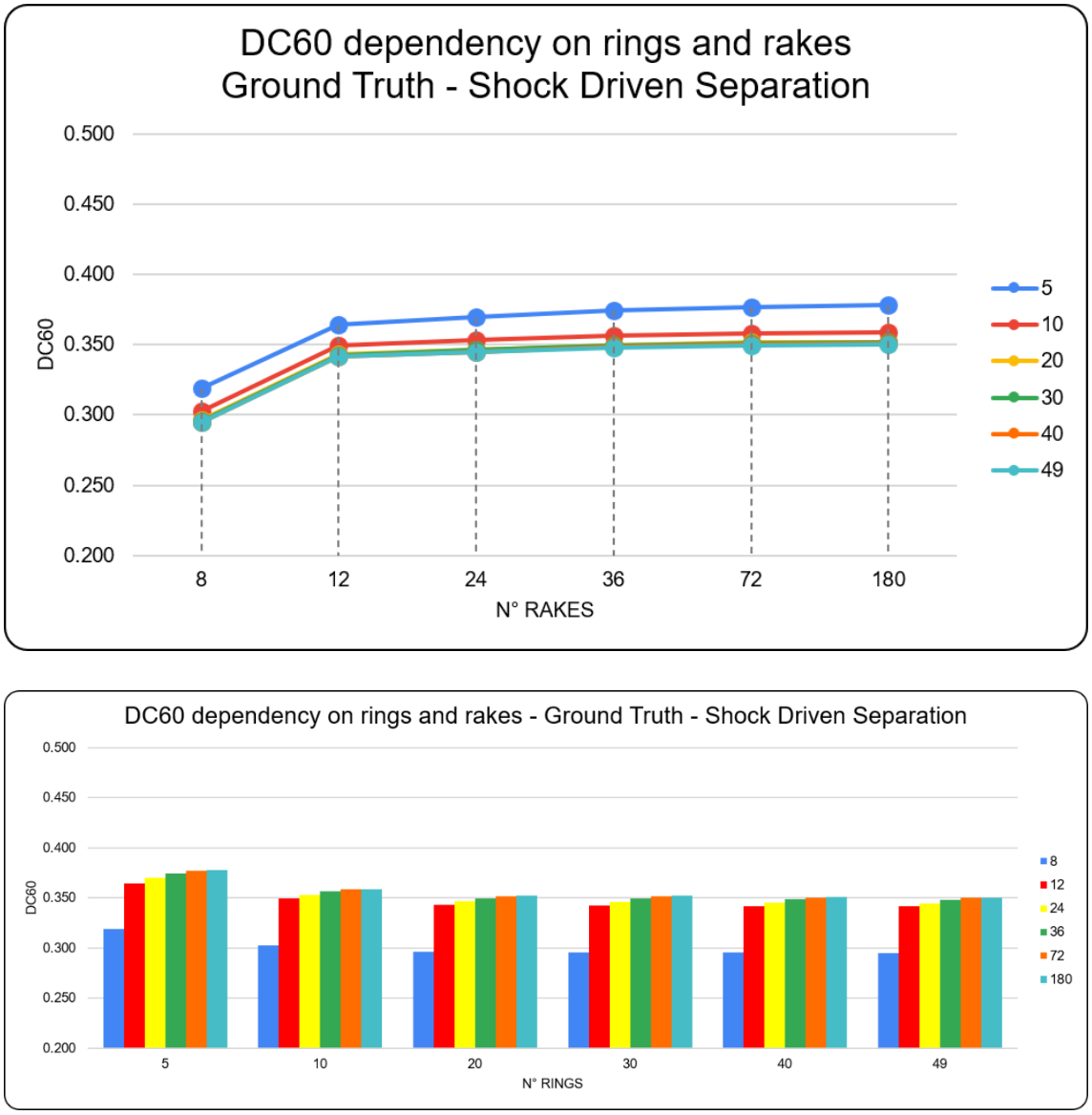


Figure 4-7 Numerical and visual representation of DC60 behaviour at different undersampled resolutions.

Consistent with both the diffusion-driven and attached flow conditions, the angular resolution dictates the virtual instrumentation's ability to detect localised aerodynamic features. At sparse rake configurations, the angular spacing is too broad, causing the virtual instrumentation array to completely miss the ground vortex. As the number of rakes increases, the reconstructed pressure field successfully intercepts the vortex. The computed distortion metrics correspondingly rise and approach a stable asymptote, aligning with the baseline CFD ground truth once a sufficient circumferential density is achieved.

The shock-driven separation case demonstrates a distinct sensitivity to radial undersampling, primarily concerning the extent and severity of the separated flow region. Reducing the radial resolution to a minimum array of 5 rings proves insufficient to accurately resolve the sharp pressure gradients that define the boundary of the separation bubble. Consequently, the spatial interpolation across these sparse radial points causes the reconstructed total pressure field to display an artificially thicker and more expansive separated area. This geometric smearing and bigger separation zone skew the distortion calculations. The reliance on only 5 rings introduces a quantifiable measurement penalty, artificially inflating the resulting $DC60$ metric by approximately 0.02 relative to the fully resolved, high-density configurations.

4.3 Influence of Spatial Resolution on CFD Ground Truth

To systematically evaluate the reliability of discrete probing methods, this section quantifies how varying spatial resolutions impact the accuracy of the extracted distortion metrics when compared directly to the full-resolution CFD baseline. By examining the absolute differences generated by various virtual probe arrays, it becomes possible to identify whether standard physical rake configurations introduce inherent measurement flaws or structural blind spots. The discrepancy between the fully resolved flow field and the undersampled discrete arrays is visualised using a scatter plot methodology. In this graphical representation, each individual data point corresponds to a specific instrumentation layout, mapping its calculated absolute delta against the true CFD baseline.

4.3.1 Diffusion Driven Separation

The scatter plot in Figure 4-8 highlights a distinct measurement penalty associated with coarse angular sampling. Specifically, it demonstrates that when an insufficient number of rakes is employed, the calculated $DC60$ metric is highly inaccurate and deviates significantly from the ground truth. This phenomenon is directly related to the spatial aliasing of critical aerodynamic structures. In configurations with sparse rake counts, the highly localised ground vortex falls between the physical instrumentation blind spots. Consequently, the interpolation algorithm fails to resolve the vortex as an independent structure, and it artificially merges with the main diffusion-driven separation area. This unphysical blending of low-pressure zones fundamentally alters the reconstructed pressure topography, thereby skewing the resulting distortion coefficients.

Furthermore, the scatter plot data clarifies the relative importance of radial versus angular resolution in this specific flow regime. For this type of analysis, variations in the number of rings demonstrate remarkably low relevance when compared to the dominant influence exerted by the number of rakes. The overall accuracy of the CFD ground truth reconstruction in a diffusion-driven state is therefore almost entirely governed by the circumferential density of the physical rake array, while radial undersampling introduces only minimal additional error.

Table 4-4 Absolute Delta DC60 (Full Resolution - Undersampled).

CFD 1 Ground Truth Δ DC60 (real-undersampled)		Resolution [deg]					
		45	30	15	10	5	2
		N° rakes					
		8	12	24	36	72	180
N° rings	5	0.072	0.043	0.008	0.004	0.003	0.002
	10	0.070	0.035	-0.001	-0.004	-0.006	-0.006
	20	0.073	0.040	0.004	0.001	-0.001	-0.002
	30	0.075	0.042	0.006	0.003	0.001	0.000
	40	0.075	0.042	0.006	0.002	0.001	0.000
	49	0.075	0.042	0.006	0.003	0.001	-

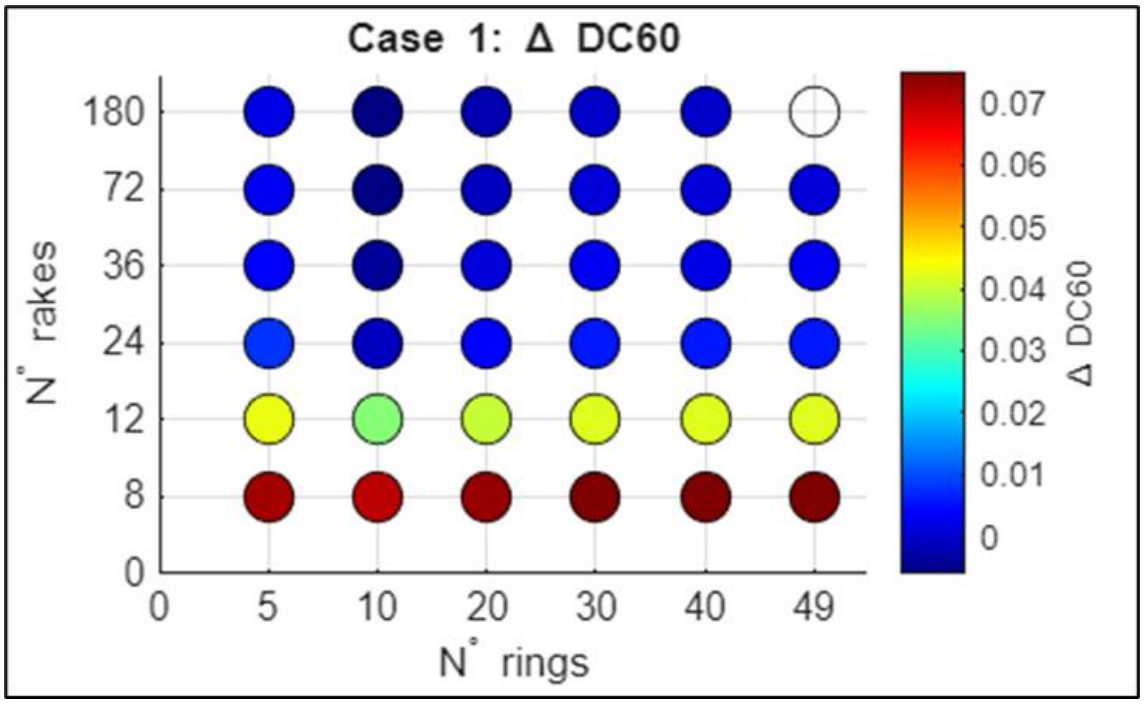


Figure 4-8 Absolute Delta DC60 (Full resolution - Undersampled).

4.3.2 Attached Flow

A critical observation from this data in Figure 4-9 is the counterintuitive performance of the 24-rake configuration, which registers as the least accurate angular resolution among the array sizes tested. This significant deviation is a direct consequence of spatial aliasing interacting with the localised geometry of the flow field. In this specific angular layout, the compact ground vortex is intercepted by only a single rake, rather than being spanned by two. Consequently, the interpolation algorithm artificially constrains the spatial footprint of the vortex, making the low-pressure region appear significantly smaller than its physical reality. This geometrical underrepresentation directly

translates to an unphysical decrease in the calculated $DC60$ metric, resulting in a pronounced absolute error compared to the baseline.

Furthermore, the scatter plot corroborates the previously discussed limitations regarding radial undersampling in this operational state. The sparse 5-ring configuration proves distinctly unreliable for this specific flow condition, as it fails to adequately capture the near-wall low-momentum boundary gradients. However, once this minimal radial density threshold is surpassed, the distortion extraction becomes highly stable. All other higher-density ring configurations demonstrate mathematically consistent results, indicating that while extreme radial sparsity introduces a severe measurement penalty, the results stabilise rapidly with adequate ring counts.

Table 4-5 Absolute Delta DC60 (Full Resolution - Undersampled).

CFD 2 Ground Truth Δ DC60 (real-undersampled)		Resolution [deg]					
		45	30	15	10	5	2
		N° rakes					
		8	12	24	36	72	180
N° rings	5	-0.009	-0.013	-0.016	-0.015	-0.016	-0.017
	10	0.016	0.004	0.016	0.013	0.003	0.001
	20	0.017	0.002	0.018	0.009	0.001	0.000
	30	0.018	0.001	0.019	0.008	0.001	0.000
	40	0.018	0.001	0.020	0.009	0.002	0.000
	49	0.018	0.002	0.019	0.009	0.002	-

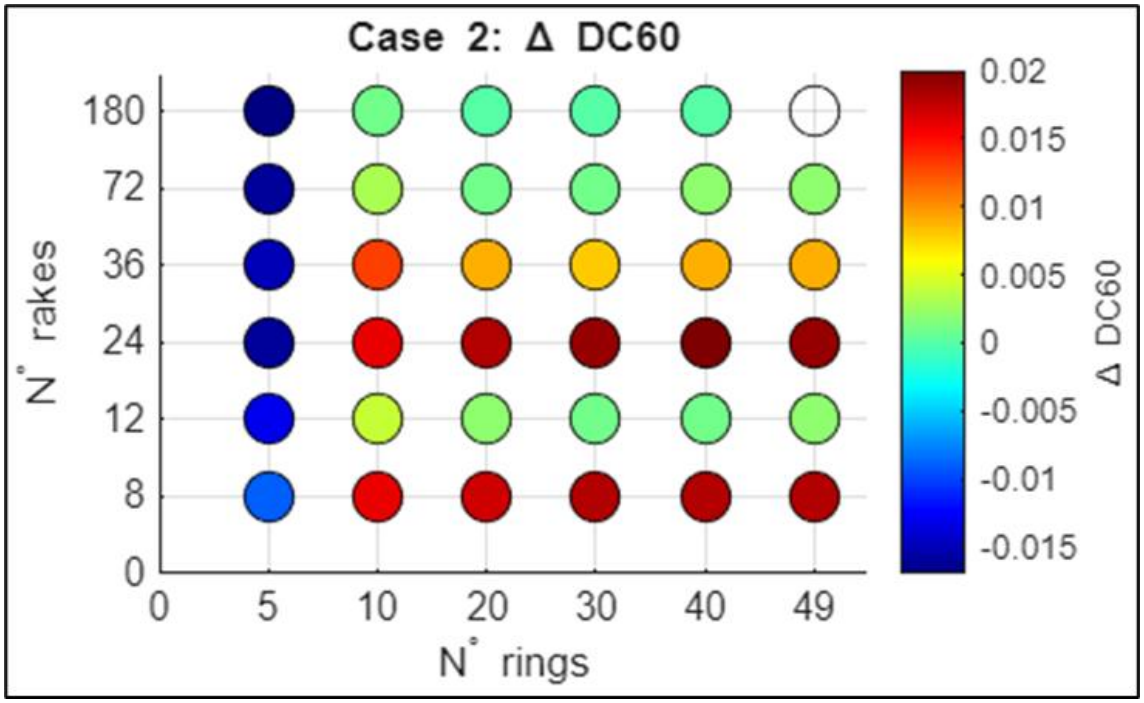


Figure 4-9 Absolute Delta DC60 (Full resolution - Undersampled).

4.3.3 Shock Driven Separation

In this extreme suction regime, the mathematical relationship between spatial resolution and measurement fidelity follows a predictable trend. The visual data demonstrates a direct correlation where an increased number of physical rakes improves accuracy relative to the baseline.

Unlike the severe spatial aliasing and structural blind spots observed in the diffusion-driven state, where some features were entirely missed by sparse arrays, the shock-driven separation exhibits a steady and monotonic convergence. As the physical instrumentation setup approaches the geometric density of the full resolution, the absolute delta of the calculated $DC60$ metric decreases proportionally. This behaviour aligns directly with theoretical expectations for a flow field dominated by a large, expansive separation zone. In this condition, the measurement error is primarily governed by the overall sampling density rather than the abrupt omission of highly compact flow structures. Consequently, the accuracy of the distortion assessment in this specific operating state scales directly and reliably with the concentration of the instrumentation array, with both rake and ring additions contributing to the gradual minimisation of the absolute error.

Table 4-6 Absolute Delta DC60 (Full Resolution - Undersampled).

CFD 3 Ground Truth Δ DC60 (real-undersampled)		Resolution [deg]					
		45	30	15	10	5	2
		N° rakes					
		8	12	24	36	72	180
N° rings	5	0.031	-0.014	-0.019	-0.024	-0.027	-0.028
	10	0.048	0.001	-0.003	-0.006	-0.008	-0.009
	20	0.054	0.007	0.004	0.001	-0.001	-0.002
	30	0.055	0.008	0.004	0.001	-0.001	-0.002
	40	0.055	0.009	0.005	0.002	0.000	0.000
	49	0.056	0.009	0.006	0.002	0.001	-

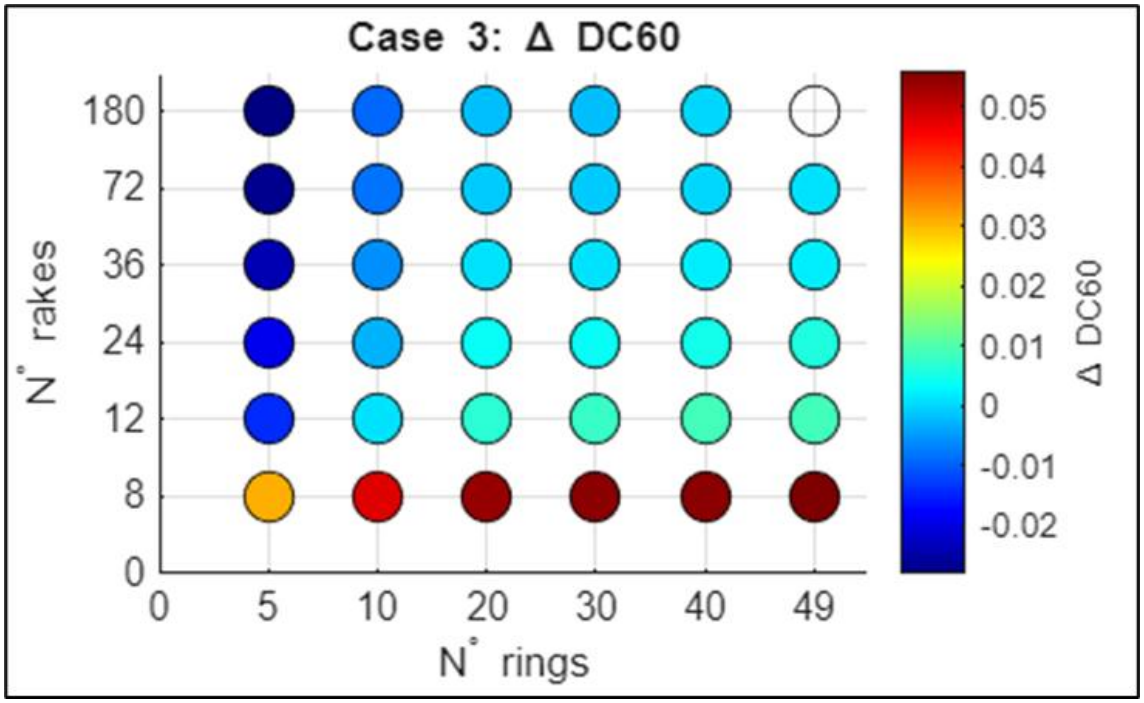


Figure 4-10 Absolute Delta DC60 (Full resolution - Undersampled).

4.4 Pressure Reconstruction from RANS Velocity Field

To further evaluate the distortion assessment methodologies, the total pressure field was derived indirectly from the computed RANS velocity field. This was achieved using the Direct Spatial Integration (DSI) reconstruction method with compressibility effects enabled. The baseline reconstruction was computed on a high-density cylindrical grid comprising 180 rakes and 49 rings (*180x49*). The DSI algorithm initialises using boundary conditions prescribed at the external circumference of the intake face and systematically integrates the pressure gradients radially inward toward the inner circumference (the spinner). This baseline reconstruction was established using the full set of boundary conditions provided by the 180 peripheral probes.

Following the baseline reconstruction, the spatial resolution was systematically undersampled to assess the sensitivity of the DSI method to grid density. The reconstructed flowfield was evaluated across a matrix of reduced grids, featuring angular resolutions of 8, 12, 24, 36, 72, and 180 rakes, each paired with radial resolutions of 5, 10, 20, 30, 40, and 49 rings. For every undersampled configuration, the $DC60$ metric was calculated using a sector resolution equivalent to the angular spacing of the rakes (e.g., a 30° evaluation sector for a 12-rake configuration, and a 5° sector for 72 rakes). The calculated metrics were then plotted and compared against the CFD ground truth to quantify the reconstruction accuracy.

4.4.1 Diffusion Driven Separation

The application of the DSI reconstruction method to the diffusion-driven separation regime reveals significant localised deviations from the original continuous flowfield. A qualitative review of the reconstructed pressure contours in Figure 3-1Figure 4-11 immediately highlights the presence of numerical artifacts inherent to the integration scheme. Because the mathematical integration marches directionally from the outer casing towards the spinner, localised pressure deficits at the outer boundary propagate inward. Consequently, in every reconstructed contour in Figure 4-12 (full set in Figure B-5), it is possible to notice a distinct artificial trail of low pressure recovery

extending inward from the primary diffusion-driven separation area and the ground vortex. These radial trails are purely numerical errors associated with this specific pressure reconstruction technique and do not exist in the baseline CFD ground truth.

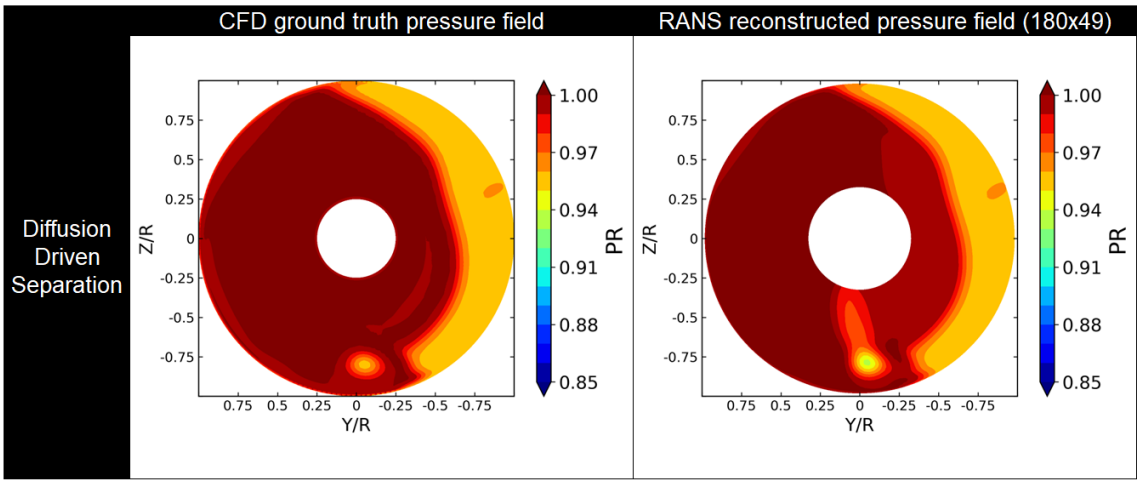


Figure 4-11 Real pressure field vs. Reconstructed pressure field.

Quantitatively, the bar chart in Figure 4-14 Comparison between reconstructed flowfield $\mathrm{DC60}$ and ground truth flowfield $\mathrm{DC60}$. demonstrate that the reconstructed flowfield consistently overestimates the $DC60$ metric relative to the true CFD baseline. Despite this overall overestimation, the dependency on spatial resolution mirrors the trends observed in the ground truth undersampling.

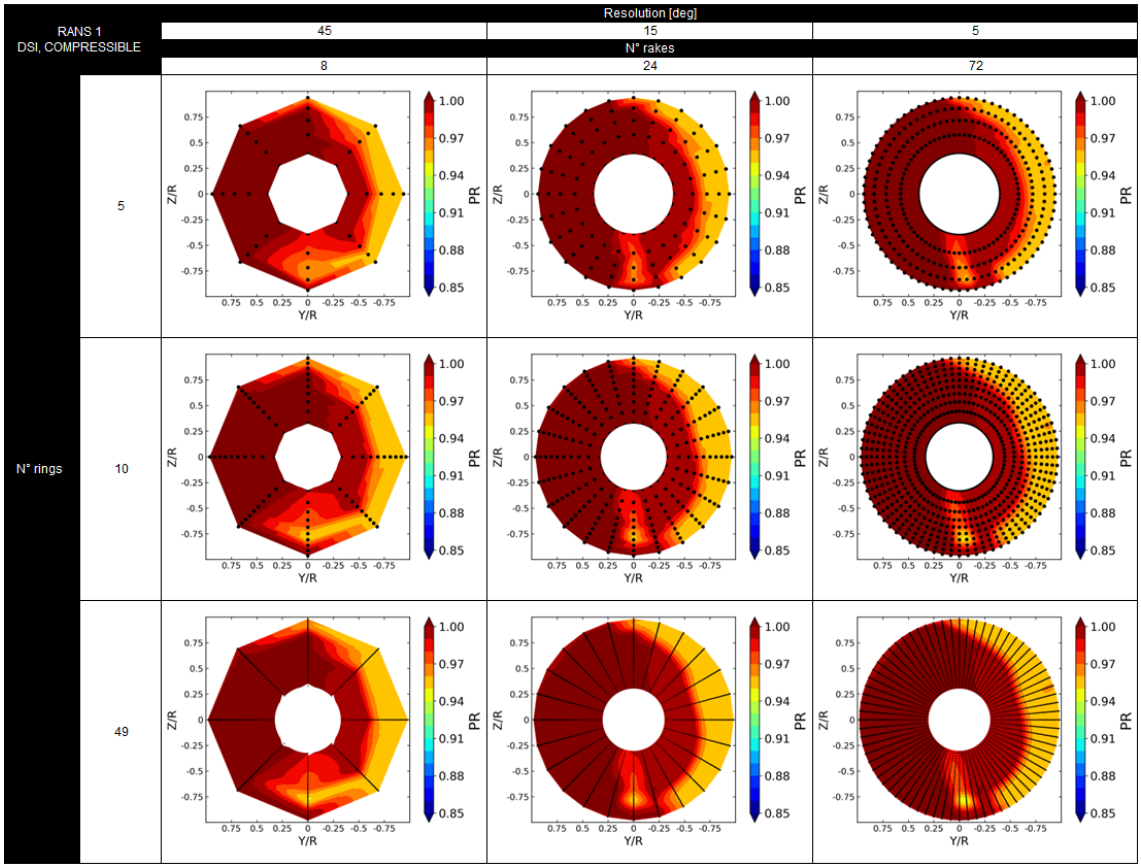
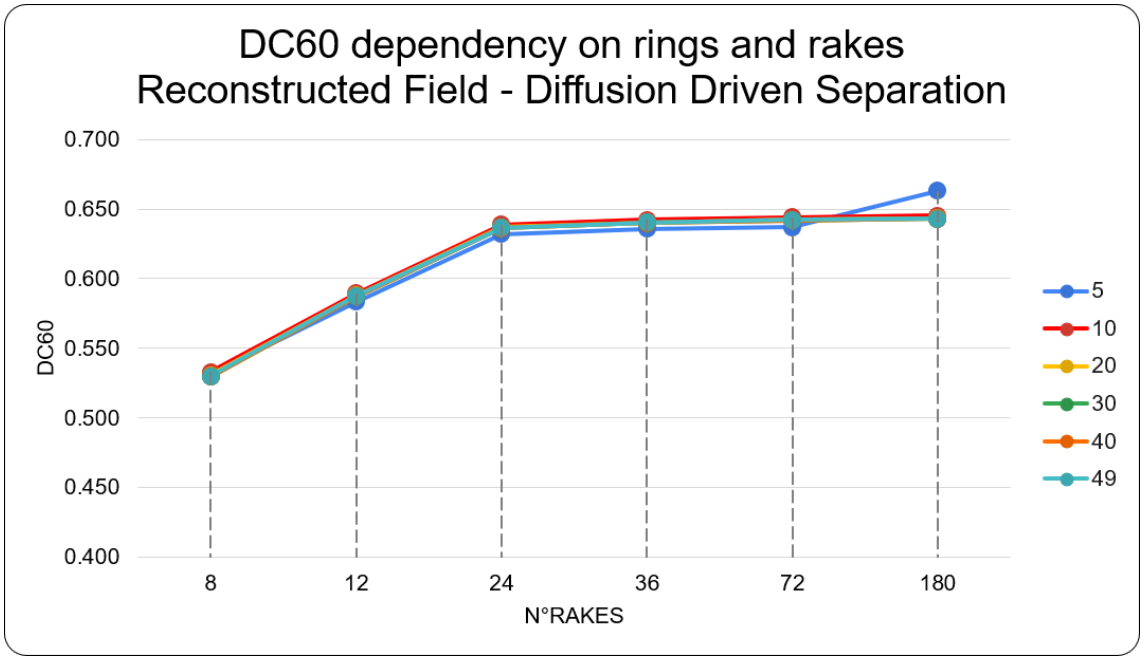


Figure 4-12 CFD reconstructed pressure field at different resolutions of rakes and rings.

Table 4-7 Comparison between reconstructed flowfield DC60 and ground truth flowfield DC60.

RANS 1 DSI, COMPRESSIBLE DC60		Resolution [deg]					
		45	30	15	10	5	2
		N° rakes					
		8	12	24	36	72	180
N° rings	5 rec	0.532	0.584	0.632	0.636	0.637	0.663
	5 real	0.500	0.529	0.565	0.568	0.569	0.570
	10 rec	0.533	0.590	0.639	0.642	0.644	0.645
	10 real	0.503	0.537	0.573	0.576	0.578	0.579
	20 rec	0.531	0.588	0.637	0.641	0.642	0.643
	20 real	0.499	0.532	0.568	0.572	0.573	0.574
	30 rec	0.530	0.587	0.636	0.640	0.642	0.643
	30 real	0.497	0.530	0.566	0.570	0.571	0.572
	40 rec	0.530	0.587	0.636	0.640	0.642	0.643
	40 real	0.497	0.530	0.566	0.570	0.572	0.573
	49 rec	0.530	0.587	0.637	0.640	0.642	0.643
	49 real	0.497	0.530	0.566	0.570	0.571	0.572



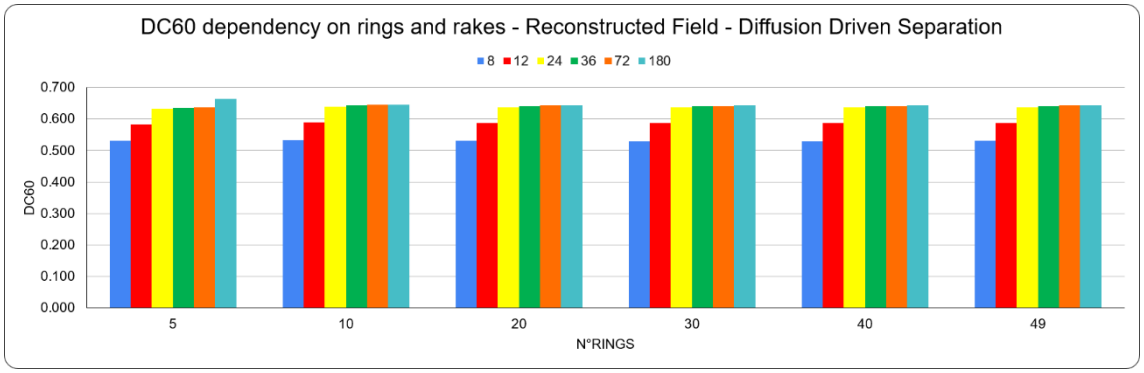


Figure 4-13 Reconstructed flowfield DC60 behaviour.

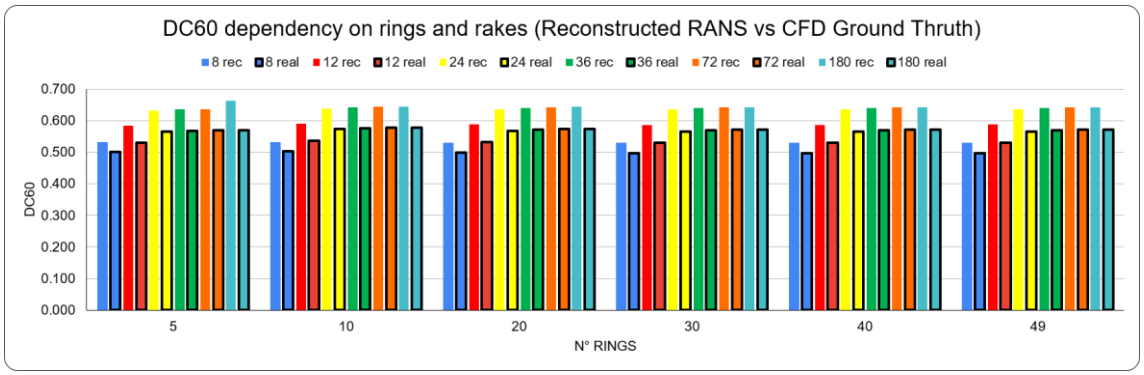


Figure 4-14 Comparison between reconstructed flowfield DC60 and ground truth flowfield DC60.

The angular resolution remains the dominant factor in accurately resolving the flow topology. Configurations relying only on 8 or 12 rakes lack the necessary circumferential density to successfully identify and spatially isolate the ground vortex. Because the vortex is either missed or geometrically misrepresented by these sparse arrays, the resulting $DC60$ metric for these low-rake configurations is lower than that of the denser arrays. As the number of rakes increases, the ground vortex is properly intercepted, stabilising the calculated metric.

Conversely, the data confirms that radial resolution plays a minimal role in this operating state. Consistent with the ground truth analysis, varying the number of rings across the reconstructed grid does not meaningfully affect the resulting $DC60$, proving that distortion tracking in the diffusion-driven condition is governed almost entirely by the angular density of the sampling array.

4.4.2 Attached Flow

The application of the DSI reconstruction method to the attached flow condition further illustrates the sensitivities of deriving total pressure fields from RANS velocity data. A qualitative examination of the reconstructed flowfields, presented in the comparative contours (Figure 4-15, Figure 4-16, full set in Figure B-6), demonstrates the characteristic behaviour of the integration scheme under these optimal design conditions. As observed in the diffusion-driven case, the fundamental mathematical mechanics of the DSI method, integrating boundary conditions from the external casing radially inward towards the spinner, introduce visible numerical artifacts. These artifacts manifest as radial trails of unphysical low-pressure recovery propagating inward from the near-wall low-momentum regions and the ground vortex. Because the attached flow condition features a naturally thinner boundary layer and a distinct low-momentum area on the windward side, the inward propagation of these boundary pressure deficits becomes highly prominent, generating wakes in the reconstructed field that do not exist in the continuous CFD baseline.

The capability of the reconstructed field to accurately capture the ground vortex remains heavily dependent on the angular resolution of the initial virtual instrumentation. In sparsely populated configurations, such as the 8-rake setup,

the wide circumferential gaps prevent the algorithm from establishing accurate boundary conditions for the highly localised ground vortex, causing the feature to be either entirely missed or heavily smeared in the final reconstruction. As the angular density increases to 24, 36, and 72 rakes, the boundary conditions become sufficiently granular to capture the distinct pressure gradients of the vortex. Consequently, the reconstructed contours for these higher-resolution arrays successfully isolate the ground vortex, yielding a visual topography that more closely approximates the high-density baseline.

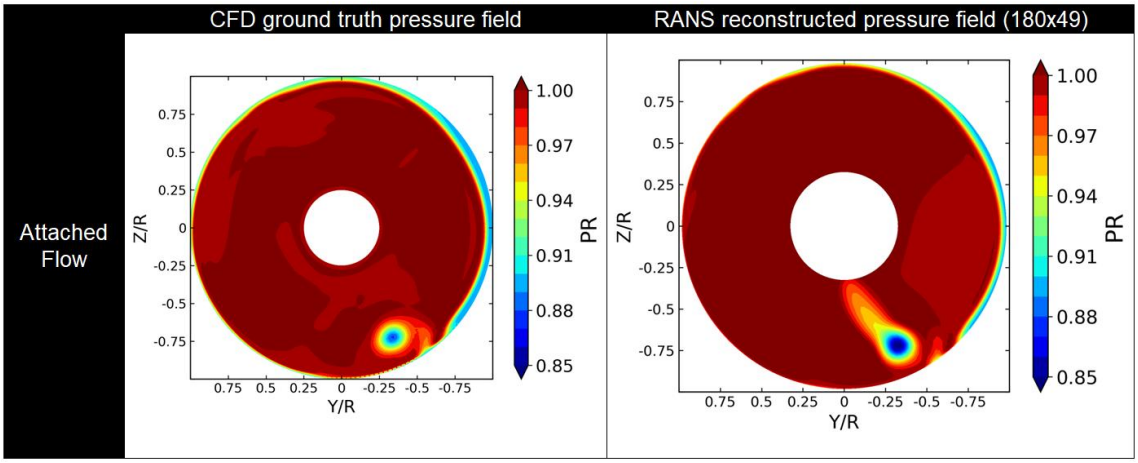


Figure 4-15 Real pressure field vs. Reconstructed pressure field.

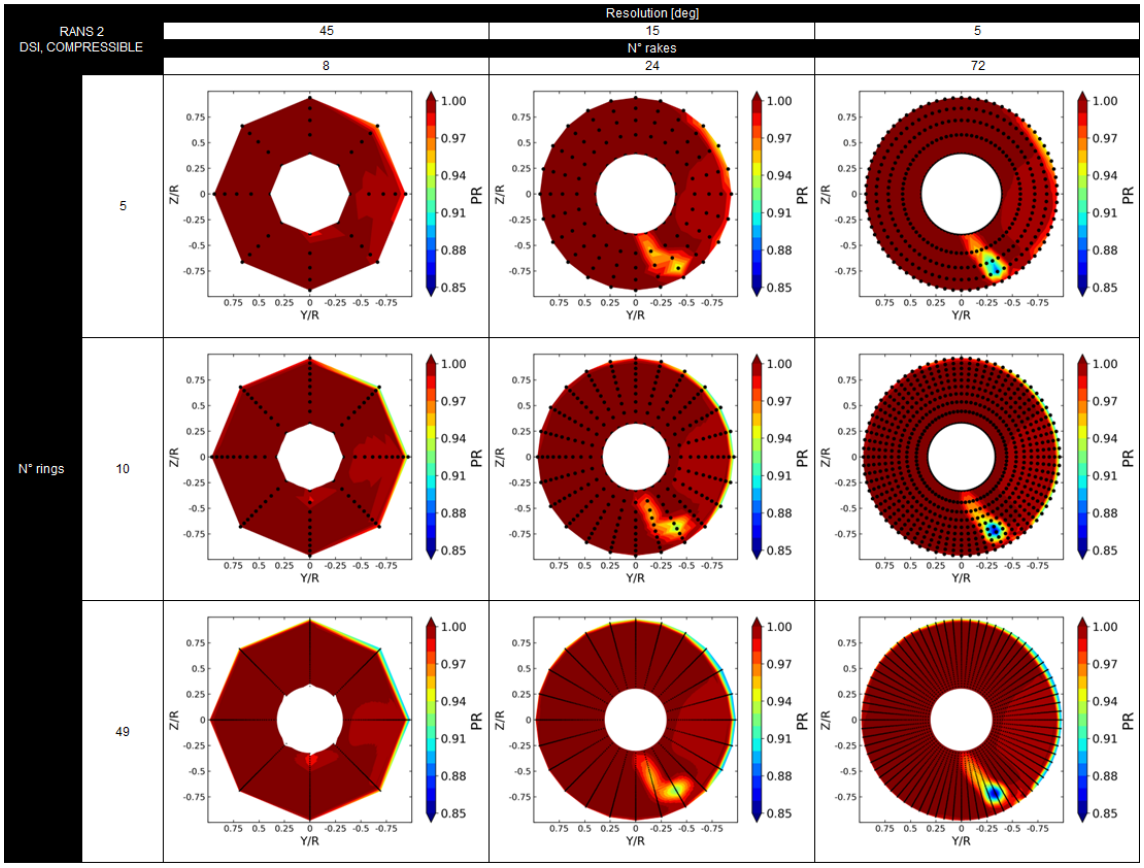


Figure 4-16 CFD Reconstructed pressure field at different resolutions of rakes and rings.

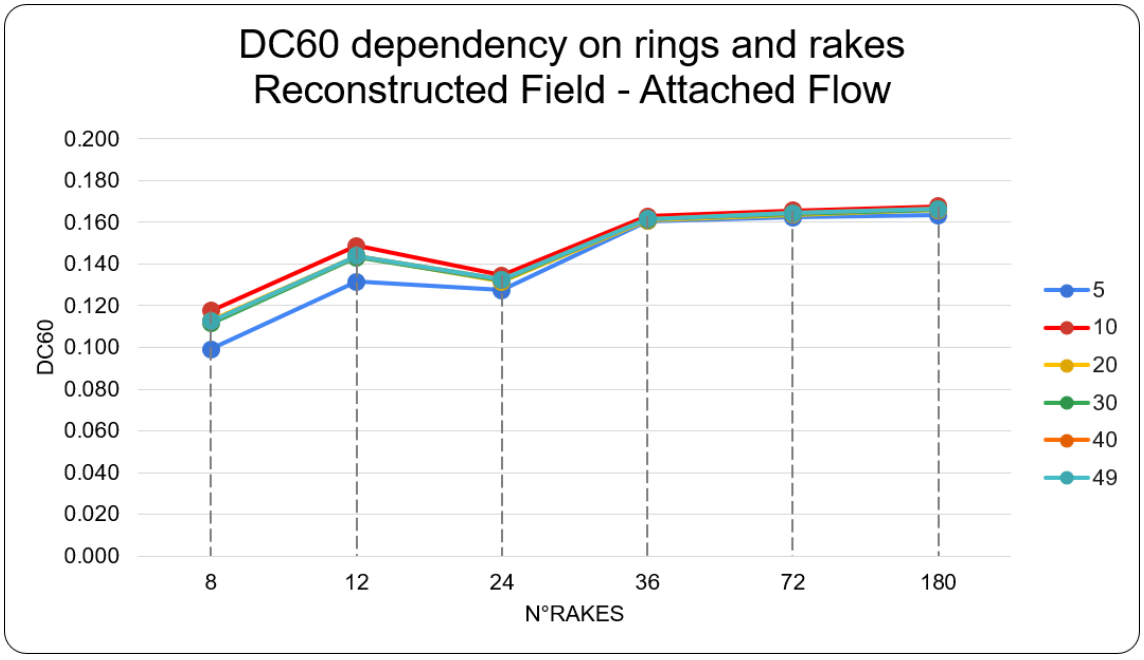
A quantitative assessment of these reconstructions is provided by the bar charts in Figure 4-18 which compare the reconstructed $DC60$ metrics against the ground truth. The data confirms that the DSI reconstruction method consistently overestimates the $DC60$ across the configurations. Similar to previous analyses, radial undersampling plays a secondary role. Beyond a minimum threshold of rings required to map the outer boundary layer, varying the ring count has a negligible impact on the overall distortion metric.

The most striking feature in the quantitative data is the anomalous spike in the calculated $DC60$ for the 12-rake configuration. This unphysical overestimation is the result of a compounding interaction between spatial aliasing and the DSI numerical integration process. As discussed in 4.2.2, a 12-rake configuration intercepts the ground vortex but interpolates it across a broad 30° angular sector, artificially enlarging its footprint at the outer boundary. When the

DSI algorithm uses this artificially broadened low-pressure zone as a starting boundary condition, it integrates this massive deficit radially inward across the entire annulus. The resulting numerical error becomes massively amplified, blanketing a large sector of the engine face in an artificially calculated low-pressure wake. This extensive, purely mathematical pressure drop drastically depresses the average face pressure recovery and heavily skews the distortion assessment, leading to the pronounced and erratic spike observed in the 12-rake $DC60$ charts.

Table 4-8 Comparison between reconstructed flowfield DC60 and ground truth flowfield DC60.

RANS 2 DSI, COMPRESSIBLE DC60		Resolution [deg]					
		45	30	15	10	5	2
		N° rakes					
		8	12	24	36	72	180
N° rings	5 rec	0.099	0.131	0.127	0.161	0.162	0.163
	5 real	0.085	0.088	0.092	0.091	0.092	0.092
	10 rec	0.118	0.149	0.134	0.163	0.166	0.168
	10 real	0.060	0.072	0.060	0.063	0.073	0.075
	20 rec	0.113	0.144	0.132	0.161	0.164	0.166
	20 real	0.058	0.074	0.057	0.067	0.074	0.076
	30 rec	0.112	0.143	0.132	0.161	0.164	0.166
	30 real	0.058	0.075	0.056	0.068	0.074	0.076
	40 rec	0.113	0.144	0.132	0.162	0.164	0.166
	40 real	0.058	0.074	0.056	0.067	0.074	0.076
	49 rec	0.113	0.144	0.132	0.162	0.164	0.166
	49 real	0.058	0.074	0.056	0.066	0.074	0.076



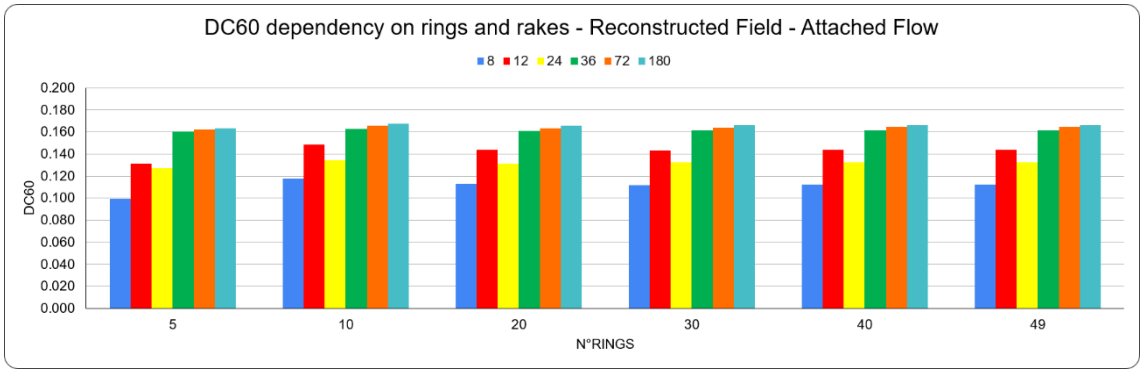


Figure 4-17 Reconstructed flowfield DC60 behaviour.

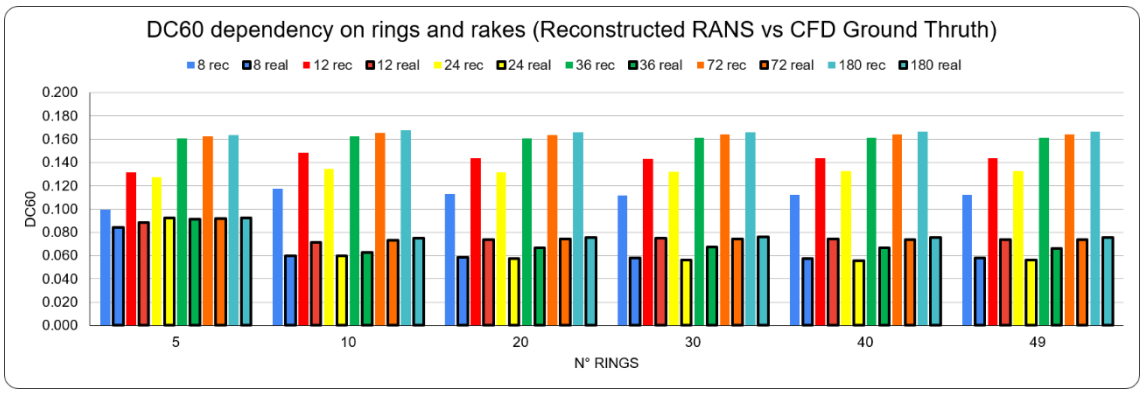


Figure 4-18 Comparison between reconstructed flowfield DC60 and ground truth flowfield DC60.

4.4.3 Shock Driven Separation

The evaluation of the DSI reconstruction method is concluded with the shock-driven separation regime. A qualitative analysis of the reconstructed flowfields, presented in the comparative contour table in Figure 4-20 (full set in Figure B-7), reveals how the extreme aerodynamic conditions of this operating state interact with the mathematical integration scheme. When compared directly to the continuous CFD ground truth (Figure 4-19), it is clear that this specific case is characterised by a very widespread integration error located on the inner side of the primary shock-driven separation zone. Because the DSI algorithm integrates pressure gradients from the external circumference inwards, the severe pressure deficit at the outer casing is numerically dragged radially toward the spinner. This results in an extensive, unphysical trail of low pressure recovery that severely distorts the inner regions of the reconstructed engine face.

The capture of the ground vortex follows a pattern consistent with the previous flow regimes, albeit complicated by the surrounding numerical artifacts. At low angular resolutions, particularly the 8-rake configuration, the sparse circumferential sampling fails to adequately isolate the ground vortex from the massive shock-induced separation area. As the number of rakes increases to 24, 36, and 72, the probes become sufficiently dense to detect the distinct pressure gradients of the vortex, allowing the reconstruction algorithm to capture its geometry more faithfully despite the pervasive radial smearing.

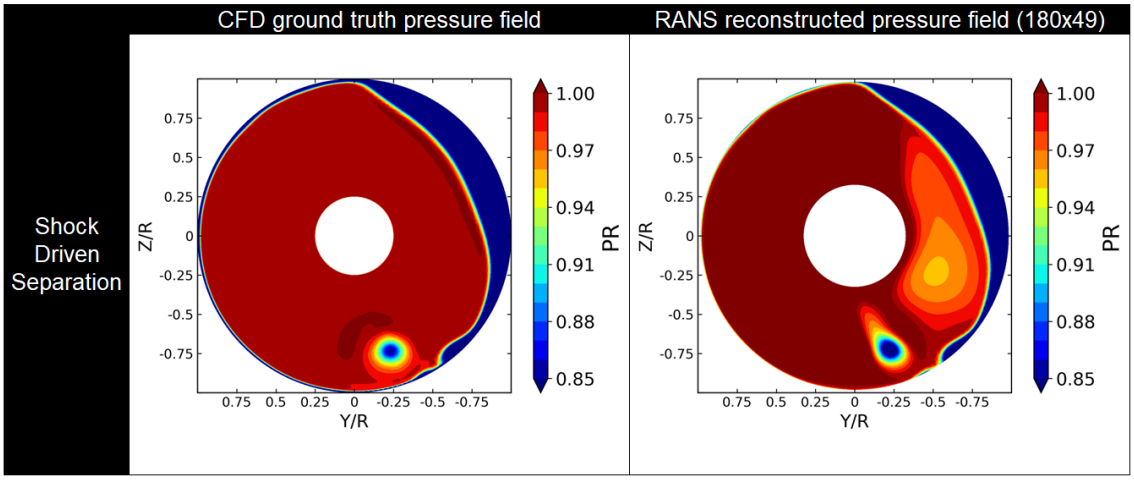


Figure 4-19 Real pressure field vs. Reconstructed pressure field.

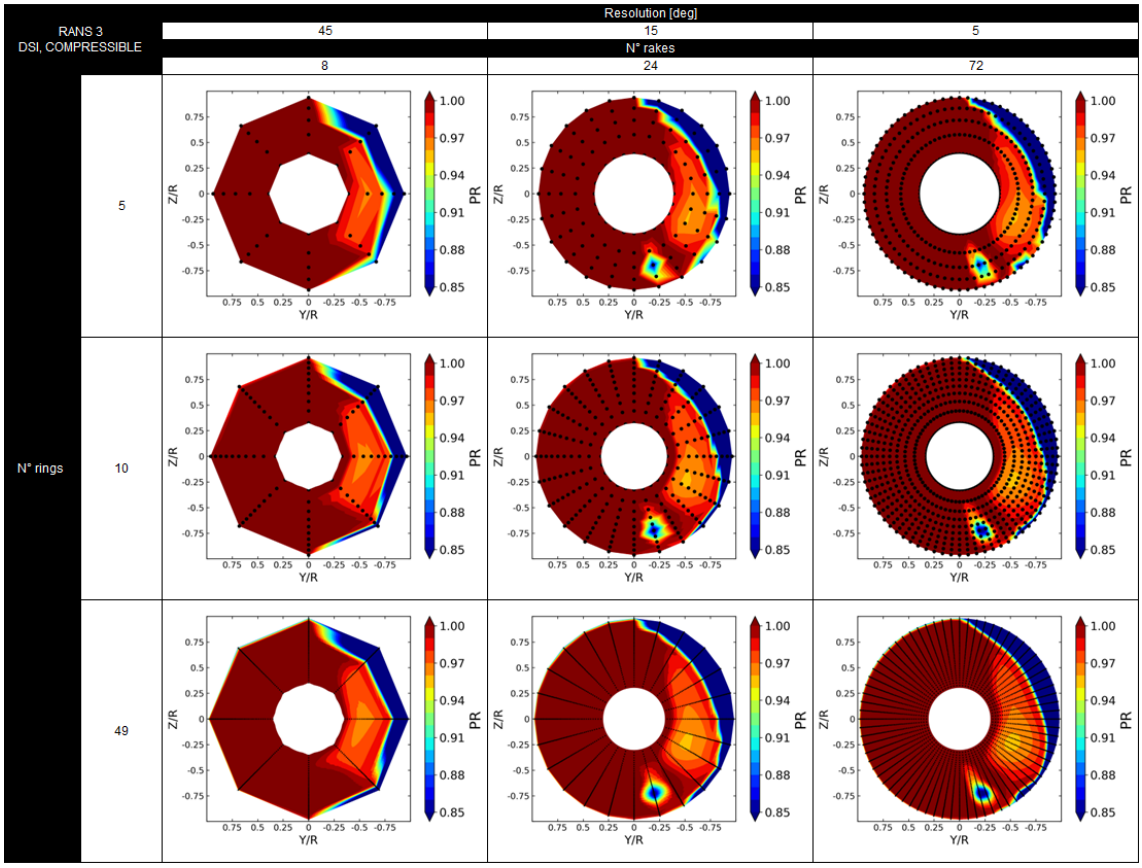
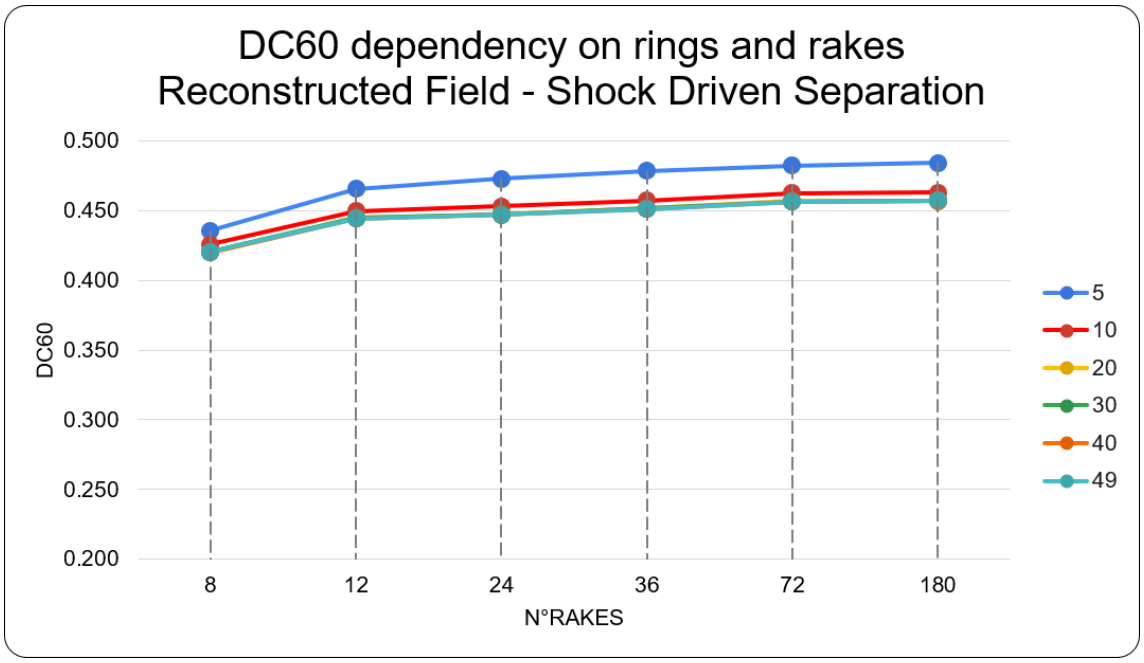


Figure 4-20 CFD reconstructed pressure field at different resolutions of rakes and rings.

The quantitative impact of these numerical artifacts is captured in the corresponding line and bar charts in Figure 4-21 and Figure 4-22. The widespread integration error directly affects the calculation of the distortion coefficient by artificially enlarging the critical low-momentum sector, thereby overestimating and increasing the calculated $DC60$ metric even more significantly than observed in the previous flow conditions. However, despite this absolute measurement offset induced by the integration wakes, the line charts demonstrate a normal, predictable mathematical behaviour expected for the reconstructed case. The calculated metrics follow a stable convergence trend as the angular resolution approaches the ground truth. Consistent with the other regimes, variations in the radial resolution continue to demonstrate a negligible influence on the final $DC60$ value compared to the dominant effect of the rake density.

Table 4-9 Comparison between reconstructed flowfield DC60 and ground truth flowfield DC60.

RANS 3 DSI, COMPRESSIBLE DC60		Resolution [deg]					
		45	30	15	10	5	2
		N° rakes					
		8	12	24	36	72	180
N° rings	5 rec	0.436	0.466	0.473	0.478	0.482	0.484
	5 real	0.319	0.365	0.370	0.374	0.377	0.378
	10 rec	0.426	0.450	0.453	0.457	0.462	0.463
	10 real	0.303	0.350	0.353	0.356	0.358	0.359
	20 rec	0.420	0.445	0.447	0.451	0.457	0.457
	20 real	0.297	0.343	0.346	0.350	0.352	0.352
	30 rec	0.420	0.445	0.447	0.451	0.457	0.457
	30 real	0.296	0.343	0.346	0.349	0.351	0.352
	40 rec	0.420	0.444	0.447	0.451	0.456	0.457
	40 real	0.295	0.342	0.345	0.348	0.350	0.351
	49 rec	0.420	0.444	0.447	0.451	0.456	0.457
	49 real	0.295	0.341	0.345	0.348	0.350	0.350



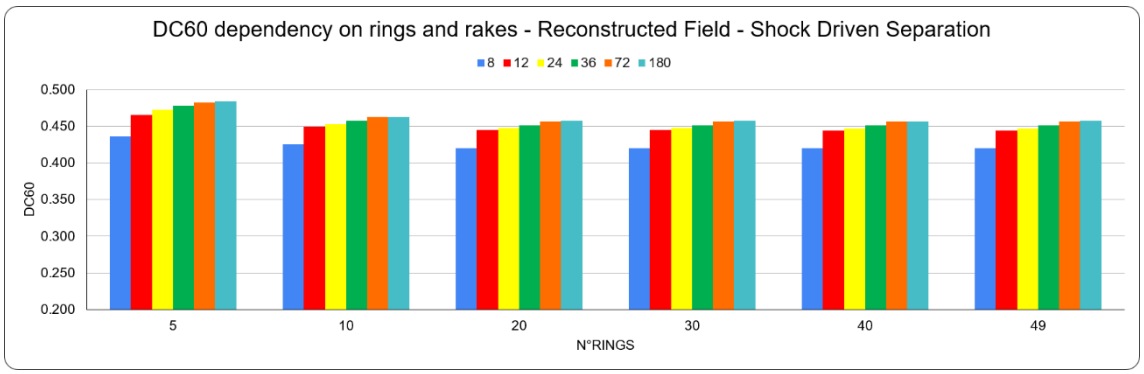


Figure 4-21 Reconstructed flowfield DC60 behaviour.

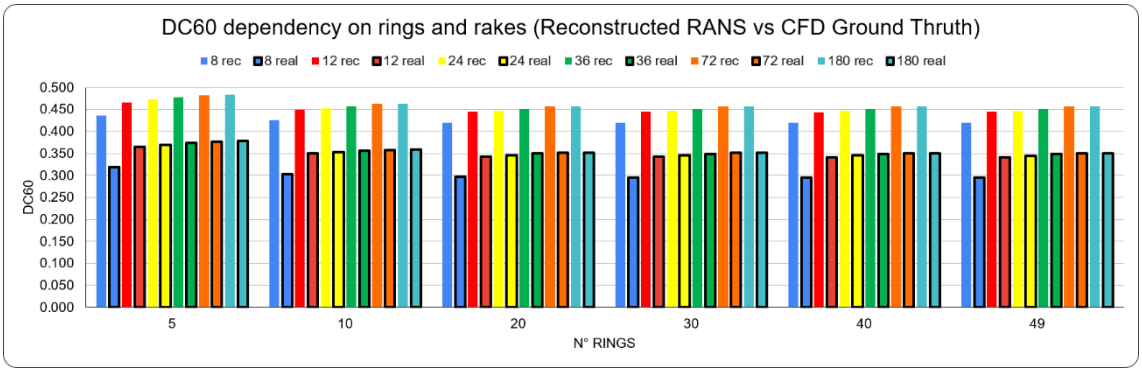


Figure 4-22 Comparison between reconstructed flowfield DC60 and ground truth flowfield DC60.

4.5 Influence of Boundary Conditions

4.5.1 Evenly Distributed Boundary Conditions

To isolate the impact of the initial boundary values from the effects of internal grid resolution, the DSI method was executed using the full-resolution grid *180x49*. For this analysis, only the spatial density of the external boundary conditions was systematically varied. The initial pressure data at the outer casing was extracted using evenly distributed peripheral arrays consisting of 8, 12, 16, and 24 virtual probes. The resulting reconstructed total pressure contours across all three aerodynamic regimes are presented in Figure 4-23. A visual assessment of these flowfields underscores a fundamental characteristic of the integration scheme as the DSI algorithm acts strictly as a mathematical propagator and is therefore entirely reliant on the fidelity of its starting boundary values.

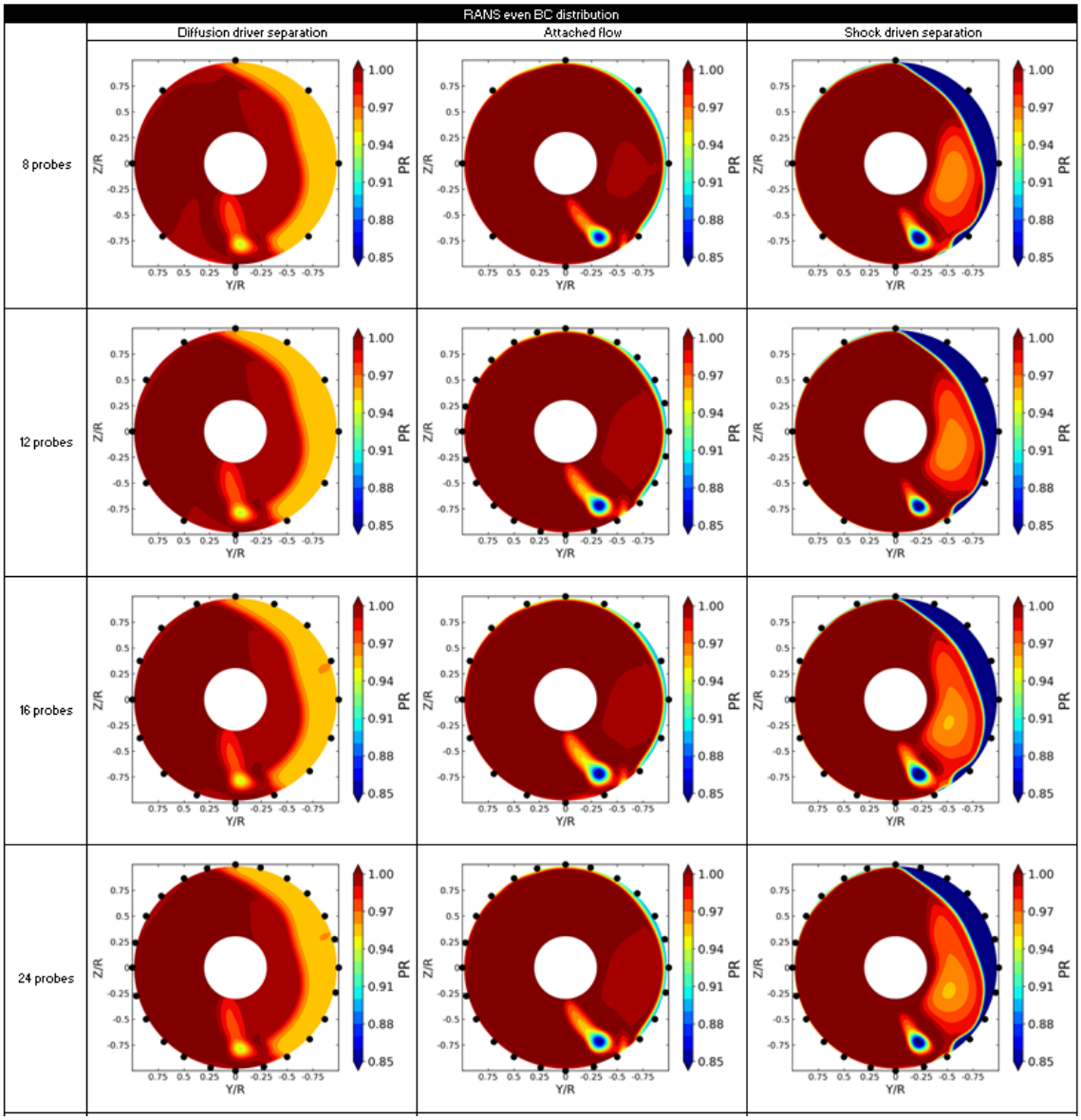


Figure 4-23 Comparative contours with varying probes number.

In both the attached flow and shock-driven separation conditions, the spatial footprint of the numerical error trail and the peak numerical error are slightly reduced compared to the full 180-probe baseline reconstruction, as seen in Figure 4-25. However, this variation must be contextualised within the broader limitations of the DSI approach. The localised differences introduced by altering the boundary conditions are of the same magnitude as, and arguably less relevant than, the absolute delta inherent to the reconstruction method itself, which introduces a baseline error of approximately 0.7. Consequently, the

fundamental integration error remains the dominant factor in the flowfield topology.

Quantitatively, the analysis of the bar charts in Figure 4-25 illustrates a distinct trend in the calculated distortion metrics. Across the tested configurations, the evaluated $DC60$ consistently registers lower than the full-resolution baseline. This underestimation is most pronounced in the sparsest 8-probe configuration, where the wide gaps between boundary inputs likely fail to capture peak pressure deficits at the outer casing, subsequently integrating a less severe flowfield.

Table 4-10 DC60 variation with evenly distributed BC probes.

DC60 - evenly distributed BC			
N° probes	Diffusion Driven Separation	Attached Flow	Shock Driven Separation
8	0.607	0.117	0.433
12	0.628	0.184	0.457
16	0.638	0.162	0.449
24	0.643	0.157	0.456
180	0.643	0.166	0.457

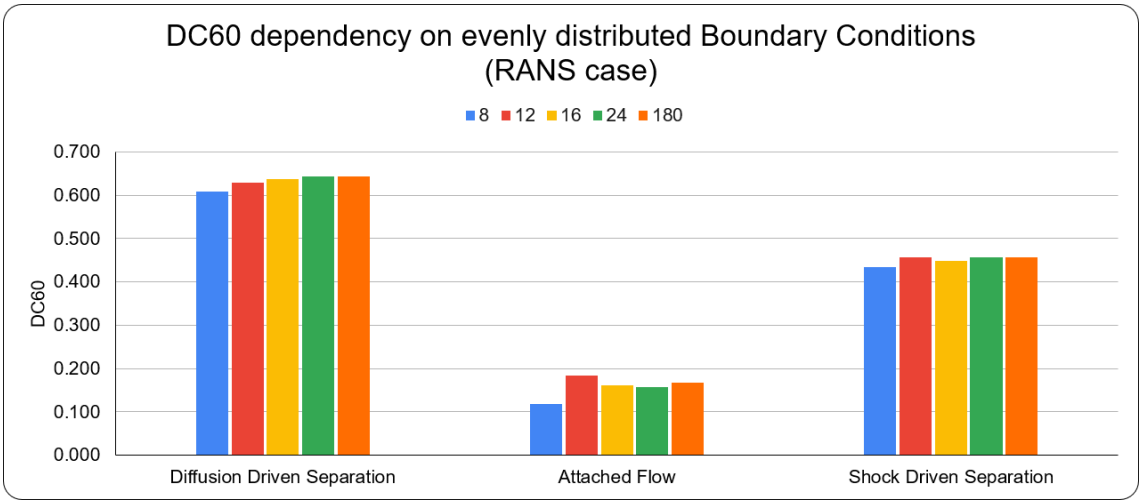


Figure 4-24 DC60 variation with evenly distributed BC probes.

Table 4-11 Absolute Delta between partial BC configurations and the full set of 180 probes.

Δ DC60 (partial-full)			
N° probes	Diffusion Driven Separation	Attached Flow	Shock Driven Separation
8	-0.036	-0.049	-0.024
12	-0.015	0.017	0.000
16	-0.005	-0.005	-0.008
24	0.000	-0.010	-0.001

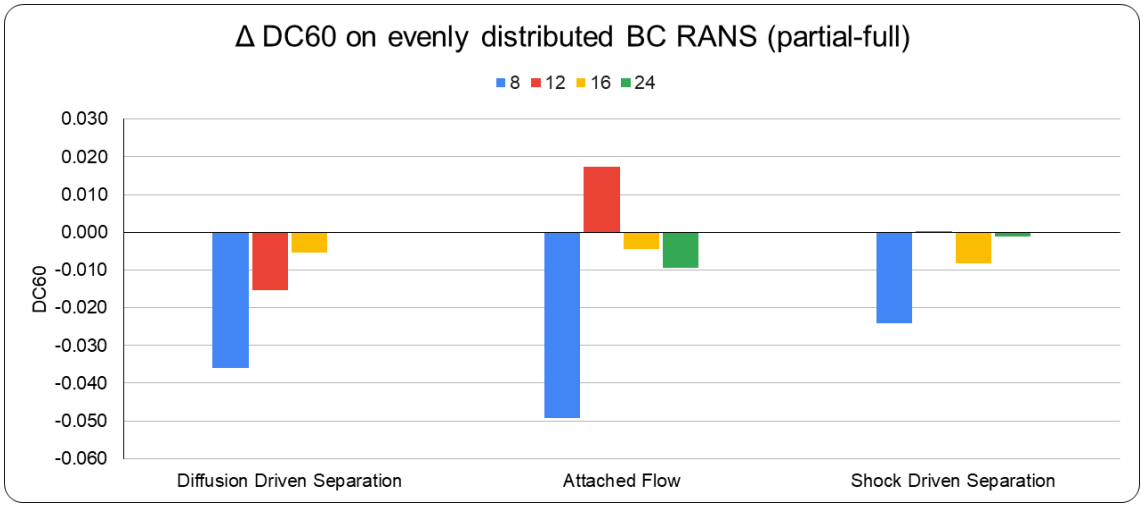


Figure 4-25 Absolute Delta between partial BC configurations and the full set of 180 probes.

Despite these measurable numerical deviations, the findings carry highly positive implications when applied to standard industrial practices. In aerospace engine integration, it is common practice to assume a $DC60$ limit of 0.2 for aerodynamic acceptance, while more conservative design criteria, such as those employed by manufacturers like Rolls-Royce, enforce a stricter limit of 0.1. When evaluating the optimal, attached flow condition, the calculated $DC60$ metric consistently falls within this critical 0.1 to 0.2 acceptability threshold across all tested boundary configurations, as seen in Table 4-10. This inherent stability demonstrates that the precise number of boundary conditions is not a strictly limiting factor for design point validation. Ultimately, this confirms that it is permissible to instrument an intake with a relatively low amount of evenly spaced boundary condition probes while still obtaining the accuracy and reliability required for standard industrial compliance.

4.5.2 Unevenly Distributed Boundary Conditions

Following the analysis of evenly distributed boundary probes, an alternative approach was investigated to determine if strategically clustering the boundary conditions could improve the reconstruction fidelity. Establishing a logical rule for this uneven distribution required identifying the regions along the external casing that experienced the highest rate of change. To achieve this, the circumferential pressure gradient, $\frac{\partial p}{\partial \theta}$, was plotted and analysed, as shown in Figure 4-26.

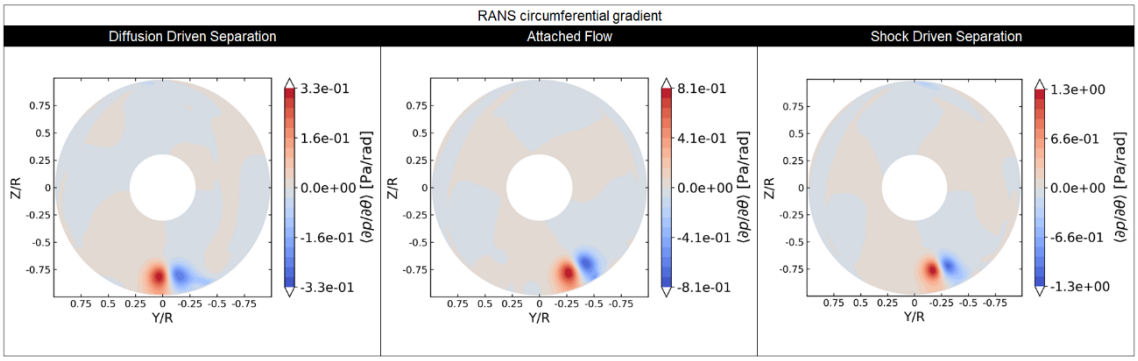


Figure 4-26 Circumferential pressure gradient for each of the flow conditions.

Since the ground vortex induces the strongest pressure gradient along the circumference, its profile was approximated as a Gaussian wave. Based on this approximation, the Full Width at Half Maximum (FWHM) of the ground vortex was assumed 30° from the contours shown, then, using the standard Gaussian width relationship:

$$\sigma = \frac{FWHM}{2\sqrt{2\ln 2}} = 12.7° \tag{4-1}$$

$$Period = 2\sigma = 24° \tag{4-2}$$

To accurately reconstruct this signal without introducing spatial aliasing, the Nyquist-Shannon sampling theorem was applied. The theorem dictates that the spatial resolution must be at least double the highest spatial frequency of the target feature. Consequently, this established a theoretical minimum angular spacing of 12° between probes in the vicinity of the vortex. However, strictly

adhering to this high-density requirement was not feasible for the 8-probe and 12-probe configurations, as clustering them too tightly would leave the remainder of the intake circumference completely unmonitored.

Therefore, the distributions were designed to concentrate sensors around the bottom of the intake, near the ground vortex, while gradually spreading them out across the rest of the annulus. Defining 0° on the right side of the intake and counting counterclockwise, the angular positions for each tested configuration were mapped as in Table 4-12.

Table 4-12 BC probes angular position.

Probes configuration	Angular probe position [°]
8	20, 60, 100, 180, 260, 280, 300, 340
12	10, 40, 70, 100, 150, 210, 250, 266, 282, 298, 314, 340
16	8, 32, 56, 80, 120, 170, 220, 248, 258, 268, 278, 288, 298, 308, 320, 344
24	0, 20, 40, 60, 80, 100, 130, 160, 190, 220, 246, 252, 258, 264, 270, 276, 282, 288, 294, 300, 306, 312, 320, 340

A visual assessment of the resulting reconstructed flowfields (compiled in the contour matrix, Figure 4-27) reveals distinct advantages to this gradient-based distribution strategy. By concentrating the boundary conditions directly across the high-frequency ground vortex, the numerical integration error inherent to the Direct Spatial Integration method is noticeably mitigated. This structural improvement is particularly evident in the attached flow and shock-driven separation conditions. In these cases, the unphysical low-pressure "shade" that propagates inward toward the spinner is visibly smaller compared to the evenly distributed tests. Furthermore, the numerical error trail specifically trailing the ground vortex is significantly reduced in spatial extent, yielding a much cleaner contour map for the attached flow case.

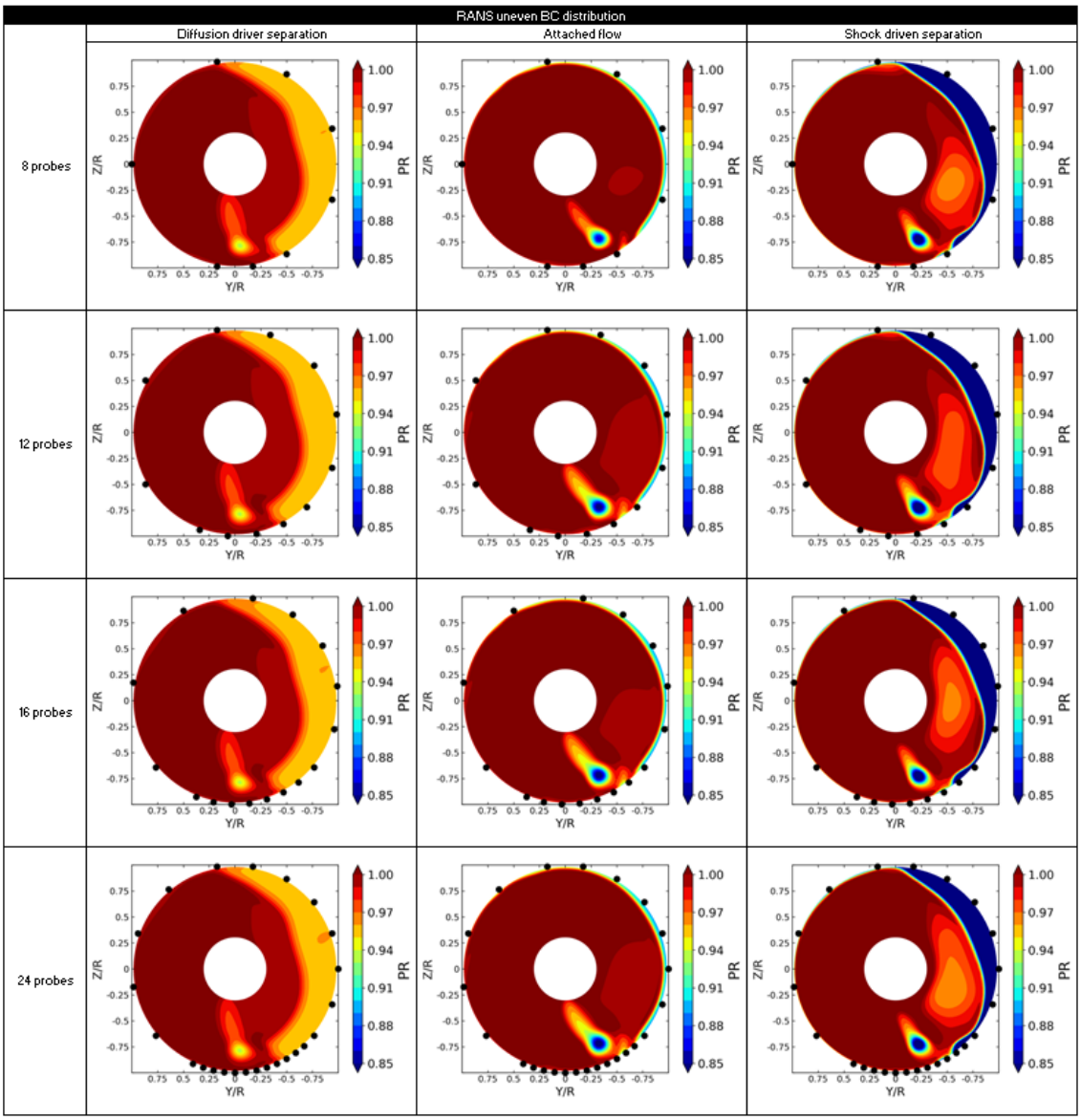


Figure 4-27 Comparative contours with unevenly distributed BC probes.

A visual assessment of the resulting reconstructed flowfields demonstrates that altering the spatial distribution of the boundary probes does not offer a distinct advantage in terms of clearing numerical artifacts. The severe numerical integration error inherent to the Direct Spatial Integration method remains highly prominent across all configurations. The unphysical low-pressure shade that propagates inward toward the spinner does not experience any significant mitigation, and the error trails stemming from both the ground vortex and the main separation zones remain unaltered when compared to the evenly distributed cases.

Quantitative validation from the bar charts in Figure 4-28 and Figure 4-29 confirms that the global impact of this redistribution is minimal. Similarly to the evenly distributed case, the differences in the calculated $DC60$ between the various uneven configurations are small. Because the integration error dominates the pressure field reconstruction regardless of probe placement, changing the circumferential distribution of a low number of probes does not heavily influence the final macro-metric, highlighting that the structural limits of the DSI scheme cannot be circumvented simply by optimising boundary point density.

Table 4-13 DC60 variation with unevenly distributed BC probes.

DC60 - unevenly distributed BC			
N° probes	Diffusion Driven Separation	Attached Flow	Shock Driven Separation
8	0.636	0.112	0.410
12	0.656	0.190	0.419
16	0.652	0.196	0.455
24	0.644	0.199	0.448
180 evenly	0.643	0.166	0.457

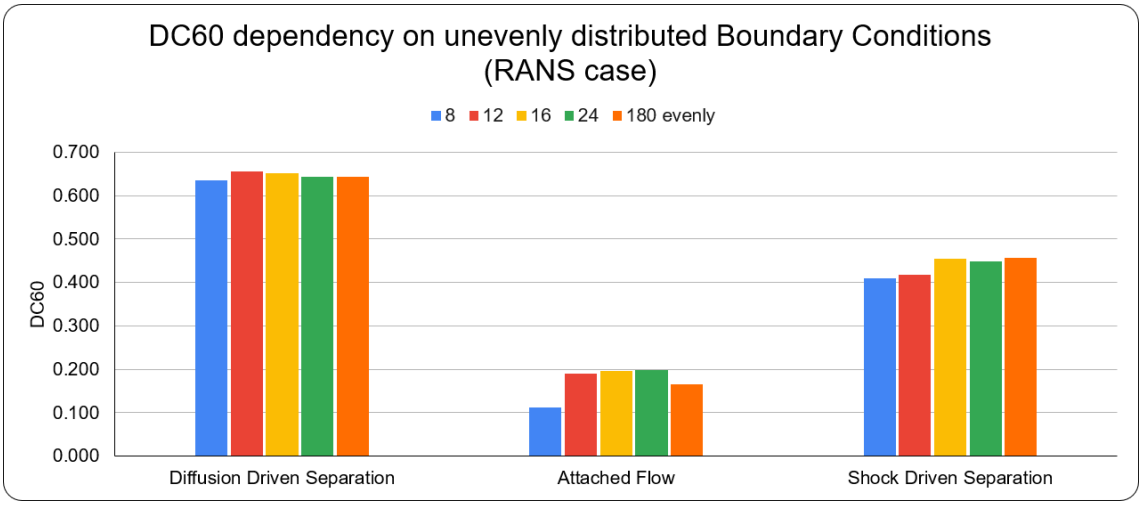


Figure 4-28 DC60 variation with unevenly distributed BC probes.

Table 4-14 Absolute Delta between partial uneven BC configurations and the full set of 180 probes.

Δ DC60 (partial-full)			
N° probes	Diffusion Driven Separation	Attached Flow	Shock Driven Separation
8	-0.008	-0.054	-0.047
12	0.013	0.024	-0.039
16	0.008	0.029	-0.002
24	0.001	0.033	-0.009

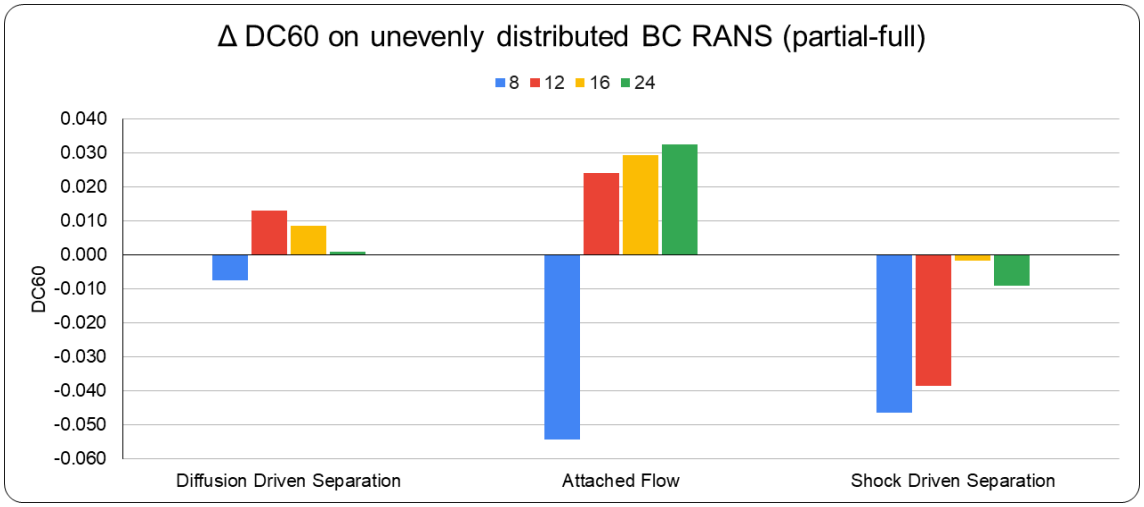


Figure 4-29 Absolute Delta between partial uneven BC configurations and the full set of 180 probes.

4.6 Resolution by Resolution Comparison: Ground Truth vs Reconstructed Pressure Field

To evaluate the reliability of the pressure-from-velocity reconstruction method, a direct resolution-by-resolution comparison was performed. In this analysis, the absolute delta of the distortion coefficient was plotted by subtracting the $DC60$ of the artificially degraded CFD ground truth from the $DC60$ of the identically undersampled reconstructed flowfield. This specific discrepancy encapsulates a complex interaction of three distinct sources of error. First is the intrinsic mathematical error generated by the reconstruction algorithm itself. Second is the geometric error introduced by undersampling the continuous CFD ground truth into a discrete array. Third is the parallel geometric error caused by undersampling the reconstructed flowfield. Because these three phenomena occur simultaneously, comparing the datasets at matching resolutions maps out exactly how physical probe sparsity interacts with mathematical integration flaws.

4.6.1 Diffusion Driven Separation

To determine the true reliability of the reconstruction methodology, it is crucial to first isolate the pure mathematical error by examining the maximum resolution of 180 rakes and 49 rings. At this *180x49* baseline, the geometric undersampling errors are eliminated, leaving only the intrinsic reconstruction penalty. The data reveals that at this full resolution, the reconstruction method overestimates the $DC60$ by an absolute delta of 0.071 as shown in Figure 4-30. This consistent offset is a direct consequence of the DSI scheme, which, as observed in the contour analysis, artificially drags boundary pressure deficits radially inward, thereby enlarging the low-pressure footprint.

When observing the scatter plot and tabular data for the undersampled grids, a misleading phenomenon occurs at the lowest angular resolutions. For the 8-rake configurations, the absolute delta drops significantly to approximately 0.031. This lower discrepancy does not imply that a sparse 8-rake array is more accurate. Instead, it proves that extreme spatial aliasing is masking the true reconstruction error. At 8 rakes, the angular gaps are so vast that the virtual probes entirely miss the ground vortex in both the ground truth and the reconstructed datasets. If this

peak distortion event is ignored in both calculations, the resulting delta is artificially suppressed.

As the angular density is increased to 24 rakes and beyond, the virtual probes successfully intersect the ground vortex. Consequently, the absolute delta experiences a rise before stabilising into a predictable plateau between 0.07 and 0.09, perfectly mirroring the pure mathematical error identified in the full-resolution baseline. This asymptotic stabilisation affirms the reliability of the reconstruction technique. It proves that once a sufficient angular resolution is achieved to capture localised phenomena, the reconstructed pressure field behaves entirely consistently with the baseline physics, burdened only by the predictable mathematical offset of the DSI algorithm.

Finally, radial undersampling plays a secondary role, with one notable exception. The data exhibits a sharp spike to an absolute error at the extreme configuration of 180 rakes and only 5 rings. This anomaly highlights that pairing maximum circumferential density with severe radial starvation actually compounds the DSI integration error, exacerbating the inward smearing of the boundary layer deficits. However, provided that a moderate radial density of at least 10 rings is maintained, the reconstruction remains robust, reliable, and fundamentally reflective of the true aerodynamic conditions.

Table 4-15 Absolute Delta DC60 resolution by resolution. Reconstructed flowfield DC60 - ground truth.

RANS 1 DSI, COMPRESSIBLE Δ DC60 (rec-CFD each resol)		Resolution [deg]					
		45	30	15	10	5	2
		N° rakes					
		8	12	24	36	72	180
N° rings	5	0.031	0.054	0.067	0.068	0.068	0.093
	10	0.030	0.053	0.066	0.066	0.066	0.067
	20	0.031	0.056	0.069	0.069	0.069	0.069
	30	0.032	0.057	0.070	0.071	0.071	0.071
	40	0.032	0.057	0.070	0.070	0.070	0.070
	49	0.033	0.057	0.071	0.071	0.071	0.071

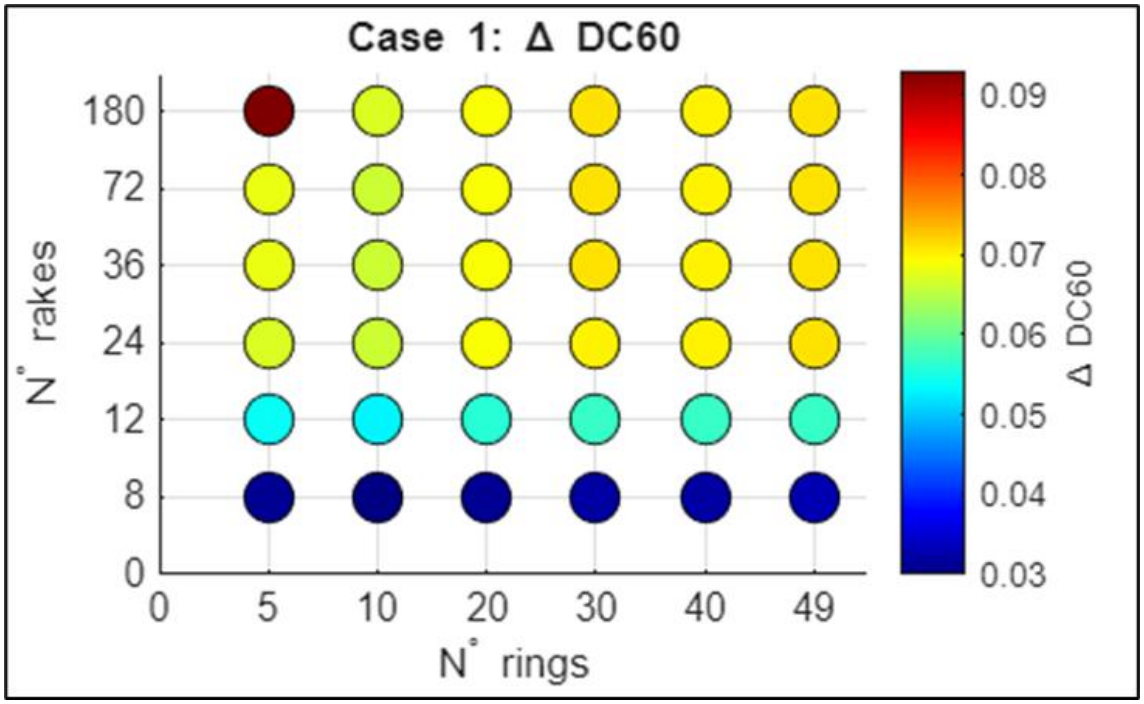


Figure 4-30 Absolute Delta DC60 resolution by resolution. Reconstructed flowfield DC60 - ground truth.

4.6.2 Attached Flow

Extending the resolution-by-resolution analysis to the attached flow condition further illuminates the operational characteristics of the DSI scheme. By calculating the absolute delta between the identically undersampled reconstructed flowfield and the CFD ground truth, the interplay between spatial aliasing and mathematical integration errors is once again explicitly mapped out.

The magnitude of this discrepancy is very similar, on average, to what was recorded in the diffusion-driven separation regime. At the maximum resolution of 180 rakes by 49 rings, where geometric undersampling errors are entirely factored out, the reconstruction overestimates the $DC60$ by an absolute delta of approximately 0.090 as shown in Figure 4-31. This is close the 0.071 offset previously established in the diffusion-driven case.

The consistency of this offset across two fundamentally different aerodynamic states, one dominated by massive flow separation and the other representing an optimal, primarily attached flow, is a critical finding. It

demonstrates that the numerical artifacts inherent to the DSI algorithm, specifically the radial inward smearing of boundary layer deficits and ground vortex signatures, scale predictably, this steady overestimation possibly represents an intrinsic reconstruction delta.

Furthermore, the behaviour at coarser resolutions perfectly aligns with this systemic understanding. At sparse geometric configurations, such as the 8-rake arrays, the absolute delta fluctuates and can appear artificially low because the physical blind spots of the virtual probes fail to resolve the compact ground vortex in both the ground truth and the reconstructed datasets. However, as the angular density crosses the structural threshold necessary to capture localised phenomena, typically 24 rakes and above, the delta stabilises toward that intrinsic offset. This reaffirms that once the spatial resolution is adequate to capture the true flow topology, the reconstruction method is exceptionally stable.

Table 4-16 Absolute Delta DC60 resolution by resolution. Reconstructed flowfield DC60 - ground truth.

RANS 2 DSI, COMPRESSIBLE Δ DC60 (rec-CFD each resol)		Resolution [deg]					
		45	30	15	10	5	2
		N° rakes					
		8	12	24	36	72	180
N° rings	5	0.015	0.043	0.035	0.070	0.070	0.071
	10	0.057	0.077	0.075	0.100	0.092	0.093
	20	0.054	0.070	0.074	0.094	0.089	0.090
	30	0.054	0.068	0.076	0.094	0.090	0.090
	40	0.055	0.069	0.077	0.095	0.090	0.091
	49	0.055	0.070	0.076	0.095	0.090	0.091

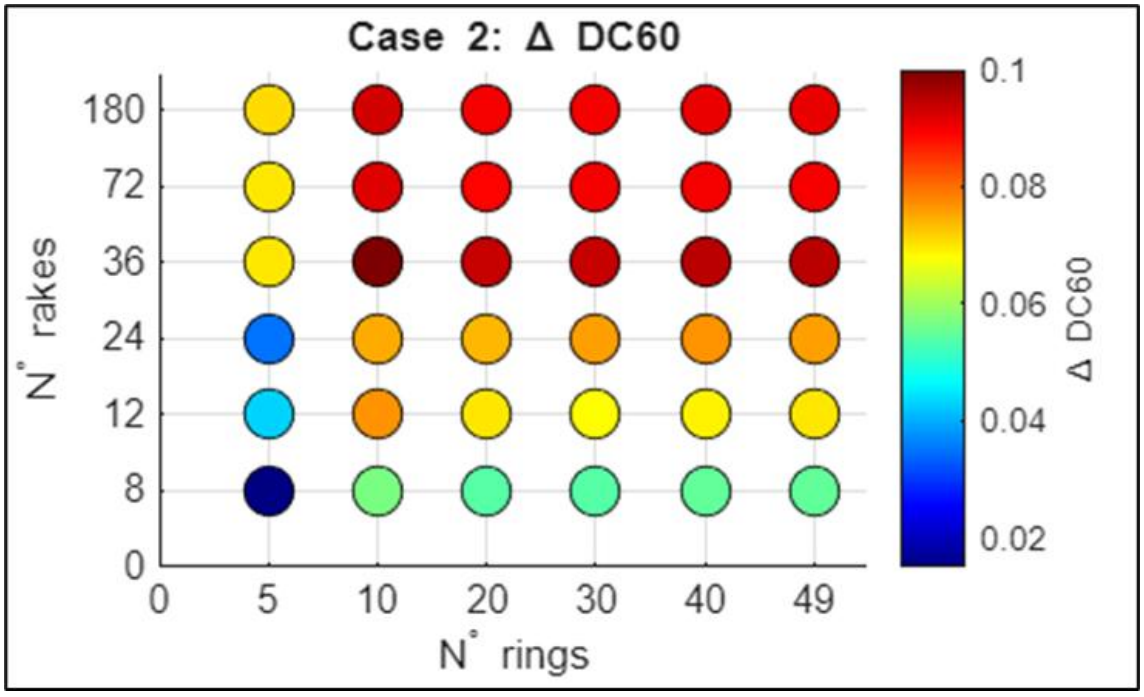


Figure 4-31 Absolute Delta DC60 resolution by resolution. Reconstructed flowfield DC60 - ground truth.

4.6.3 Shock Driven Separation

To complete the resolution-by-resolution assessment, the same comparison was applied to the extreme suction conditions of the shock-driven separation regime. When isolating the full-resolution baseline *180x49* to eliminate geometric downsampling variables, the data reveals that the delta explicitly due to the reconstruction process is, on average, higher than the other two cases, settling at an absolute overestimation of 0.107 (reflecting a reconstructed metric of 0.457 against the ground truth value of 0.350). The primary explanation for this higher baseline penalty lies in the qualitative behaviour of the DSI reconstruction in the presence of strong shock waves. Because the algorithm marches radially inward, the severe total pressure deficits originating at the outer intake casing from shock-induced boundary layer detachment are numerically dragged across the entire annulus toward the spinner. This mathematical trailing effect forms expansive low-pressure wakes that do not exist in reality, thereby compounding the overestimation of the distortion footprint and driving the overall metric upward. Despite this elevated baseline discrepancy, the reconstruction demonstrates a

crucial characteristic that affirms its underlying physical and numerical reliability. The results are the most consistent between different spatial resolutions out of all the operating regimes tested. Across the entire matrix of downsampled grids, the absolute delta is exceptionally uniform as shown in Figure 4-32, with the variation becoming entirely negligible for configurations using more than 12 rakes.

This consistency is a consequence of the physical topology of the shock-driven regime. Unlike the diffusion-driven and attached flow states, where the ground vortex dominates and can slip entirely between sparse virtual probes, the shock-driven state is heavily governed by a large, expansive separation zone along the windward side. Because the structural footprint of this distortion is geometrically broad, it does not suffer from severe spatial aliasing. The sampling grid successfully captures the boundary of the separation bubble even at moderate densities, allowing the DSI scheme to generate an identically stable, albeit conservative, pressure map across nearly all configurations.

The caveats of the discrepancy at constant matching resolutions must be understood as the combined stacking of three concurrent mathematical phenomena: the fundamental reconstruction error of the DSI algorithm, the error related to the undersampling of the CFD ground truth and the error related to the undersampling of the reconstructed pressure field. While the global integration artifacts mean that the raw numerical output requires calibration before it can achieve absolute parity with physical measurements, the mathematical consistency across varying grid densities proves that the reconstruction technique is highly reliable even under transonic operating conditions.

Table 4-17 Absolute Delta DC60 resolution by resolution. Reconstructed flowfield DC60 - ground truth.

RANS 3 DSI, COMPRESSIBLE Δ DC60 (rec-CFD each resol)		Resolution [deg]					
		45	30	15	10	5	2
		N° rakes					
		8	12	24	36	72	180
N° rings	5	0.117	0.101	0.103	0.104	0.105	0.106
	10	0.123	0.100	0.100	0.101	0.104	0.104
	20	0.124	0.102	0.101	0.102	0.105	0.105
	30	0.125	0.102	0.101	0.102	0.105	0.105
	40	0.125	0.102	0.102	0.103	0.106	0.106
	49	0.126	0.103	0.102	0.103	0.107	0.107

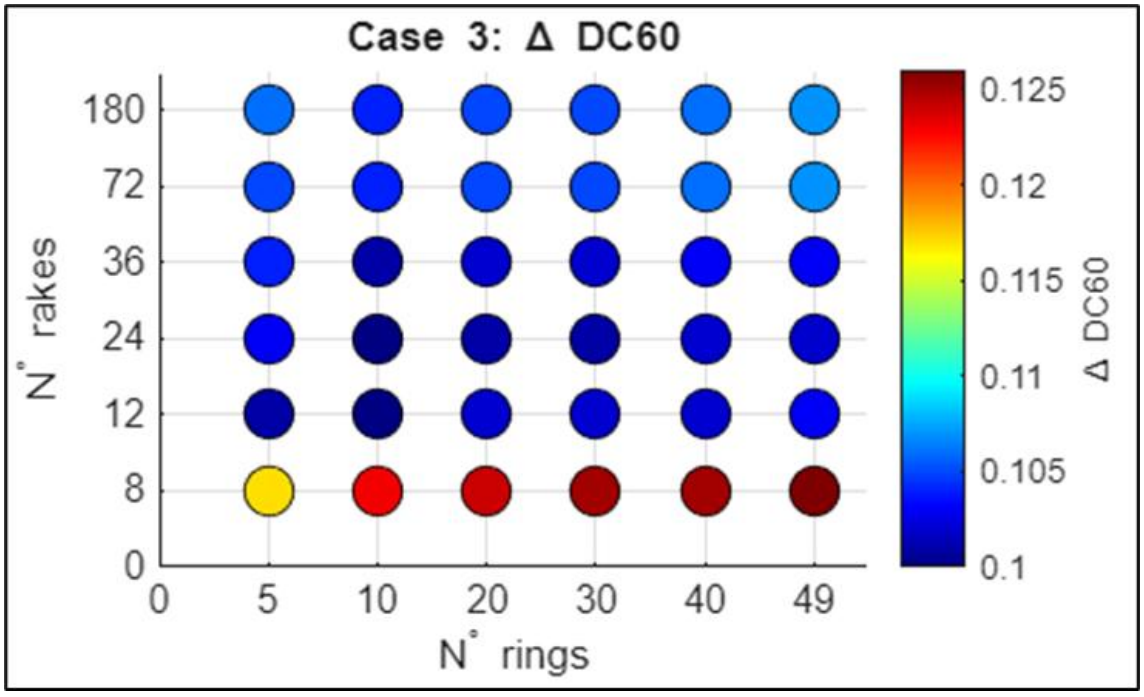


Figure 4-32 Absolute Delta DC60 resolution by resolution. Reconstructed flowfield DC60 - ground truth.

4.7 Real Case Simulation: Notional Physical Rake vs Reconstruction Method

To simulate a real-case testing scenario within the different flow regimes, the full-resolution reconstructed flowfield is compared directly against varying configurations of notional physical rakes. In evaluating these results, it is essential to remember that the typical measuring errors and aerodynamic blockage effects introduced by physical probes are absent in this numerical baseline. Since these detrimental physical effects are absent in this idealised computational baseline, the performance of physical rakes in a real-world testing environment would be even more compromised than these data suggest. Furthermore, while the simulation explores highly dense configurations, installing anything approaching these dense grids in a physical intake is entirely impossible without completely choking the engine flow. The analysis relies on calculating the delta by subtracting the undersampled ground truth $DC60$, representing the physical rake readings, from the full-resolution reconstructed $DC60$, which represents the optical measurement approach.

4.7.1 Diffusion Driven Separation

When examining the data, the full-resolution reconstructed pressure field yields a $DC60$ of 0.643. In contrast, evaluating the flow using a simulated industry-standard 8-rake by 5-ring physical configuration produces a ground truth $DC60$ of merely 0.500. This generates a substantial delta of 0.143 as shown in Figure 4-33, explicitly illustrating how a conventional, sparse physical rake severely underestimates the true peak distortion intensity. Because the wide angular gaps of the 8-rake setup completely miss the highly localised ground vortex, the overall non-uniformity is structurally masked. As the simulated physical rake density is progressively increased to 12 and 24 rakes at 5 rings, the ground truth $DC60$ rises and consequently, the calculated delta narrows down.

As the virtual instrumentation approaches the theoretical limit of 180 rakes and 49 rings, the ground truth $DC60$ plateaus at its maximum full resolution value of 0.572. At this point, spatial aliasing is entirely eliminated, and the delta converges to a stable 0.071. This remaining discrepancy represents the intrinsic

mathematical overestimation of the Direct Spatial Integration scheme, which artificially drags boundary pressure deficits radially inward. However, despite this known numerical offset, the chart and numbers clearly demonstrate that relying on sparse physical rakes results in a dangerous underrepresentation of the distortion field. The reconstruction method, by successfully resolving the critical ground vortex that sparse grids miss, ultimately provides a much more comprehensive and conservative assessment of aerodynamic compatibility.

Table 4-18 Absolute Delta DC60 real case simulation. Full resolution reconstructed flowfield DC60 - Undersampled ground truth.

RANS 1 DSI, COMPRESSIBLE Δ DC60 (max res rec-CFDvariable)		Resolution [deg]					
		45	30	15	10	5	2
		N° rakes					
		8	12	24	36	72	180
N° rings	5	0.143	0.114	0.079	0.075	0.074	0.073
	10	0.141	0.106	0.070	0.067	0.065	0.065
	20	0.144	0.111	0.075	0.072	0.070	0.069
	30	0.146	0.113	0.077	0.074	0.072	0.071
	40	0.146	0.113	0.077	0.073	0.072	0.071
	49	0.146	0.113	0.077	0.074	0.072	0.071

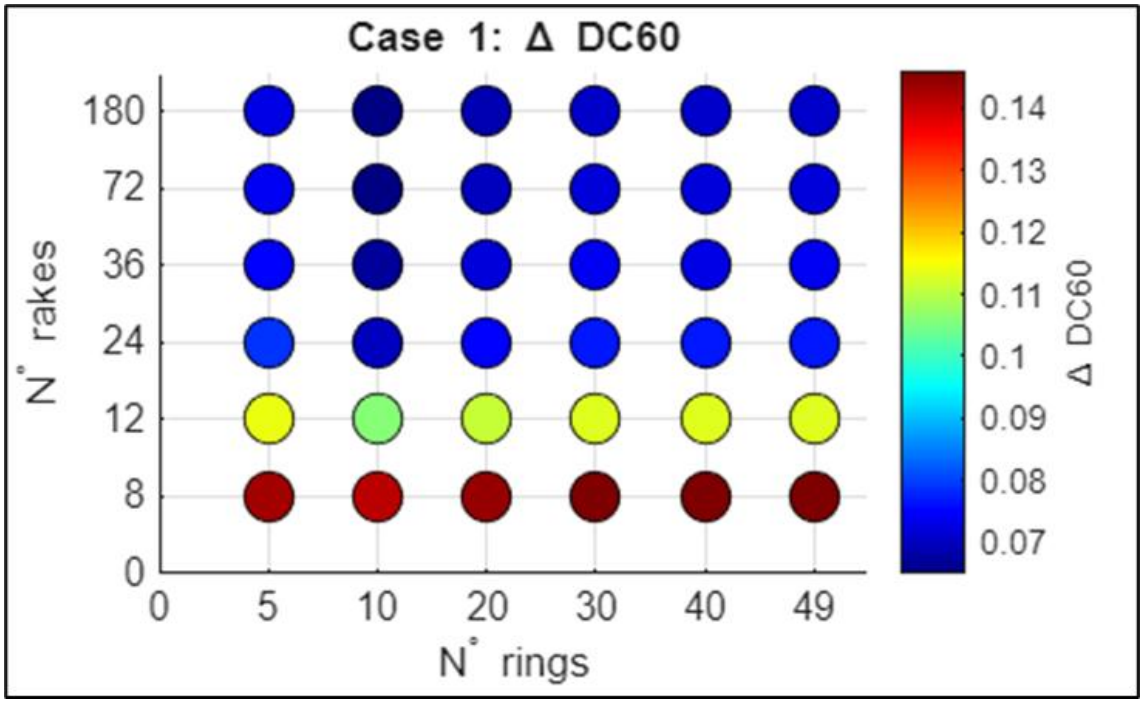


Figure 4-33 Absolute Delta DC60 real case simulation. Full resolution reconstructed flowfield DC60 - Undersampled ground truth.

4.7.2 Attached Flow

For this optimal operating state, the full-resolution reconstructed pressure field establishes a baseline $DC60$ of 0.166. When the flow is evaluated using the notional industry-standard 8-rake by 5-ring physical configuration, the ground truth yields a $DC60$ of only 0.085. Subtracting this sparse physical representation from the velocimetry reconstruction results in a substantial delta of 0.081. This pronounced discrepancy highlights a severe structural blind spot as the wide angular spacing of an 8-rake array completely fails to intersect the ground vortex that characterises the attached flow regime. Because the virtual instrumentation entirely misses this critical peak distortion event, the standard physical configuration inherently masks the true severity of the flow non-uniformity.

As the simulated physical rake density is artificially increased, the virtual probes begin to intersect the ground vortex, though spatial aliasing continues to skew the results. While these denser arrays improve the capture of localised phenomena, achieving such circumferential resolution with intrusive hardware remains practically unfeasible in a real testing environment. When pushing the notional physical instrumentation to the theoretical limit of 180 rakes and 49 rings, the ground truth $DC60$ stabilises at 0.076. At this physically impossible density, where geometric undersampling is eliminated, the delta between the reconstructed baseline and the ground truth settles at 0.090. This enduring discrepancy isolates the intrinsic mathematical overestimation of the Direct Spatial Integration scheme, which tends to artificially amplify near-wall low-momentum regions and vortex signatures as they are integrated radially inward. Despite the numerical offset, by successfully capturing the small-scale aerodynamic structures that standard physical rakes are virtually guaranteed to miss, the velocimetry reconstruction approach provides a safer, more comprehensive assessment of flow distortion.

Table 4-19 Absolute Delta DC60 real case simulation. Full resolution reconstructed flowfield DC60 - Undersampled ground truth.

RANS 2 DSI, COMPRESSIBLE Δ DC60 (max res rec-CFDvariable)		Resolution [deg]					
		45	30	15	10	5	2
		N° rakes					
		8	12	24	36	72	180
N° rings	5	0.082	0.078	0.074	0.075	0.074	0.074
	10	0.106	0.095	0.107	0.103	0.093	0.092
	20	0.108	0.093	0.109	0.100	0.092	0.091
	30	0.108	0.091	0.110	0.099	0.092	0.090
	40	0.109	0.092	0.111	0.100	0.092	0.091
	49	0.108	0.092	0.110	0.100	0.093	0.091

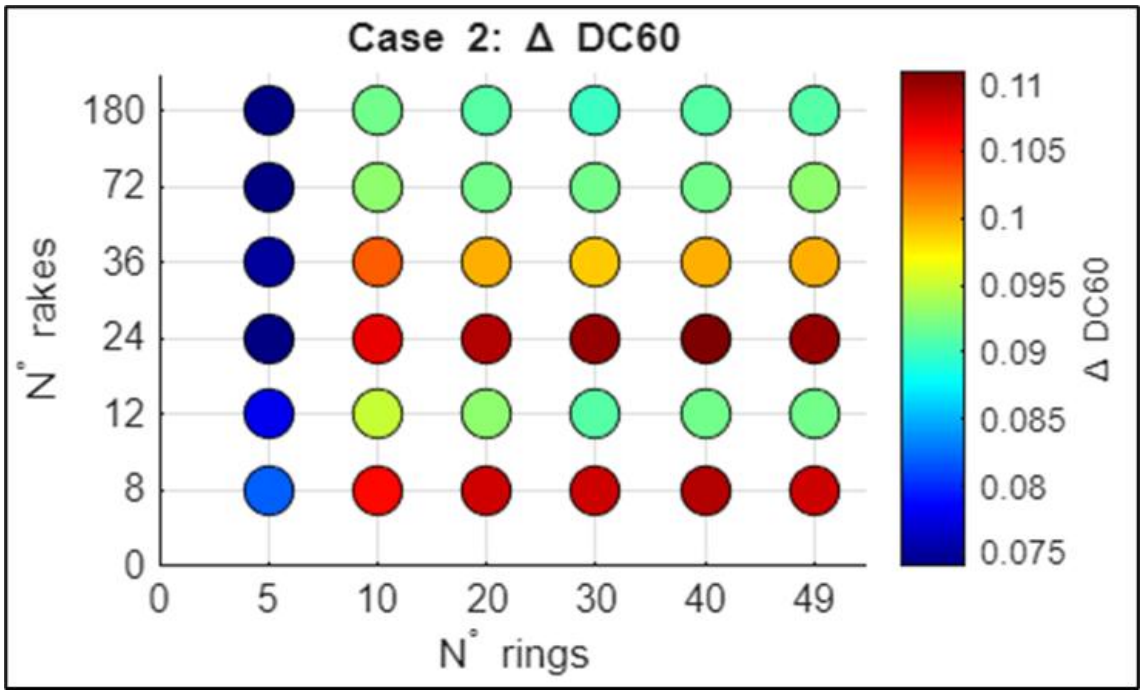


Figure 4-34 Absolute Delta DC60 real case simulation. Full resolution reconstructed flowfield DC60 - Undersampled ground truth.

4.7.3 Shock Driven Separation

Examining the numerical data shown in Figure 4-35, the notional industry-standard configuration of 8 rakes by 5 rings generates a substantial delta of 0.138. As the simulated physical instrumentation is artificially densified, the measurement capture improves and the data begins to converge. Progressing to a 12-rake by 5-ring configuration abruptly narrows the delta to 0.092, while further increasing the angular resolution to 24 or 36 rakes causes the discrepancy to stabilise around 0.110.

When the notional physical rake is pushed to the physically impossible maximum resolution of 180 rakes and 49 rings, geometric undersampling and spatial

aliasing are entirely eradicated. At this theoretical limit, the delta settles at a steady 0.107. As previously established in the resolution-by-resolution analysis, this enduring 0.107 offset characterises the intrinsic mathematical overestimation of the Direct Spatial Integration scheme. In the presence of strong shock waves, the algorithm drags severe total pressure deficits radially inward across the annulus from the outer casing, creating expansive low-pressure wakes that numerically inflate the overall metric.

Table 4-20 Absolute Delta DC60 real case simulation. Full resolution reconstructed flowfield DC60 - Undersampled ground truth.

RANS 3 DSI, COMPRESSIBLE Δ DC60 (max res rec-CFDvariable)		Resolution [deg]					
		45	30	15	10	5	2
		N° rakes					
		8	12	24	36	72	180
N° rings	5	0.138	0.092	0.087	0.083	0.080	0.079
	10	0.155	0.107	0.104	0.101	0.099	0.098
	20	0.160	0.114	0.111	0.107	0.106	0.105
	30	0.161	0.114	0.111	0.108	0.106	0.105
	40	0.162	0.115	0.112	0.109	0.107	0.106
	49	0.162	0.116	0.112	0.109	0.107	0.107

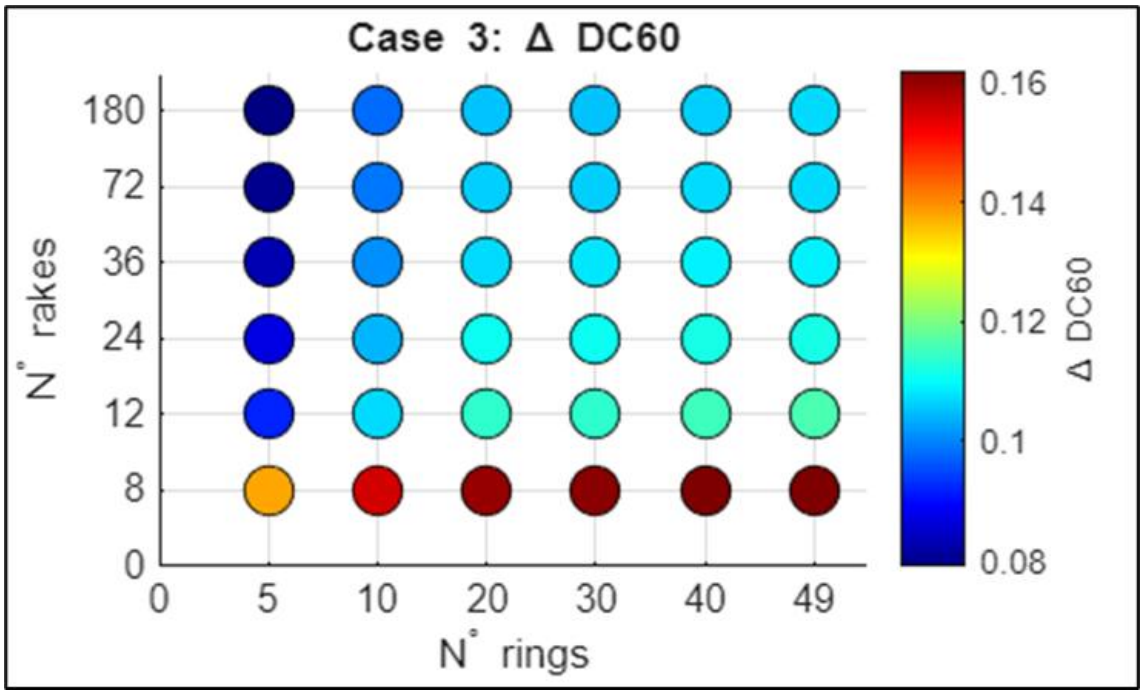


Figure 4-35 Absolute Delta DC60 real case simulation. Full resolution reconstructed flowfield DC60 - Undersampled ground truth.

4.8 Conclusions about the DC60 Study on Reconstructed Flowfields

The comprehensive evaluation of the total pressure field reconstruction method demonstrates that this non-intrusive approach successfully yields a flowfield representation that is significantly closer to reality than what can be captured by standard discrete instrumentation. By eliminating the spatial blind spots inherent to sparse physical arrays, the reconstruction algorithm reliably resolves the critical localised aerodynamic structures, such as ground vortices and separation bubbles, that conventional rakes routinely miss.

When comparing the full-resolution reconstructed flowfield against the absolute theoretical limits of the ground truth, a distinct mathematical offset emerges. This delta, which isolates the intrinsic overestimation of the Direct Spatial Integration scheme, scales predictably across the operating envelope. The discrepancy measures approximately 0.07 for the diffusion-driven separation case, rises to 0.09 for the attached flow, and reaches 0.11 during shock-driven separation. This progression indicates that the mathematical offset increases with the Mass Flow Capture. However, because this overestimation is highly consistent and predictable across varying virtual grid densities, it constitutes a systematic offset rather than a random error, allowing it to be accounted for in future experimental setups.

It is also crucial to emphasise that reverting to conventional physical rakes does not equate to achieving zero error. The study proves that standard physical configurations inherently suffer from severe spatial undersampling. When standard sparse arrays are compared against the continuous ground truth, they generate their own significant geometric errors, yielding deltas such as 0.07 in the diffusion case, an anomalous near-zero reading in the attached flow that can be attributed to the sheer luck of probe placement relative to a compact vortex, and 0.03 in the shock-driven regime. Consequently, physical rakes carry an unavoidable measurement penalty, which in a real-world scenario would be further exacerbated by aerodynamic blockage and probe interference effects, absent in this idealised numerical baseline.

Ultimately, the viability of the reconstruction method depends heavily on the specific flow regime in exam. In attached, nominal flow conditions where the baseline aerodynamic distortion is minimal, the predictable 0.09 mathematical offset translates into a substantial relative error. Conversely, in highly severe off-design conditions, most notably the diffusion-driven separation regime, the absolute distortion is massive, meaning the 0.07 delta represents a relatively small and acceptable margin of error. This distinction perfectly highlights the industrial value of the technique. By employing velocimetry reconstruction, aerodynamicists can conduct extensive, cost-effective testing of critical, highly distorted off-design conditions without the financial burden, setup time, and aerodynamic choking risks associated with installing dense physical rakes inside the engine intake.

4.9 Aeromechanics

4.9.1 Influence of Low Resolution on CFD Ground Truth for HEI

4.9.1.1 Diffusion Driven Separation

A comparative analysis of the Harmonic Excitation Index between the full-resolution CFD baseline *180x49* and the undersampled grid *8x5* reveals a different sensitivity to spatial resolution than what was observed with the $DC60$ metric. When evaluating whether industrial standard physical rakes possess inherent flaws or limitations compared to the real flow, two primary aeromechanical constraints must be acknowledged. First, this numerical comparison represents an idealised scenario, it lacks the aerodynamic blockage and probe interference effects that would further degrade real-world physical measurements. Second, the spatial sparsity of an 8-rake configuration enforces a limitation dictated by the Nyquist theorem. Because a physical 8-rake array provides only eight circumferential sampling points, it is blind to any aerodynamic forcing above the 4th Engine Order. Any high-frequency flow-induced vibrations caused by smaller, complex aerodynamic structures are structurally masked from the instrumentation. However, when analysing the resolvable low-order harmonics, the undersampled array performs remarkably well. A visual and numerical assessment of the HEI_n in Figure 4-36 demonstrates that the *8x5* notional physical rake captures the primary aeromechanical forcing footprint with surprisingly high fidelity.

In the diffusion-driven separation regime, the dominant structural threat is a massive 1st EO excitation, particularly concentrated at the outer radial rings (Rings 4 and 5), where the HEI_n peaks near 0.08. This peak is driven by the diffusion-driven separation, which creates a massive block of low-momentum flow on the windward side of the intake. While the 8-rake configuration failed to pinpoint the localised peak deficits of the ground vortex for the $DC60$ calculation due to spatial aliasing, it successfully maps the broad, once-per-revolution pressure wave required for the Fourier transform.

Since the Fourier decomposition extracts the global sinusoidal shape of the circumferential pressure distribution rather than hunting for isolated peak deficits, the sparse physical rake is sufficient to define the primary 1st and 2nd EO forcing magnitudes. Consequently, the dataset proves that are physical rakes are reliable for identifying large-scale, low-order harmonic excitations typical of massive flow separations.

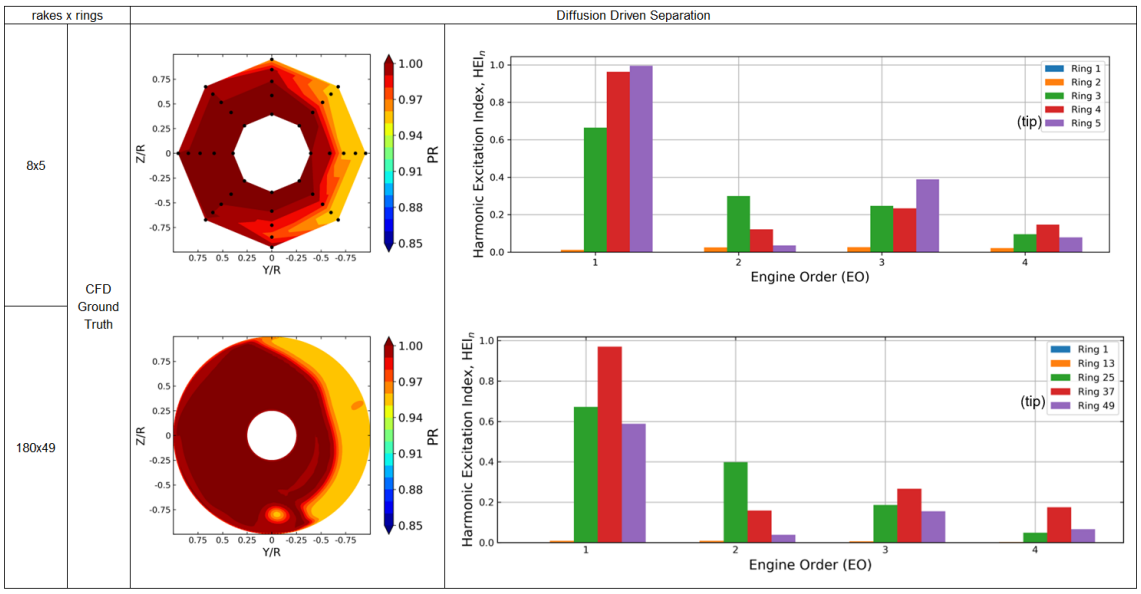


Figure 4-36 HEI undersampled Ground truth vs. Full resolution Ground truth.

4.9.1.2 Attached Flow

In contrast to the diffusion-driven separation regime, the attached flow condition exposes a vulnerability in the spatial resolution of standard industrial rakes. While the overall harmonic excitation magnitudes in this regime are inherently lower, with the peak HEI_n reaching only around 0.030 compared to the 0.090 observed previously, the divergence between the continuous high-resolution ground truth and the discrete *8x5* rake configuration is noticeable. A comparative analysis of the HEI_n bar charts in Figure 4-37 reveals information loss, specifically isolated within the 3rd and 4th radial rings across all the EO. The most alarming discrepancy occurs in the 2nd EO of Ring 4, where the full-resolution CFD predicts a dominant excitation peak, while the undersampled rake registers a negligible forcing value.

This under-prediction is a consequence of the rake's spatial sparsity failing to capture a highly localised flow structure. In the attached flow regime, the primary aeromechanical threat is not a broad, low-momentum separation wave, but rather a tightly concentrated ground vortex. As confirmed by the total pressure contours, this vortex is physically small and localised within the radial bands corresponding to Rings 3 and 4. Because the spatial gap between the eight physical rakes is wider than the circumferential footprint of the vortex itself, the discrete probes completely straddle the phenomenon. Consequently, the physical instrumentation is essentially blind to the vortex. When the Fourier decomposition is applied to this undersampled data, it lacks the total pressure deficit required to reconstruct the true harmonic waves.

This finding highlights a fundamental limitation of standard physical rakes as they are inadequate for capturing high-intensity, small-scale distortion structures. Relying solely on traditional intrusive measurements in this regime would provide a false sense of security, as the instrumentation underestimates the true harmonic excitation imposed on the fan blades.

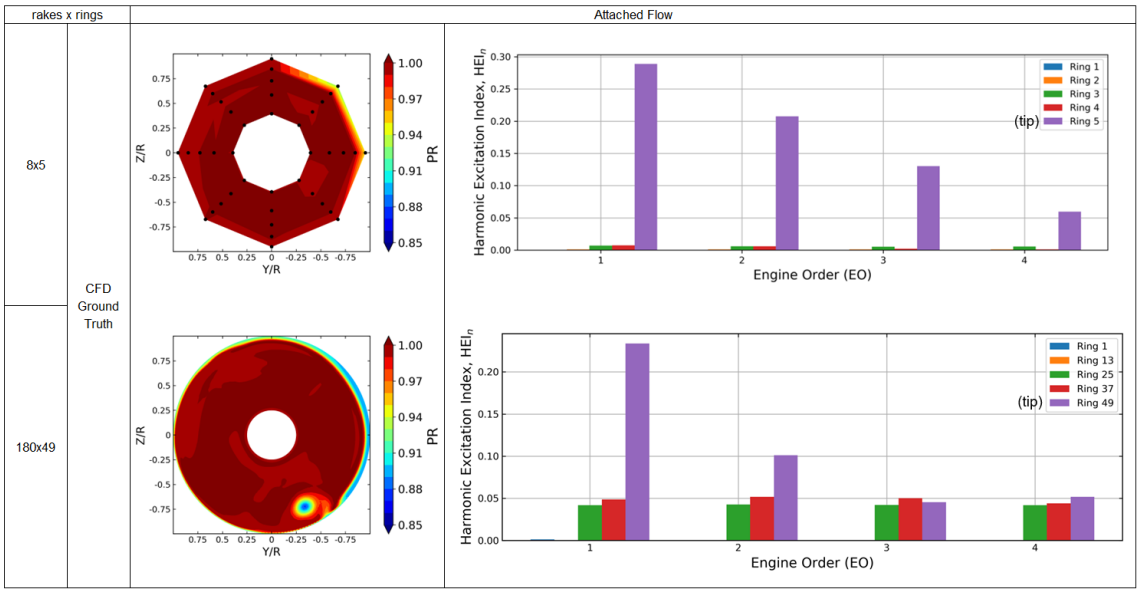


Figure 4-37 HEI undersampled ground truth vs. Full resolution ground truth.

4.9.1.3 Shock Driven Separation

For this last flow condition in Figure 4-38, in the outermost radial band, the notional physical rake overpredicts the magnitude of both the 1 EO and 2 EO harmonic excitations. Moving radially inward to Ring 3 exposes a failure to capture secondary aerodynamic effects. The high-resolution ground truth clearly identifies a distinct 1st EO and 2nd EO excitation. However, the discrete rake registers this forcing as virtually zero. Like the failure observed in the attached flow regime, this indicates the presence of a vortex aligned with the spatial gaps between the eight physical probes.

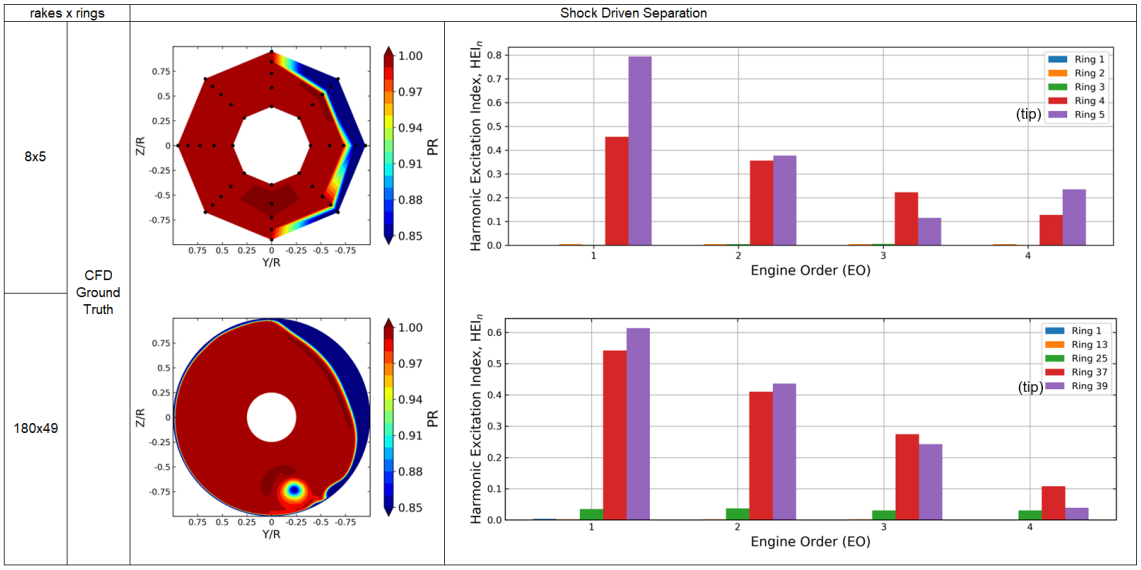


Figure 4-38 HEI undersampled ground truth vs. Full resolution ground truth.

4.9.2 HEI Comparison: Ground Truth vs Reconstructed Pressure Field

4.9.2.1 Diffusion Driven Separation

To evaluate the aeromechanical reliability of the reconstruction, a resolution-by-resolution comparison of the Harmonic Excitation Index is performed for the diffusion-driven separation regime. When comparing the full-resolution ground truth against the reconstructed pressure fields across varying azimuthal resolution, the general trend for the Engine Order excitation remains fundamentally consistent. In both the actual flowfield and all reconstructed cases, the dominant structural threat is heavily concentrated at the 1st EO, primarily affecting the outer radial rings, followed by a rapid decay in harmonic excitation at higher engine orders.

In the ground truth, the innermost radial bands (Rings 1, 2, and 3) experience negligible harmonic excitation, remaining at nearly zero across all engine orders. Conversely, the reconstructed fields artificially report distinct harmonic excitations on these inner rings. Since the integration scheme calculates pressure by marching radially inward from the outer casing, the total pressure deficits characteristic of the outer-boundary separation are mathematically dragged toward the hub. This creates a non-physical inward propagation of the low-pressure footprint, resulting in an artificial forcing load on the inner rings that is entirely absent in the actual physical flow.

Comparing the reconstructions resolution-by-resolution confirms that this mathematical offset is a product of the algorithm itself, rather than spatial starvation. The 180, 40, and 20-rake reconstructed fields yield nearly identical HEI profiles, proving that the magnitude inflation and the inner-ring forcing are intrinsic to the radial integration scheme and remain stable across high and medium rake densities. The 8-rake reconstruction exhibits the exact same magnitude overestimations and inward propagation artifacts on the inner rings, but its diagnostic capability is abruptly truncated. As dictated by the Nyquist limit, the 8-rake array chart cuts off completely at the 4th Engine Order, rendering it

entirely blind to any higher-frequency excitations that the denser arrays can still theoretically process.

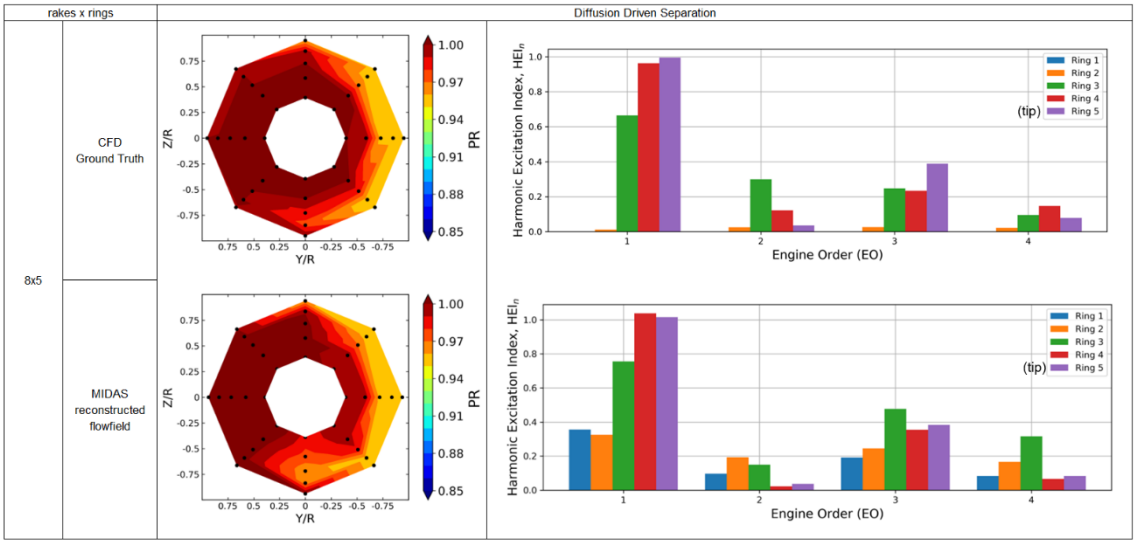


Figure 4-39 8x5 HEI analysis CFD ground truth vs reconstructed field.

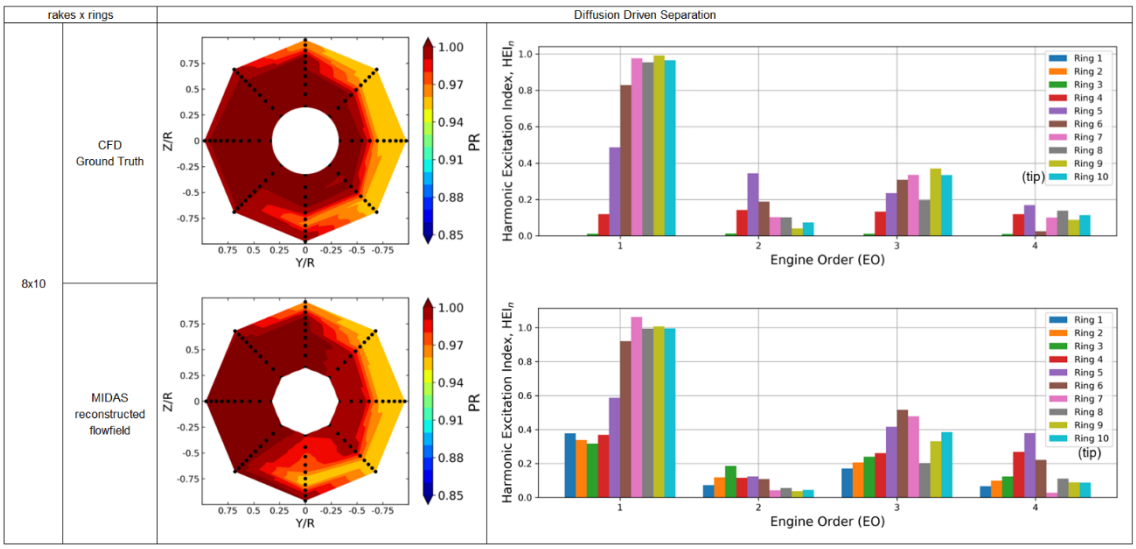


Figure 4-40 8x10 HEI analysis CFD ground truth vs reconstructed field.

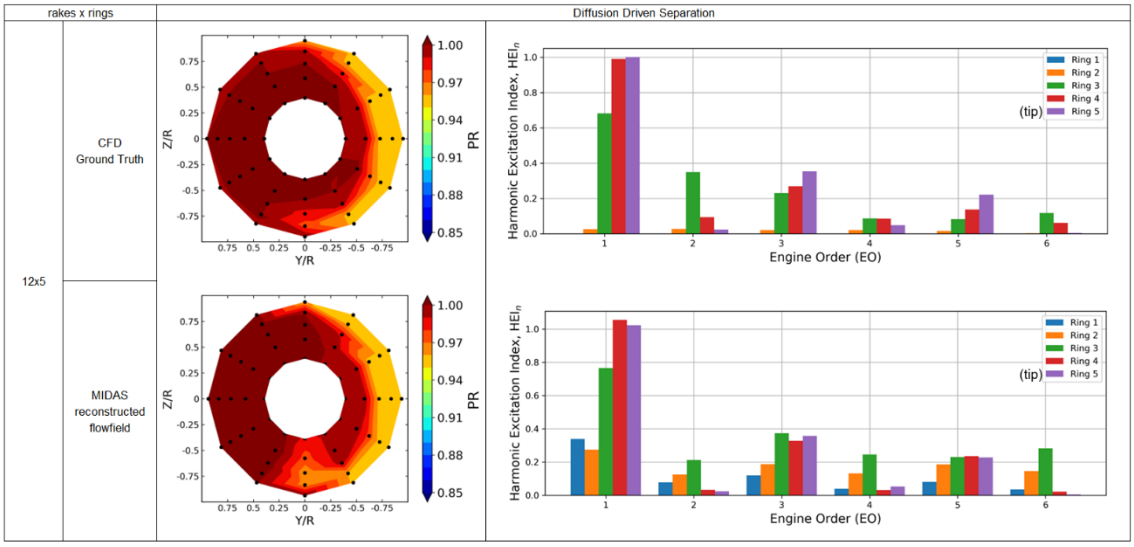


Figure 4-41 12x5 HEI analysis CFD ground truth vs reconstructed field.

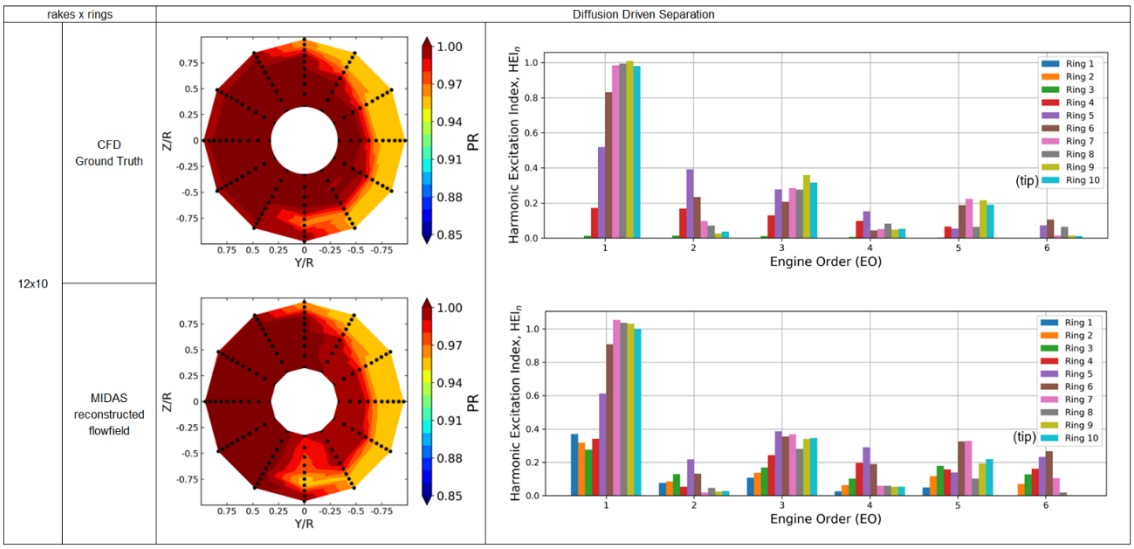


Figure 4-42 12x10 HEI analysis CFD ground truth vs reconstructed field.

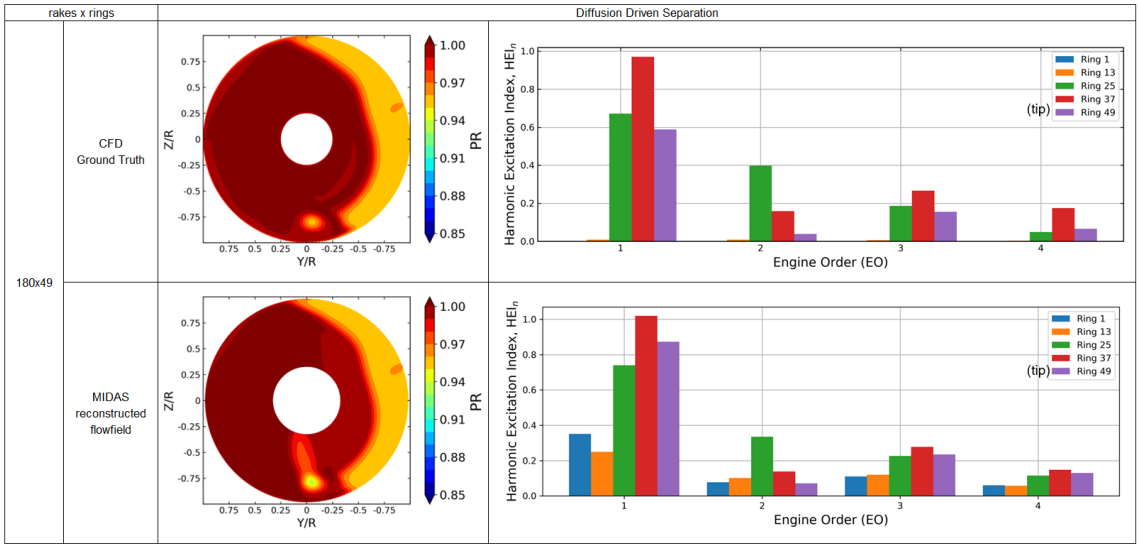


Figure 4-43 180x49 HEI analysis CFD ground truth vs reconstructed field.

4.9.2.2 Attached Flow

An analysis of the harmonic content for this flow condition, as shown in the following pictures, reveals that the dominant Engine Order is the first harmonic. While the reconstruction methodology successfully captures this primary harmonic, it unpredictably overestimates the magnitude of the HEI. Furthermore, the reconstructed field introduces non-physical HEI values within the inner radial rings. Since these elevated levels are absent in the high-resolution CFD baseline, they can be attributed to numerical noise or reconstruction artifacts. It is also noteworthy how spatial resolution impacts the capture of the ground vortex. The under-sampled low-resolution grid entirely fails to resolve the vortex, yielding an HEI of zero in the inner rings. Conversely, the high-resolution CFD accurately captures the vortex signature in this region, albeit at a substantially lower HEI magnitude than the artificially inflated values produced by the reconstruction.

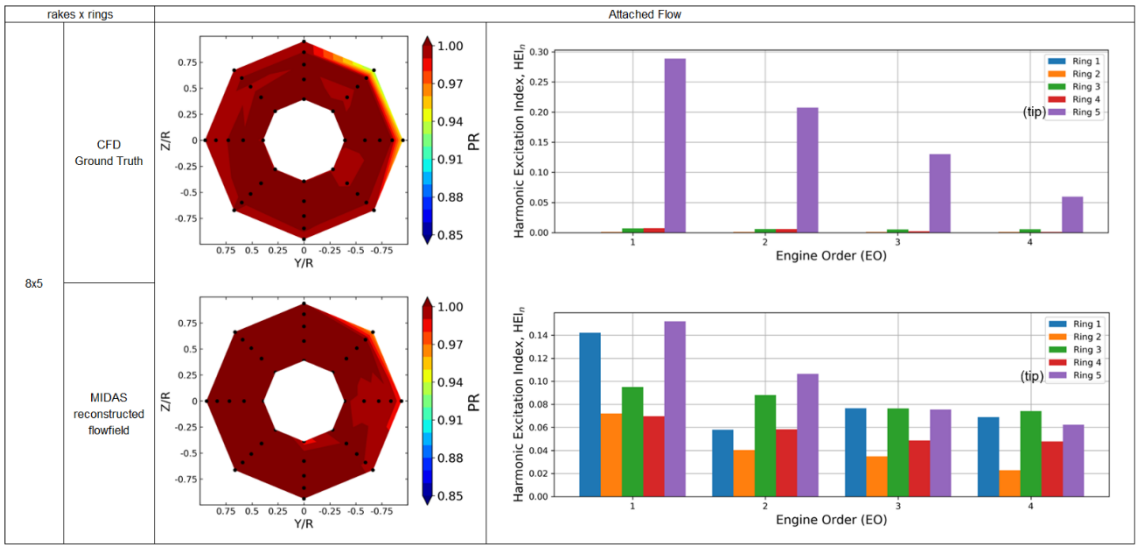


Figure 4-44 8x5 HEI analysis CFD ground truth vs reconstructed field.

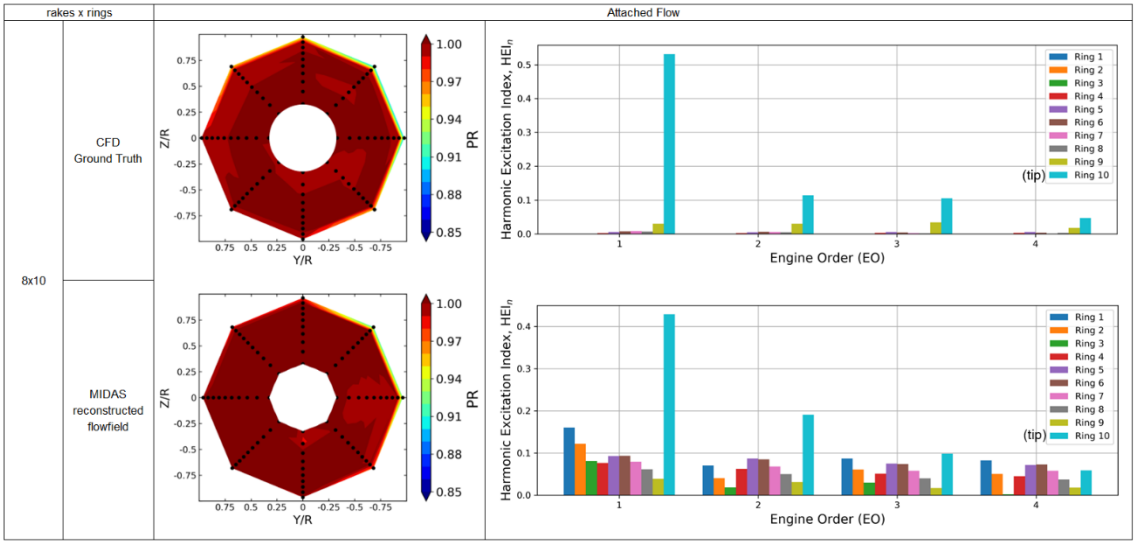


Figure 4-45 8x10 HEI analysis CFD ground truth vs reconstructed field.

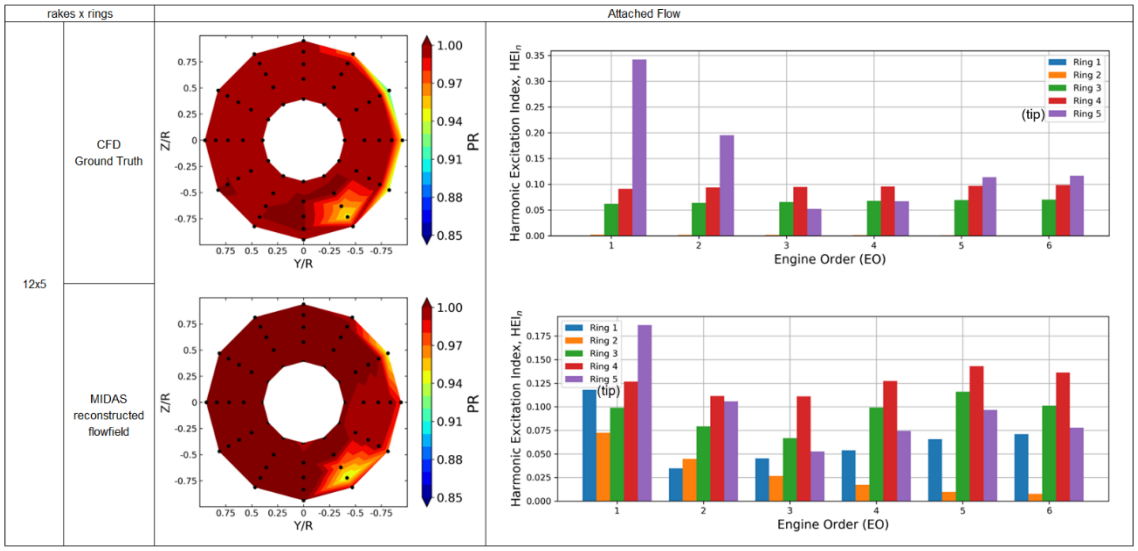


Figure 4-46 12x10 HEI analysis CFD ground truth vs reconstructed field.

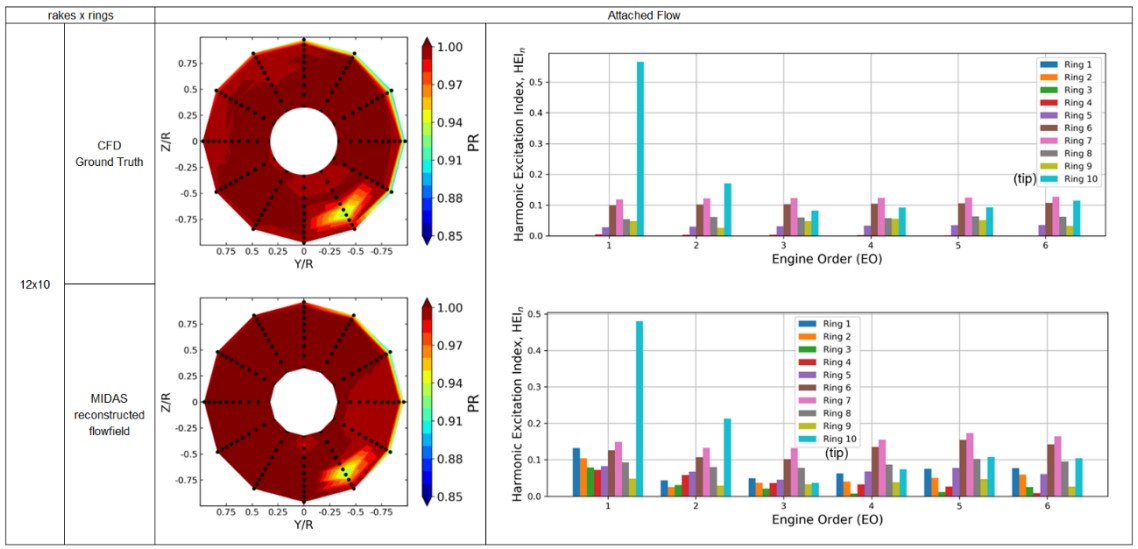


Figure 4-47 12x10 HEI analysis CFD ground truth vs reconstructed field.

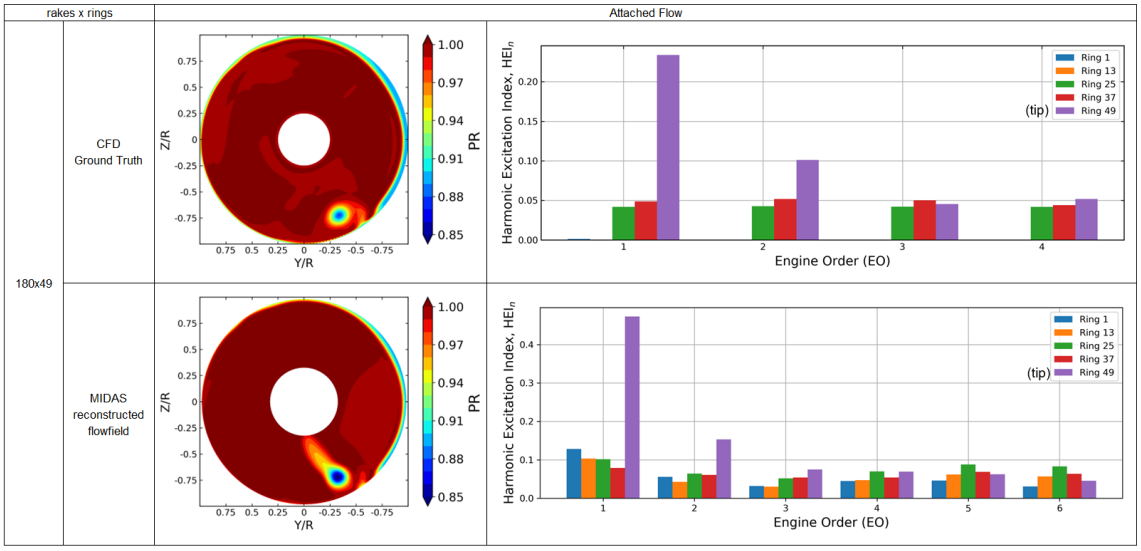


Figure 4-48 180x49 HEI analysis CFD ground truth vs reconstructed field.

4.9.2.3 Shock Driven Separation

In the shock-driven separation case, the reconstructed HEI field demonstrates strong overall consistency with the high-resolution CFD ground truth, successfully capturing the primary separation region. However, a significant limitation of the methodology is the introduction of substantial spurious numerical artifacts. This numerical noise heavily contaminates the innermost radial rings, artificially inflating the local HEI values. Consequently, when the resolution allows to capture the aerodynamic signature of the ground vortex, this physical flow feature is largely obscured by the superimposed numerical noise, reducing the signal-to-noise ratio in the core region.

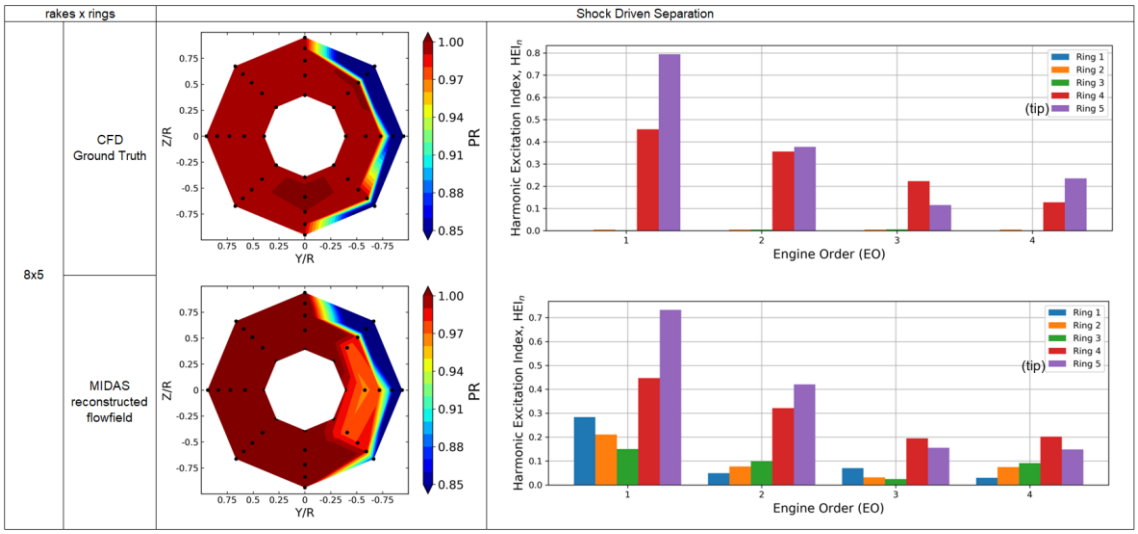


Figure 4-49 8x5 HEI analysis CFD ground truth vs reconstructed field.

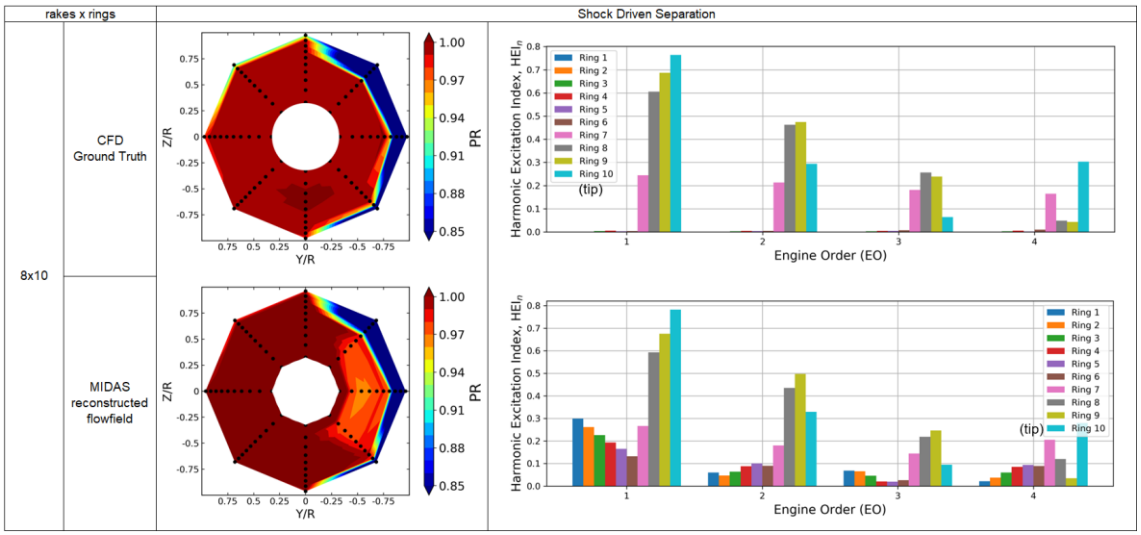


Figure 4-50 8x10 HEI analysis CFD ground truth vs reconstructed field.

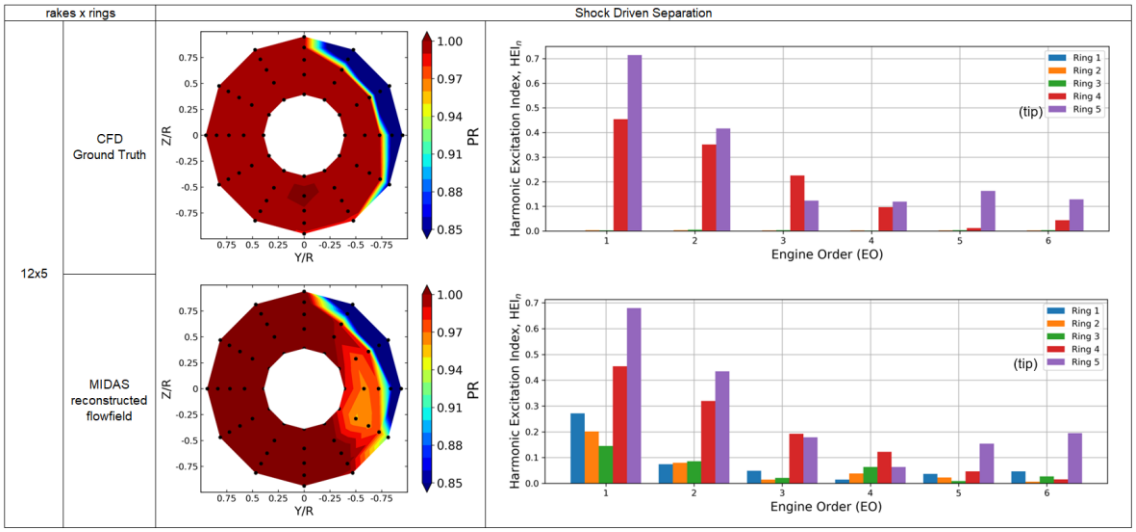


Figure 4-51 12x5 HEI analysis CFD ground truth vs reconstructed field.

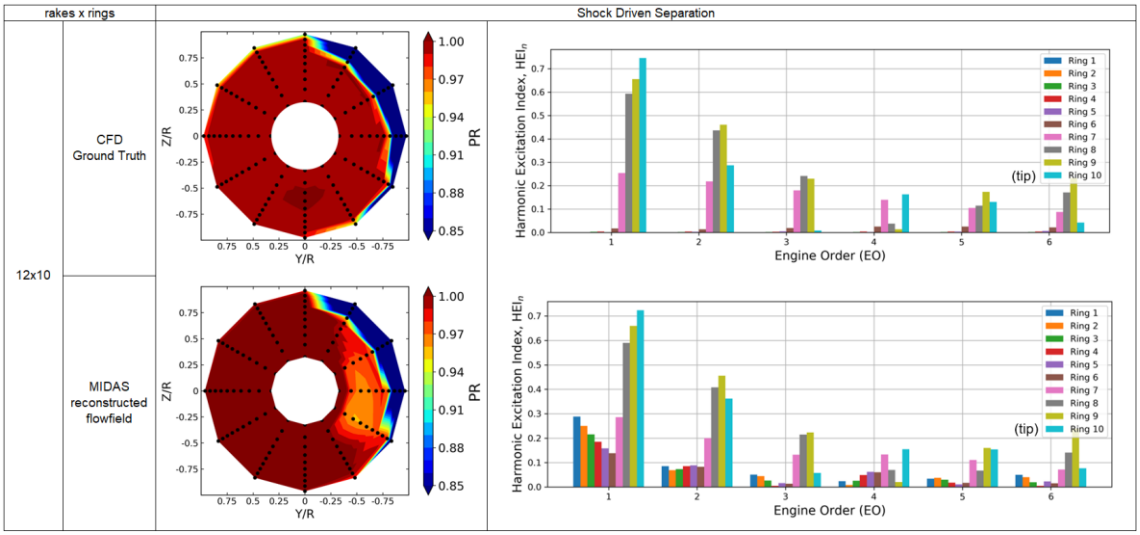


Figure 4-52 12x10 HEI analysis CFD ground truth vs reconstructed field.

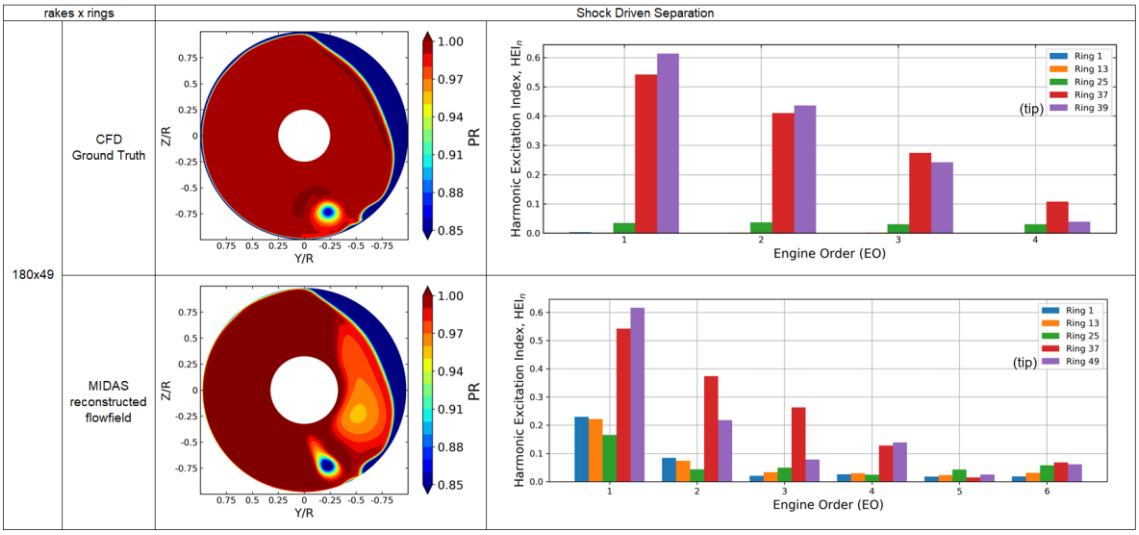


Figure 4-53 180x49 HEI analysis CFD ground truth vs reconstructed field.

4.9.3 Real Case Simulation: Notional Physical Rake vs Reconstruction Methods

In evaluating this scenario, it is essential to first establish that the simulated physical rakes represent an idealised baseline, as they inherently omit the aerodynamic blockage effects and measuring errors that would be present in a physical wind tunnel or test-bed environment. Consequently, the discrepancies observed between the methods stem entirely from spatial resolution and the mathematical nature of the reconstruction process.

4.9.3.1 Diffusion Driven Separation

An analysis of the contour plots in Figure 4-54 and Figure 4-55 reveals the limitations of standard physical arrays. The industrial standard *8x5* and *12x5* rakes suffer from significant spatial aliasing, completely failing to resolve compact, high-intensity aerodynamic structures. Specifically, the total pressure deficit at the bottom of the annulus, characteristic of an ingested ground vortex, is entirely missed by the physical rakes, resulting in a smoothed pressure field. This lack of spatial resolution translates into a dangerous underestimation of aeromechanical forcing. Looking at the HEI charts, the simulated physical rakes register almost completely flat responses for the inner rings (Ring 1 and Ring 2), entirely missing the fundamental forcing peaks at the lower Engine Orders. In contrast, the reconstructed flowfields successfully capture the presence of this critical distortion. However, the reconstructed data exhibits a significant amplification in the HEI for these inner rings when compared to the ground truth, as seen in the previous section. This overestimation is a compounded result of two inseparable factors. The genuine recovery of high-resolution distortion data and the numerical error introduced by the reconstruction algorithm itself. Because the Direct Spatial Integration method integrates radially inward, the mathematical smearing accumulates near the hub, making it impossible to decouple the true aerodynamic load from the numerical artefact in this region.

Despite the overestimation at the hub, the performance of the reconstruction method in the outer span of the compressor face is highly encouraging. The charts demonstrate that the three outermost rings (Rings 3, 4,

and 5) are remarkably reliable. In these regions, the HEI curves for the reconstructed fields align closely with the simulated rakes, proving that where the cumulative integration error is minimal, the reconstructed velocimetry data provides a highly accurate assessment of fan blade forcing.

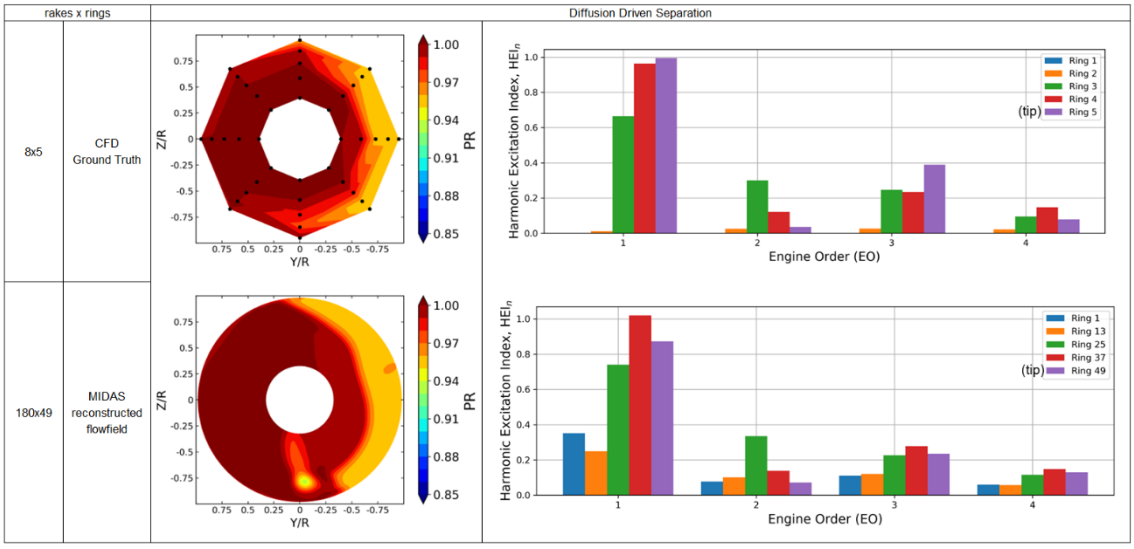


Figure 4-54 Real Case simulation: Reconstruction vs 8x5 rake - Diffusion Driven Separation.

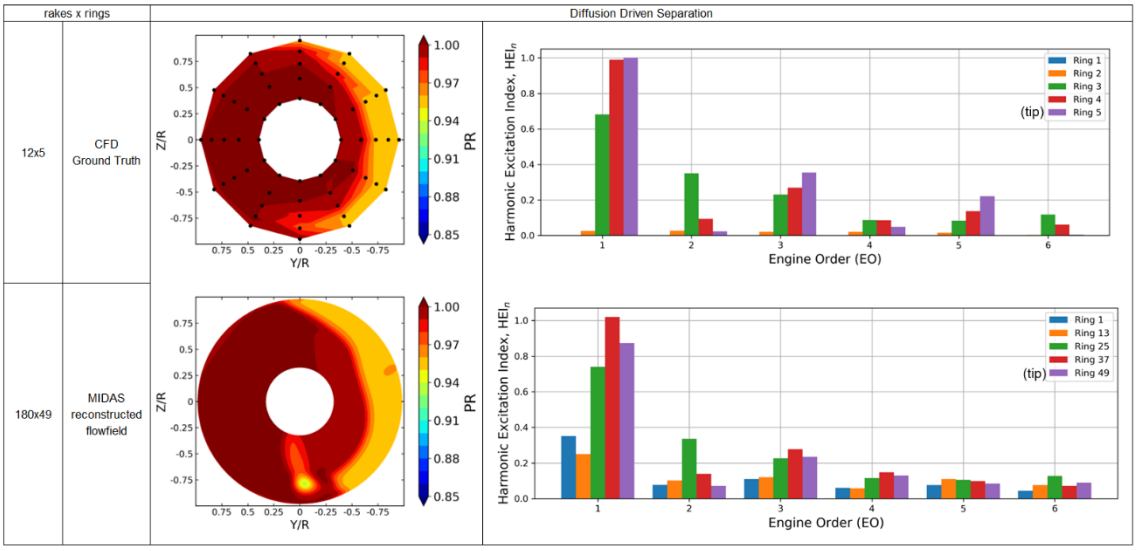


Figure 4-55 Real Case simulation: Reconstruction vs 12x5 rake - Diffusion Driven Separation.

4.9.3.2 Attached Flow

Transitioning to the attached flow scenario presents a nuanced contrast to the previously analysed separated regime. Interestingly, the simulated high-density *12x5* physical rake in Figure 4-57 performs quite well in this case, capturing the primary aerodynamic structures with reasonable fidelity. However, the critical takeaway remains the inadequacy of the industry-standard *8x5* configuration in Figure 4-56. Even in this relatively stable attached flow, the sparse *8x5* array fails to resolve the finer details, effectively losing all the useful aeromechanical information required for a safe and comprehensive fan blade assessment. Looking closely at the outer span, there is a pronounced spike in the HEI on the 5^{th}, outermost ring. This sharp increase is directly attributable to a very thin, low-momentum area situated at the extreme outer border of the annulus. This highlights how highly localised boundary layer deficits or casing interactions can dominate the forcing spectrum at the blade tips, a feature that must be accurately resolved.

Regarding the reconstructed flowfield, the DSI method yields a highly consistent pressure map overall, especially focused on the outer rings. However, the mathematical limitations of the radial integration are once again apparent. There is a distinct "error trail" that propagates inward, which is particularly noticeable in the wake of the ground vortex structure. Just as in the diffusion-driven scenario, this mathematical smearing compromises the accuracy of the forcing assessment at the lower rings, as the algorithmic artefact accumulates and cannot be decoupled from the physical aerodynamic load near the hub.

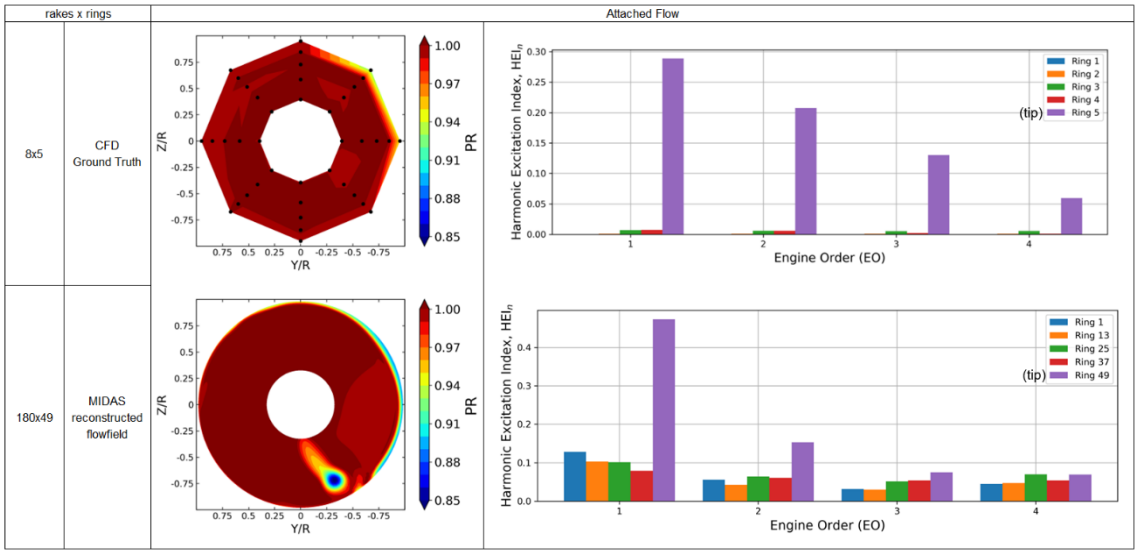


Figure 4-56 Real Case simulation: Reconstruction vs 8x5 rake - Attached Flow.

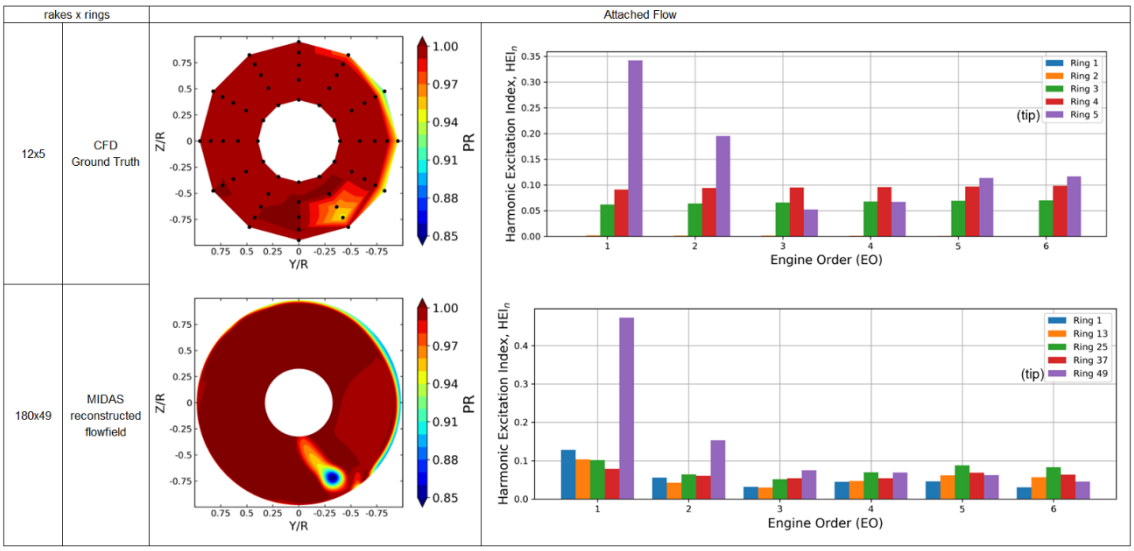


Figure 4-57 Real Case simulation: Reconstruction vs 12x5 rake - Attached Flow.

4.9.3.3 Shock Driven Separation

Consistent with the trends observed in the previous regimes, in the shock driven separation both the standard *8x5* in Figure 4-58 and the higher density *12x5* (Figure 4-59) configurations completely fail to resolve the critical ground vortex structure. The contour plots demonstrate a severe case of spatial aliasing. The distortion at the bottom of the annulus is entirely smoothed over, rendering the physical rakes blind to a primary driver of aerodynamic instability in this highly separated flow.

The reconstructed flowfield successfully detects the presence of this localised distortion, but it introduces a notably wider band of numerical error compared to the diffusion-driven and attached flow cases. This artefact is substantial enough that the resulting error trail noticeably inflates the HEI as far out as the fourth ring, a broader reach than seen in earlier scenarios.

The reconstructed HEI values in the inner rings are significantly enlarged, reading about 1.5 when the actual baseline forcing should only be around 0.05 on the third ring as established in Figure 4-53. This overestimation highlights a critical trade-off. The physical rakes register almost zero forcing in these inner regions, entirely missing the aerodynamic threat. Therefore, despite the substantial numerical amplification caused by the integration trail, the reconstruction method remains the more conservative and safer approach. It flags the presence of severe distortion that would otherwise go completely undetected by standard industrial instrumentation.

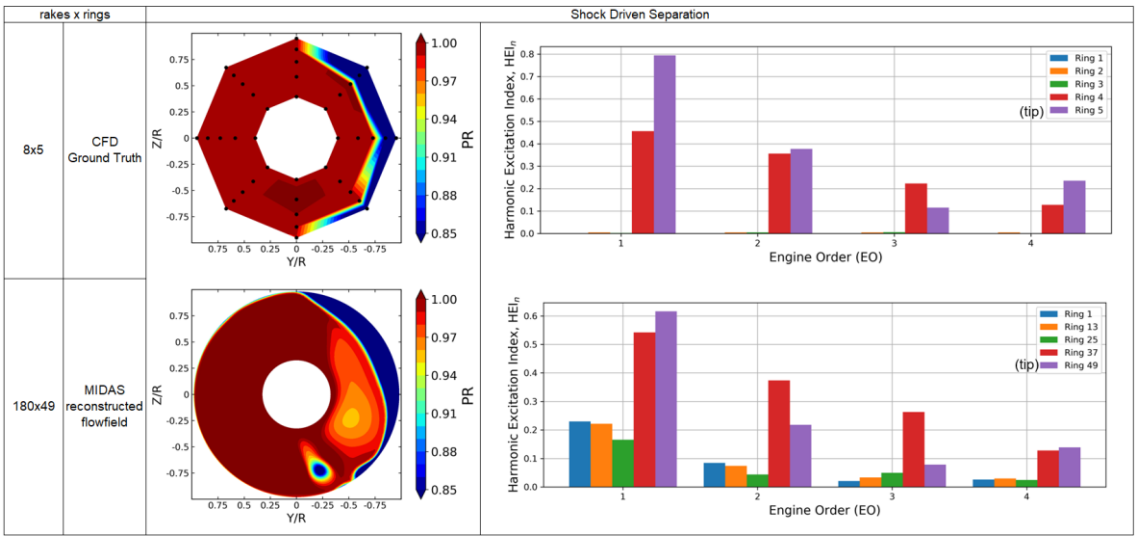


Figure 4-58 Real Case simulation: Reconstruction vs 8x5 rake - Shock Driven Separation.

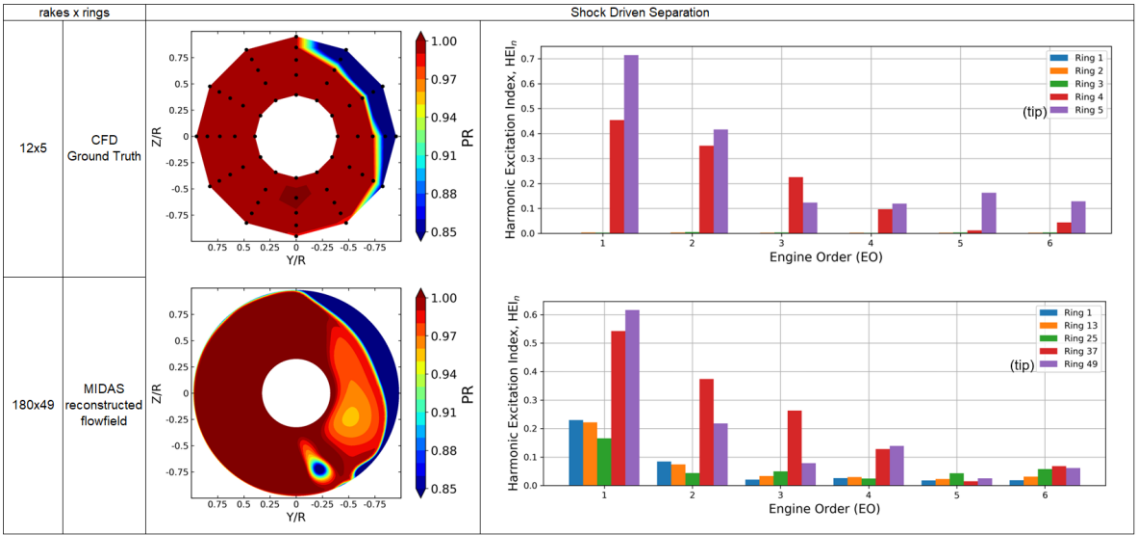


Figure 4-59 Real Case simulation: Reconstruction vs 12x5 rake - Shock Driven Separation.

4.10 Conclusions Regarding the CFD Dataset

The comprehensive evaluation of the computational dataset establishes that traditional intrusive instrumentation, specifically sparse arrays like the standard *8x5* physical rake configuration, suffers from severe spatial aliasing. Across varying operational regimes, these low-density grids consistently fail to resolve highly compact, localised aerodynamic structures, most notably the ingested ground vortex. Consequently, relying solely on discrete probes inherently masks the true spatial complexity of flow non-uniformities, leading to a dangerous underestimation of peak distortion intensities and overall structural forcing. The accuracy of the distortion assessment is predominantly governed by the circumferential density of the measurement array, whereas radial density plays a secondary role, provided a minimum threshold is maintained to adequately capture near-wall boundary layer gradients.

The pressure-from-velocity reconstruction technique successfully eliminates the spatial blind spots of conventional physical arrays, reliably resolving the aerodynamic structures that sparse grids routinely miss. However, the Direct Spatial Integration scheme introduces a persistent and measurable mathematical offset into the final flowfield topology. Because the algorithm integrates pressure gradients radially inward from the outer casing, it artificially

drags severe boundary pressure deficits toward the hub. This creates non-physical low-pressure wakes that systematically inflate the calculated $DC60$ metric. This mathematical overestimation scales with the Mass Flow Capture Ratio, presenting an absolute error delta of approximately 0.07 during diffusion-driven separation, 0.09 in attached flow, and 0.11 during extreme shock-driven separation. It is crucial to contextualise this error within engine certification processes, which strictly mandate a maximum acceptable $DC60$ limit, usually 0.2. In baseline attached flow conditions, the true aerodynamic $DC60$ is inherently low, therefore, the absolute offset of 0.09 translates into a disproportionately high relative error. This artificial inflation of distortion metrics in clean flow regimes poses a significant risk of falsely exceeding rigid certification thresholds. However, the behaviour of the reconstructed field remains stable across varying virtual grid densities, confirming its reliability as a systematic, calibratable numerical offset rather than an unpredictable error.

Investigations into the reconstruction algorithm indicate that altering the placement of outer boundary condition probes does not significantly mitigate the inherent numerical error of the radial integration scheme. Whether distributing the virtual probes evenly around the casing or concentrating them unevenly to target high-gradient regions like the ground vortex, the improvements in the boundary inputs are ultimately overshadowed by the dominant footprint of the inward integration error. Nevertheless, the data demonstrates that a low quantity of evenly spaced boundary probes is entirely sufficient to yield stable diagnostic metrics that comfortably meet standard industrial compliance thresholds, proving that extreme physical boundary density is not a strict prerequisite for reliable validation.

From a structural aeromechanical perspective, the velocimetry reconstruction method proves superior to standard discrete arrays for diagnosing blade forcing. While an *8x5* physical rake captures the broad, low-order harmonic excitations typical of diffusion-driven separations, it is entirely blind to the localised forcing generated by a compact ground vortex, erroneously registering a harmonic excitation of near-zero. The non-intrusive reconstruction effectively

flags these small-scale distortion threats. Although the inward mathematical smearing heavily inflates the Harmonic Excitation Index on the inner radial rings near the spinner, the reconstructed flowfield provides a conservative assessment of fan blade forcing in the critical radial span. This methodology is not optimally suited for validating baseline attached flow conditions. Instead, its true diagnostic value is unlocked in severe off-design regimes. Ultimately, this establishes the mathematical reconstruction as a highly targeted and safer diagnostic tool for evaluating complex off-design aerodynamic phenomena without incurring in the aerodynamic blockage penalties of physical wind-tunnel instrumentation.

5 PARTICLE IMAGE VELOCIMETRY DATASET ANALYSIS

5.1 Time-Averaged PIV Dataset and Flow Conditions

Building upon the knowledge and methodological framework acquired from the analysis of the computed dataset, the investigation now transitions to the evaluation of the experimental Particle Image Velocimetry dataset. The spatial integration and pressure reconstruction techniques previously validated on the numerical results are here applied to physical optical measurements to assess their performance, robustness, and accuracy in a practical testing environment.

The experimental campaign captured the internal flow field under three distinct operative conditions. While these conditions feature slightly different specific values compared to the numerical cases analysed in previous chapters, they effectively represent the same fundamental aerodynamic phenomena. The first operative condition operates at a MFCR of 7.83, resulting in a flow field predominantly characterised by diffusion-driven separation. The second condition represents a stable, attached flow regime, achieved at an MFCR of 14.71. Finally, the third condition is characterised by an elevated MFCR of 17.81, which induces a severe shock-driven separation within the intake.

Following the initial characterisation of the flow regimes, the total pressure field was reconstructed from the available PIV velocity vectors. To evaluate the sensitivity of the distortion metrics to spatial resolution, the reconstructed full resolution *180x49* fields were subsequently undersampled to simulate various rake array configurations. However, based on the findings from the computational dataset analysis, the 40-ring and 49-ring rake configurations were excluded from this phase. Previous results demonstrated that these high-density configurations yielded negligible differences in the final distortion metrics. Therefore, omitting them from the experimental analysis conserved computational resources and processing time without compromising the validity of the study.

To validate the reconstruction methodology, the undersampled PIV results were compared directly against physical probe measurements. The experimental reference data was obtained using a physical rake setup comprising 8 rakes and 10 rings. To facilitate a smoother visual comparison and a higher-resolution metric evaluation, this *8x10* physical measurement was linearly interpolated to a *24x10* grid. Furthermore, the physical experiments used traditional Pitot probes, which inherently record time-averaged total pressures, the instantaneous PIV reconstructions has been processed accordingly to ensure an equivalent comparison. The PIV results presented in this analysis are derived from the time-average of 1000 discrete instantaneous pressure fields snapshots, ensuring a consistent comparison between the optically reconstructed pressure fields and the pneumatic probe data.

5.2 PIV Reconstructed Pressure Field

5.2.1 Diffusion Driven Separation

As expected from the previous experience, the behaviour of the Distortion Coefficient $DC60$ is monotonic, increasing as the azimuthal resolution increases before approaching a stable asymptote. As illustrated in Figure 5-2, this asymptotic behaviour becomes prominent beyond 24 rakes, stabilising at a $DC60$ value of approximately 0.580. Furthermore, the data indicates that radial resolution has virtually zero influence on the calculated $DC60$ within this regime. The plotted curves for 5, 10, 20 and 30 rings are almost entirely superimposed across all circumferential resolutions, confirming that the rake number is the primary driver of reconstruction accuracy for this metric. The contours in Figure 5-1 show that the ground vortex is captured, although poorly defined and captured by chance thanks to a lucky positioning of the 12-rakes configuration.

When comparing these reconstructed results to conventional intrusive measurement techniques, distinct discrepancies emerge. The standard 80-probes array calculates a $DC60$ of 0.600 as shown in Figure 5-3. This indicates that the physical rake measures a $DC60$ that is 0.019 higher than the asymptotic value achieved by the high-resolution PIV reconstruction or 2.3% higher. However, as established in prior sections, the reconstruction method itself inherently overestimates the $DC60$, in this specific diffusion-driven case, by approximately 0.07. Consequently, the true aerodynamic $DC60$ is theoretically lower still, meaning the physical rake is significantly amplifying the distortion severity, overestimating the true $DC60$ by roughly 0.089 overall.

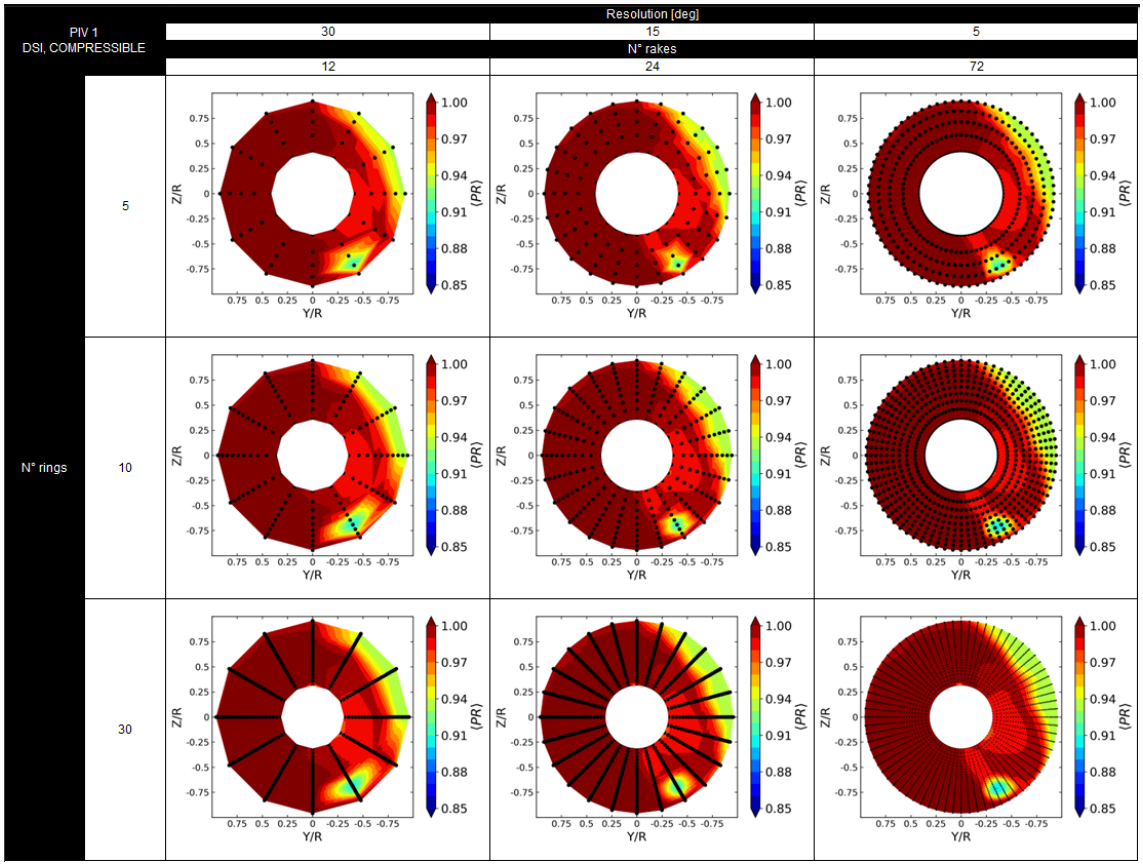


Figure 5-1 Total pressure reconstructed flowfield at different resolutions - Diffusion Driven Separation.

Table 5-1 DC60 comparison reconstruction vs. rakes – Diffusion Driven Separation.

PIV 1 DSI, COMPRESSIBLE DC60		Resolution [deg]				
		30	15	10	5	2
		N° rakes				
		12	24	36	72	180
N° rings	5	0.486	0.563	0.573	0.579	0.582
	10	0.483	0.562	0.574	0.580	0.582
	10 rake		0.600			
	20	0.480	0.562	0.573	0.579	0.581
	30	0.481	0.561	0.573	0.579	0.581

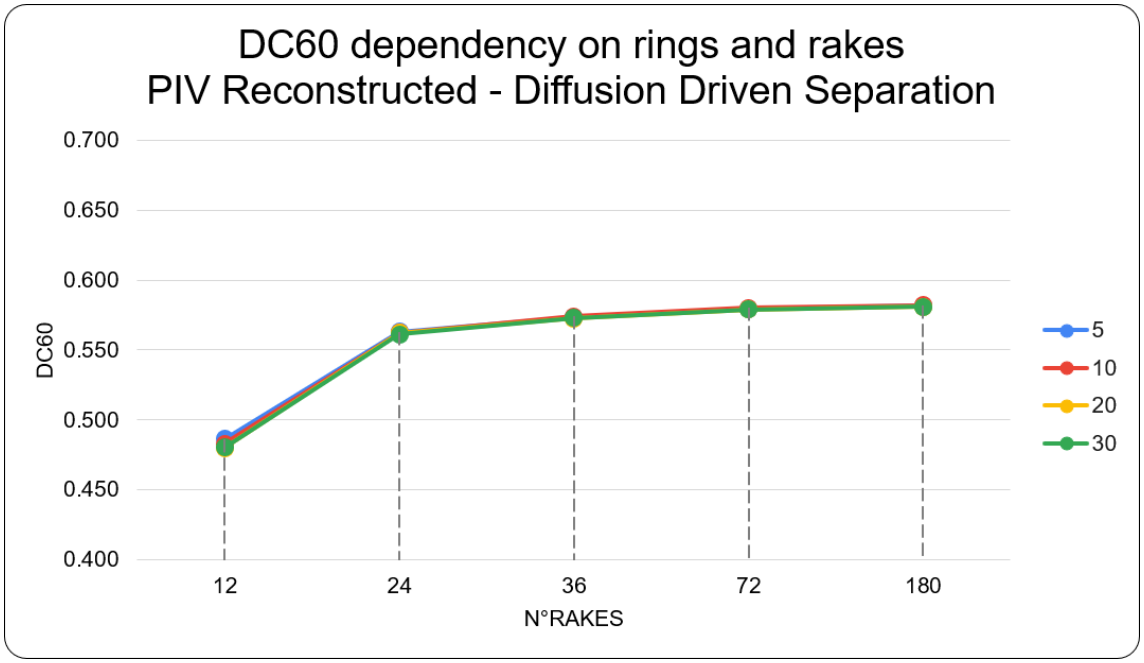


Figure 5-2 Reconstructed flowfield DC60 – Diffusion Driven Separation.

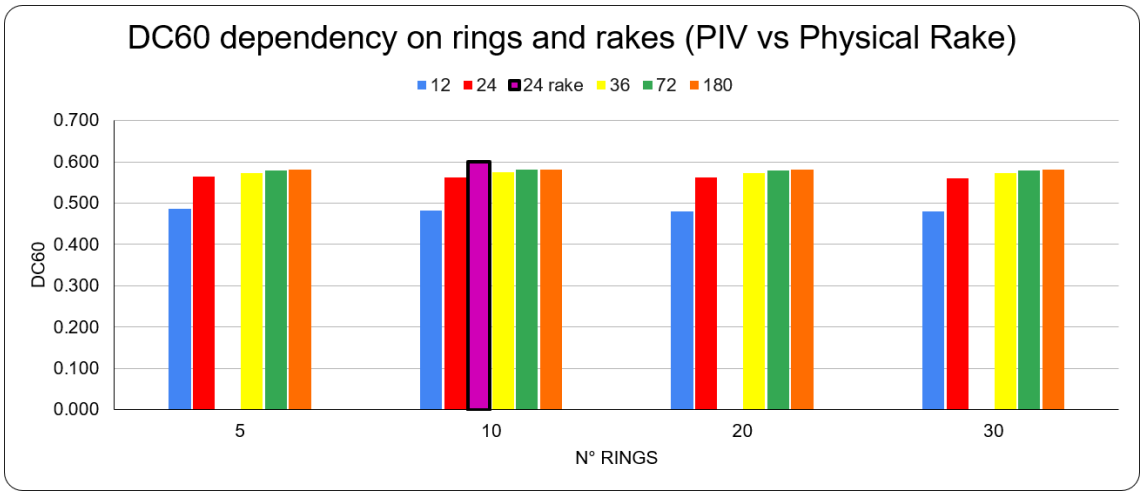


Figure 5-3 DC60 comparison reconstruction vs. rakes – Diffusion Driven Separation.

5.2.2 Attached Flow

A visual assessment of the reconstructed total pressure field for the attached flow condition in Figure 5-4 highlights the critical role of azimuthal resolution in capturing highly localised flow features. The contour plots illustrate a ground vortex near the bottom of the engine face. At the lowest resolution of 30° (12 rakes), the spatial sampling is too coarse, failing to capture the true

intensity and footprint of the vortex. However, as the resolution improves, the vortex resolves into a sharply defined distortion cloud. Conversely, moving vertically through the contour matrix demonstrates that for more than 5 rings, increasing the radial resolution up to 30 rings has virtually no visible impact on resolving the flow. This visual sensitivity is quantified in the $DC60$ dependency analysis in Figure 5-5. The line graph plotting $DC60$ against the number of rakes exhibits a steep initial gradient. With the 12-rake configuration, the $DC60$ is underestimated at approximately 0.090. As rake resolution increases, the calculated distortion rises approaching a stable asymptote of 0.165 at 180 rakes.

Evaluating the practical implications of this spatial sensitivity requires comparing the PIV reconstruction against standard intrusive measurement methods. As illustrated in the bar chart comparing the PIV versus physical rake data, the standard physical array (interpolated to 10 rings and 24 rakes) calculates a $DC60$ of 0.066. The delta that holds the most practical significance for real-world applications is the difference between this standard physical measurement and the full resolution reconstruction. In this attached flow scenario, the fully resolved reconstructed flowfield yields a $DC60$ that is 0.099 higher than the physical rake's measurement. This substantial difference is directly attributable to spatial undersampling; the low-resolution physical rake fails to adequately intercept and capture the concentrated pressure drop of the ground vortex, ultimately resulting in a significant underestimation of the true aerodynamic distortion. However, in the computed dataset, the attached flow condition has shown a consistent overestimate of the metric of approximately 0.9, which would dramatically change the outcome of this study, as the metric value would be dramatically closer to the physical rake. For this reason, it was concluded that for this design point flow condition, the reconstruction method is sometimes deceiving and not ideal.

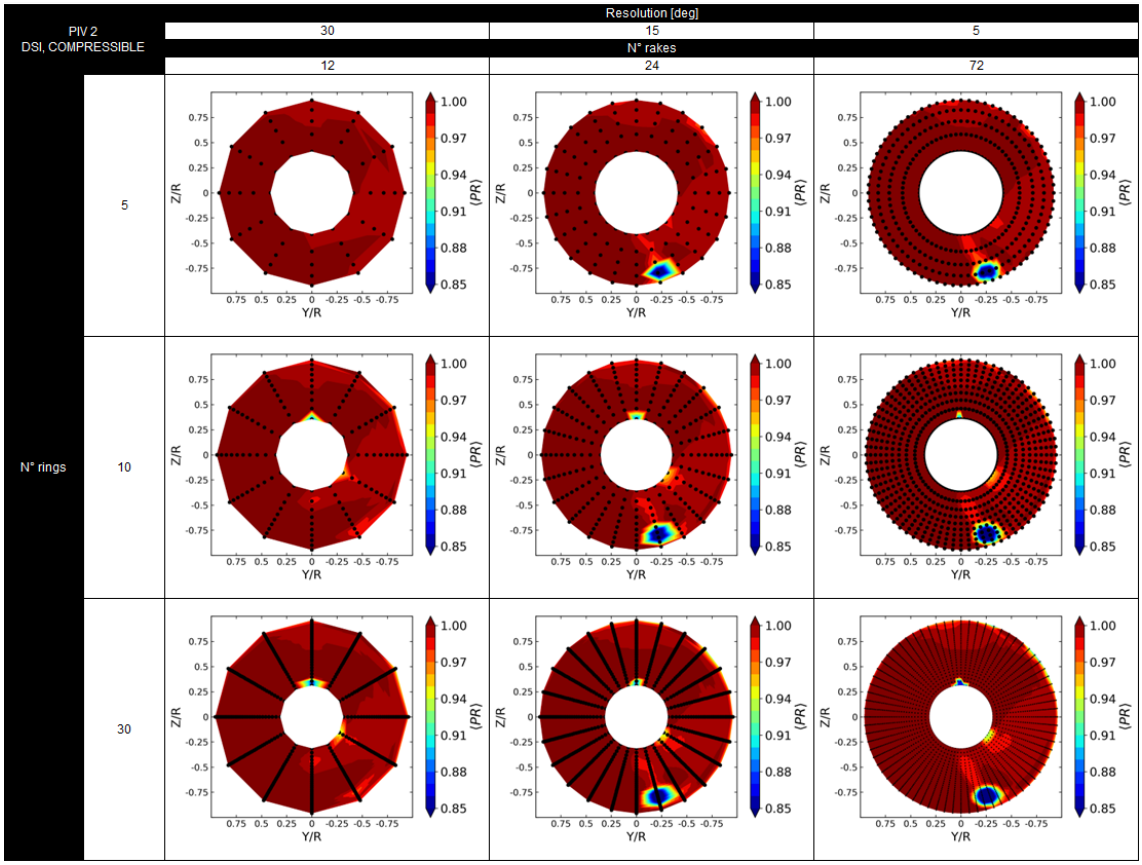


Figure 5-4 Total pressure reconstructed flowfield at different resolutions – Attached Flow.

Table 5-2 DC60 comparison reconstruction vs. rakes – Attached Flow.

PIV 2 DSI, COMPRESSIBLE DC60		Resolution [deg]				
		30	15	10	5	2
		N° rakes				
		12	24	36	72	180
N° rings	5	0.078	0.136	0.142	0.147	0.149
	10	0.094	0.155	0.160	0.167	0.169
	10 rake		0.066			
	20	0.093	0.153	0.156	0.163	0.166
	30	0.092	0.152	0.156	0.163	0.165

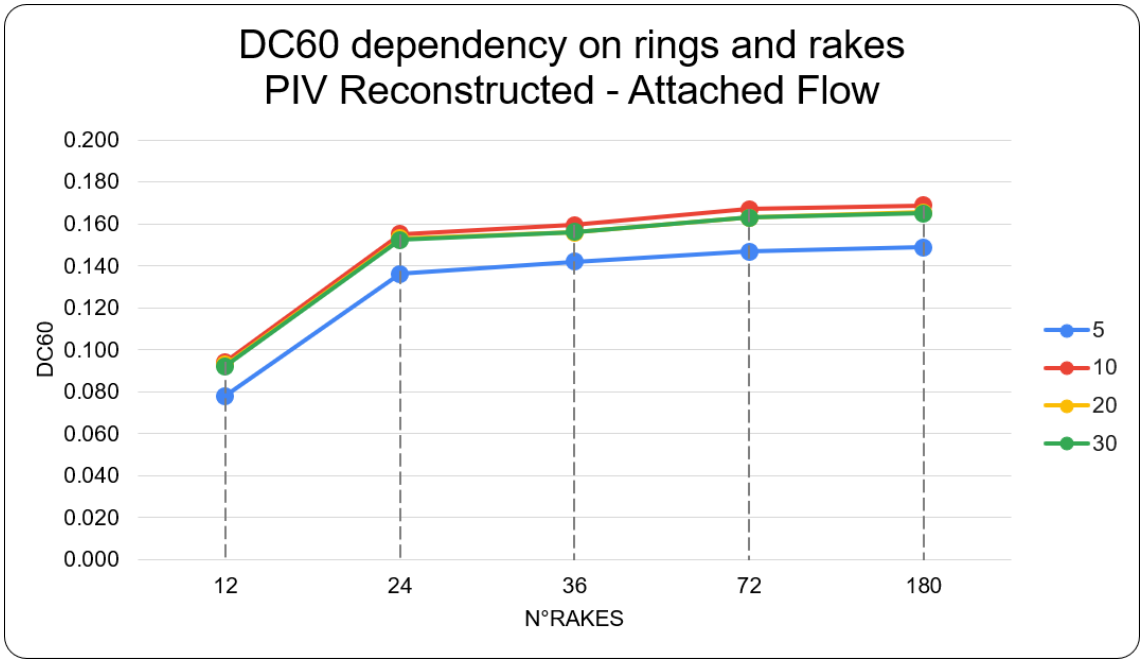


Figure 5-5 Reconstructed flowfield DC60 – Attached Flow.

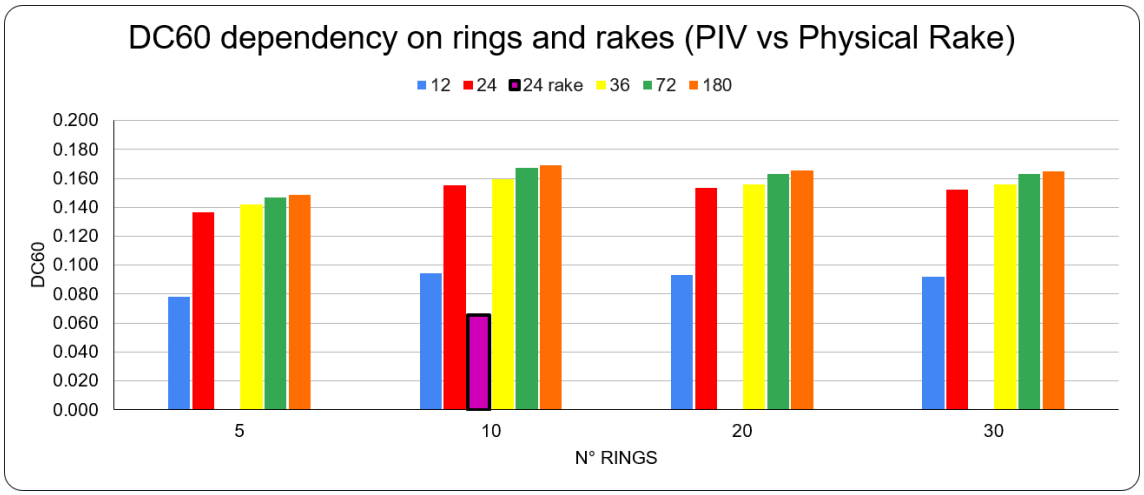


Figure 5-6 DC60 comparison reconstruction vs. rakes – Attached Flow.

5.2.3 Shock Driven Separation

To conclude, the shock-driven separation reconstruction reveals a flow topology characterised by two distinct distortion features. The contour plots clearly display a large, dominant area of low pressure recovery situated on the right side of the engine face, indicative of the primary shock-induced separation. In addition, a smaller low-pressure region is visible, corresponding to the ground vortex. At a coarse 30° azimuthal resolution the ground vortex is totally

undetected as visible in Figure 5-7. As the resolution tightens, the vortex footprint becomes sharply concentrated. Conversely, moving vertically through the contour matrix confirms that altering the radial resolution produces negligible alteration to the $DC60$ metric (Figure 5-8). The quantitative analysis of the $DC60$ dependency reinforces these visual observations. The line graph tracking $DC60$ against the number of rakes demonstrates a monotonic increase approaching an asymptote. At the lowest resolution of 12 rakes, the $DC60$ is calculated at approximately 0.280. As circumferential resolution improves, the metric rises, stabilising at 0.310.

To evaluate the practical implications of this reconstruction method, it is most logical to compute the delta between the full resolution reconstruction and the standard physical rake measurement, as these represent the bounds of real-world application. According to the comparative bar chart in Figure 5-9, the standard physical array calculates a $DC60$ of 0.245. The fully resolved reconstructed flowfield yields a $DC60$ of 0.310, making the reconstructed distortion measurement 0.065 higher than the intrusive rake measurement. While this underestimation by the physical rake is notable, it is less impactful than the delta observed in the pure attached flow case. Because the massive, primary shock-driven separation dominates the overall pressure loss and is captured by both methods, the relative error is subdued. However, the physical array lacks the necessary density to intercept the ground vortex, resulting in a less reliable overall $DC60$ calculation.

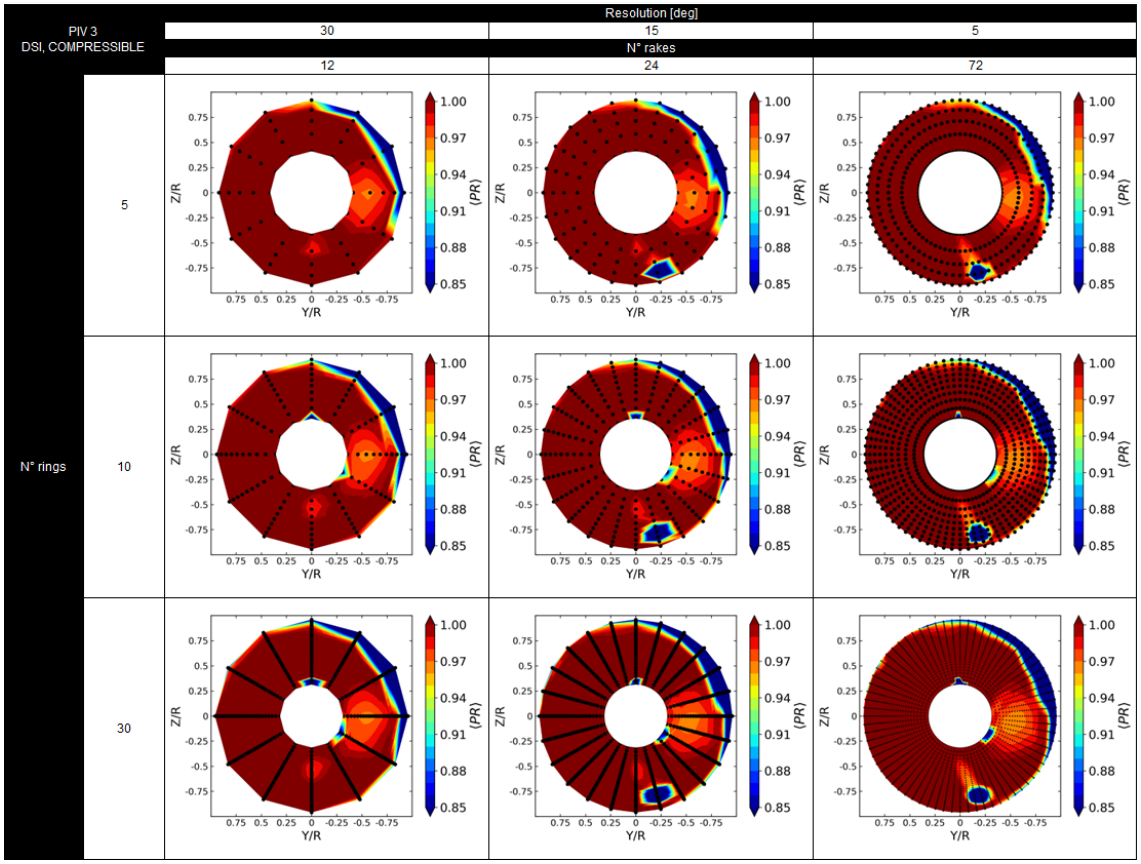


Figure 5-7 Total pressure reconstructed flowfield at different resolutions – Shock Driven Separation.

Table 5-3 DC60 comparison reconstruction vs. rakes – Shock Driven Separation.

PIV 3 DSI, COMPRESSIBLE DC60		Resolution [deg]				
		30	15	10	5	2
		N° rakes				
		12	24	36	72	180
N° rings	5	0.292	0.310	0.318	0.321	0.323
	10	0.276	0.298	0.309	0.312	0.312
	10 rake		0.245			
	20	0.275	0.296	0.305	0.309	0.310
	30	0.276	0.296	0.305	0.309	0.310

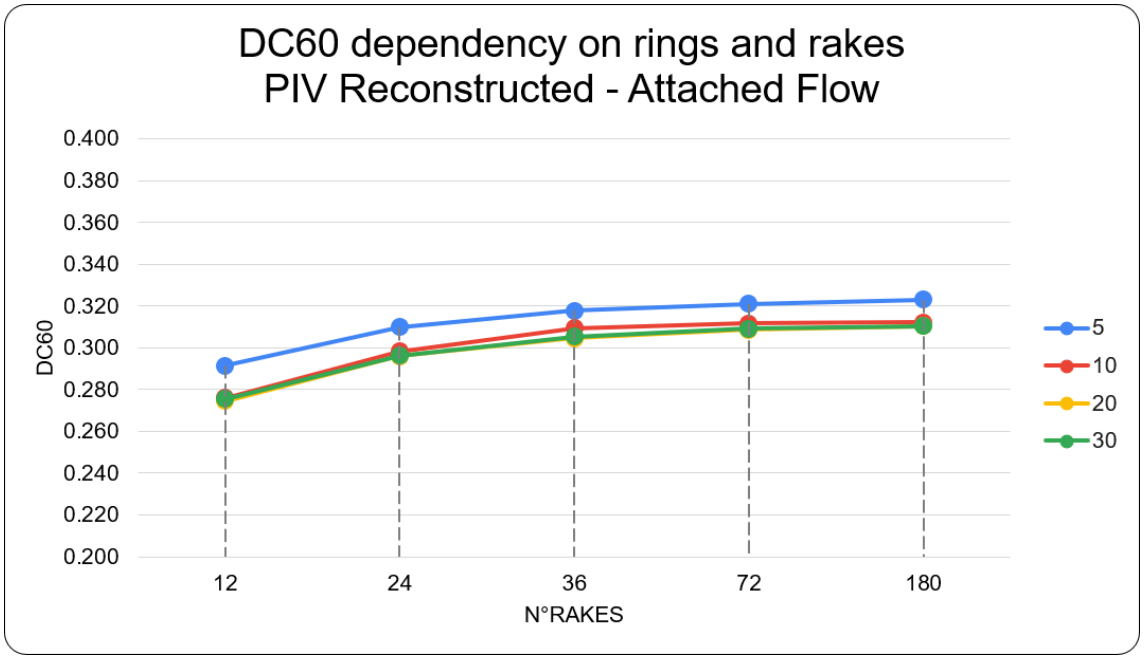


Figure 5-8 Reconstructed flowfield DC60 – Shock Driven Separation.

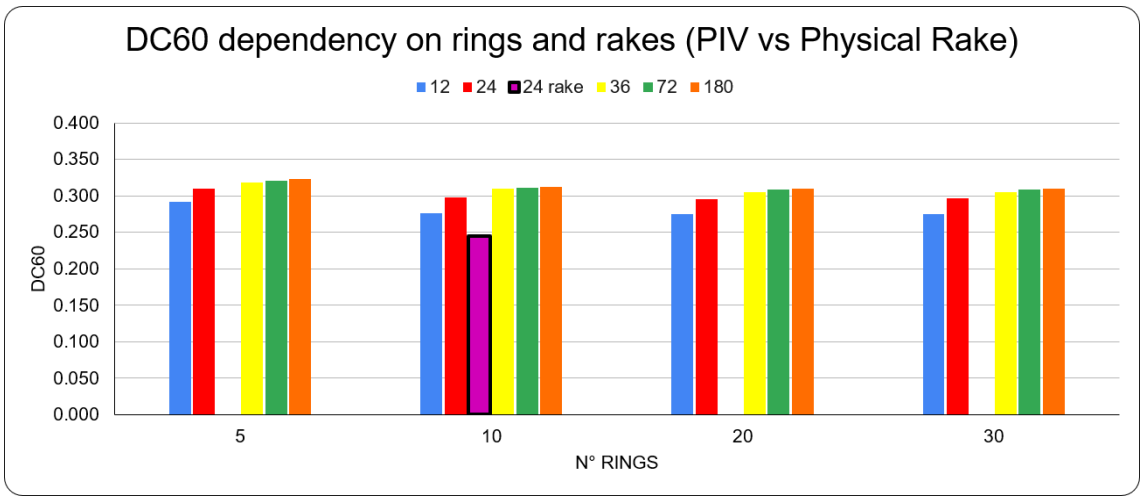


Figure 5-9 DC60 comparison reconstruction vs. rakes – Shock Driven Separation.

5.3 Influence of Boundary Conditions

This section evaluates the sensitivity of PIV pressure reconstruction to the spatial resolution of the applied boundary conditions. Specifically, the full 16 probes boundary condition distribution is compared against a configuration using 12 unevenly distributed probes. The comparative analysis spans the three distinct aerodynamic regimes: diffusion-driven separation, attached flow and shock-driven separation.

An examination of the total pressure recovery contour maps in Figure 5-10 reveals that the macroscopic topological features of the flow field remain highly consistent irrespective of the boundary condition resolution. The reduction in spatial data points does not induce any significant qualitative degradation in the reconstructed flow structures. In the diffusion-driven separation regime, the characteristic deep, expansive low-pressure region is captured with high fidelity. Similarly, the localised low-pressure pockets indicative of the attached flow and shock-driven separation cases are mapped accurately by the discrete probe configuration.

To quantify the impact of the boundary condition reduction, a comparative analysis of the $DC60$ metric was conducted in Figure 5-11 to assess steady-state aerodynamic face distortion. The numerical data demonstrates that the 12-probe configuration systematically underpredicts the $DC60$ severity across all evaluated flow regimes. The maximum absolute deviation is observed in the highly distorted diffusion-driven separation case, which exhibits a discrepancy of 0.048 compared to the full-resolution baseline. Conversely, the attached flow and shock-driven separation regimes display minor deviations of 0.021 and 0.019, respectively.

Despite this systematic underprediction, the discrete boundary condition approach successfully maintains the relative scaling and trend of distortion severity among the different flow states. The findings indicate that while an unevenly distributed 12-probe array introduces a minor quantitative offset in the calculated distortion metric, it provides an exceptionally reliable approximation of both the overall flow topology and the relative distortion magnitude. Consequently, this reduced-resolution approach represents a practical

methodology for PIV pressure reconstruction in aero-engine intake testing, offering a viable alternative in scenarios where positioning too many boundary data could introduce errors and difficulties.

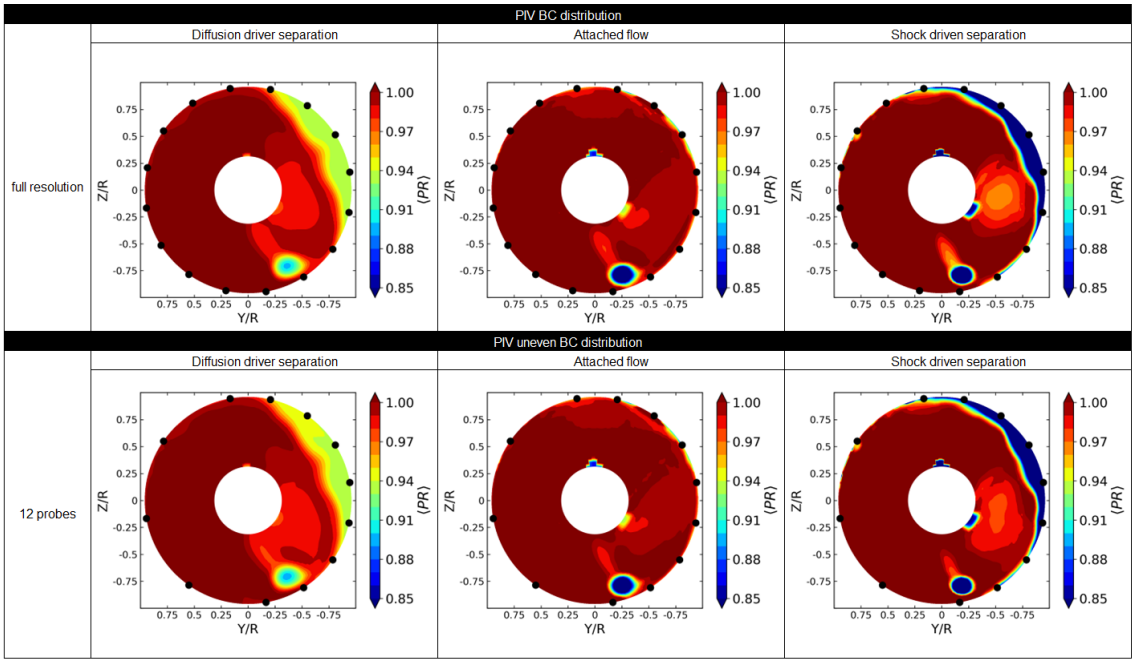


Figure 5-10 Comparative contours between full set of boundary conditions and partial set.

Table 5-4 Boundary condition influence on DC60.

Probes	Δ DC60 Diffusion Driven Separation	Attached Flow	Shock Driven Separation
full resolution	0.581	0.165	0.310
12 probes	0.533	0.144	0.291
Delta	-0.048	-0.021	-0.019

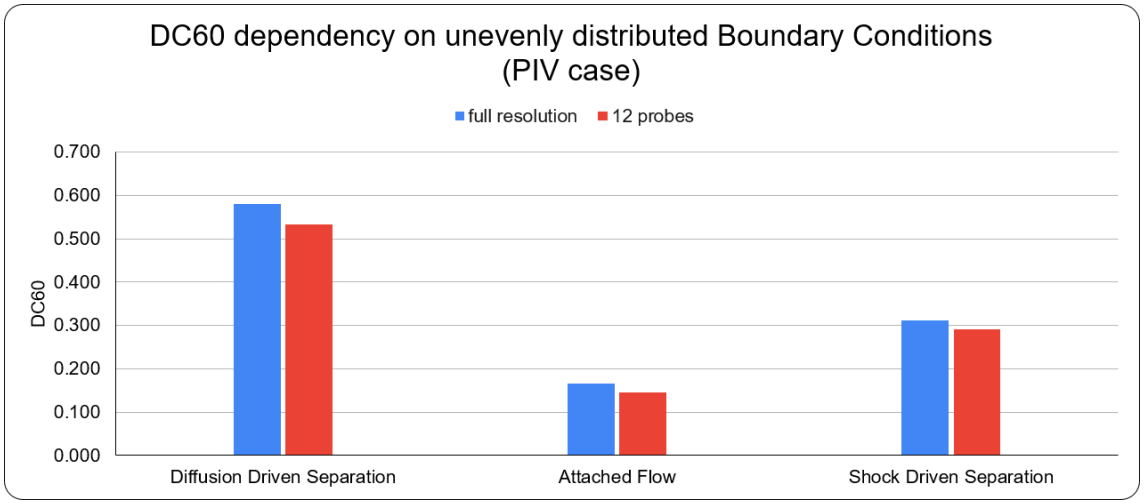


Figure 5-11 Boundary conditions influence on DC60.

5.4 Conclusions Regarding PIV Dataset

The analysis of the experimental S-PIV dataset confirms the trends established during the CFD investigation. The accuracy of the distortion metrics remains dependent on the rake resolution of the measurement array, whereas variations in the radial density have virtually no influence on the final calculated $DC60$. Across all evaluated operative conditions, the reconstructed Distortion Coefficient exhibits a clear, monotonic increase that approaches a stable asymptote as the number of circumferential rakes increases. This directly confirms that highly dense, non-intrusive optical measurements are essential for properly resolving compact aerodynamic phenomena, such as the ingested ground vortex, which are consistently missed or smeared by standard, sparse physical rakes.

The integration algorithm continues to drag boundary pressure deficits radially inward, resulting in a consistent overestimation of the $DC60$ metric in the attached flow and shock driven separation cases. This overestimation proves to be particularly impactful during nominal attached flow conditions, reinforcing the earlier conclusion that the velocimetry reconstruction method can be deceiving in clean flow regimes. However, it remains a highly valuable and conservative diagnostic tool for evaluating off-design aerodynamic phenomena where the physical distortion is massive and the relative mathematical error becomes minimal.

Finally, the experimental dataset demonstrates that the pressure reconstruction remains robust even when the physical boundary conditions are reduced. Using a sparser, unevenly distributed array of boundary static pressure taps introduces only a minor underprediction while maintaining the overall flow topology and relative distortion magnitudes. These empirical findings validate the computational models, proving that pressure from velocimetry reconstruction serves as a practical alternative for evaluating complex intake aerodynamics without the penalties associated with traditional intrusive wind-tunnel instrumentation.

6 CONCLUSIONS

6.1 Summary of Findings

This research evaluated pressure from velocimetry reconstruction, specifically the Direct Spatial Integration scheme, as an alternative to intrusive pressure rakes for assessing intake-engine aerodynamic compatibility. Based on CFD and S-PIV datasets, several conclusions were established.

First, the standard *8x5* physical rake configuration suffers from spatial aliasing. Physical probes are also susceptible to errors induced by flow angularity, non-parallel alignment between flow vectors and fixed probes introduces inaccuracies. These low-density grids fail to resolve compact aerodynamic structures, such as ingested ground vortices. Relying solely on discrete probes masks flow non-uniformities, leading to an underestimation of peak distortion intensities, measured by $DC60$ and structural forcing indicators like the Harmonic Excitation Index.

In contrast, extracting pressure fields directly from optical data streamlines testing enables faster and more cost-effective campaigns by removing the need for mechanical rakes. This non-intrusive approach resolves the aerodynamic structures that sparse grids miss, providing a conservative assessment of fan blade forcing. However, the DSI scheme introduces an offset into the flowfield topology. Integrating pressure gradients radially inward from the outer casing drags boundary pressure deficits toward the hub, creating non-physical low-pressure wakes that inflate the calculated $DC60$ metric. This overestimation scales with the Mass Flow Capture Ratio, presenting an absolute error delta of approximately 0.07 during diffusion-driven separation, 0.09 in attached flow, and 0.11 during shock-driven separation. Altering the placement of outer boundary condition probes does not mitigate this numerical error. Nonetheless, a low quantity of evenly spaced boundary probes is sufficient to yield diagnostic metrics that meet industrial compliance thresholds.

The diagnostic viability of this methodology depends on the operative regime. In attached flow conditions, where aerodynamic distortion is low, the

numerical offset translates into a high relative error. This artificial inflation risks falsely exceeding certification thresholds, meaning the methodology is not suited for validating attached flow. Instead, its diagnostic value is unlocked in off-design regimes, such as diffusion-driven and shock-driven separations. In these states, testing is more comprehensive because the relative error generated by the DSI offset is smaller compared to the physical distortion present in the flow.

Ultimately, mathematical reconstruction is a targeted diagnostic tool for evaluating off-design aerodynamic phenomena, circumventing the aerodynamic blockage associated with physical instrumentation. This methodology offers a practical proposition for the aerospace industry, enabling agile, economical, and high-resolution engine compatibility assessments.

6.2 Recommendations for Future Research

Building upon the findings of this study, future research should prioritise two main avenues to mature non-intrusive pressure reconstruction techniques. Most importantly the development of advanced spatial integration schemes is required to mitigate the accumulated numerical offset inherent to the current DSI approach. Because the existing algorithm integrates radially inward from the outer casing, numerical errors systematically compound near the hub. Future studies should evaluate bi-directional integration methods. For instance, establishing boundary conditions at both the outer casing and the inner spinner, and integrating simultaneously from both surfaces. This dual-anchored approach would constrain the mathematical domain at both ends, minimising the inward propagation of numerical errors and preventing the artificial drag of boundary pressure deficits.

Second, future research must fundamentally question the continued use of legacy distortion metrics, such as $DC60$, when evaluating high-resolution reconstructed flow fields. $DC60$ inherently relies on spatial area averaging over a 60-degree sector, which smears the detailed aerodynamic phenomena that optical velocimetry captures. Consequently, it lacks the precision necessary to fully leverage high-resolution optical data. Subsequent research should therefore focus on proposing and validating novel, high fidelity metrics that directly quantify the physical flow structures rather than relying on generalised area-averaged calculations.

References

[1] V. Tavares Silva, “Aerodynamic Design and Experimental Investigation of Short Nacelles for Future Turbofan Engines” 2020.

[2] I. Sadrehaghighi, “Aircraft Nacelle Design & Optimization”.

[3] T. Piovesan, “Aerodynamics and Unsteady Flow Distortion in a Short Aero-engine Intake under Crosswind” Jun. 2024.

[4] E. J. Gunn, T. Brandvik, M. J. Wilson, and R.-R. P. M. Lane, “FAN-INTAKE COUPLING WITH CONVENTIONAL AND SHORT INTAKES” 2021. [Online]. Available: http://asmedigitalcollection.asme.org/GT/proceedings-pdf/GT2021/84898/V001T01A003/6757020/v001t01a003-gt2021-58829.pdf

[5] F. Tejero, D. Macmanus, J. Hueso-Rebassa, Y. Frey Marioni, and I. Bousfield, “Aerodynamics of a Short Intake at High Incidence” 2025. [Online]. Available: www.euroturbo.eu

[6] A. Magrini and E. Benini, “Interaction Effects of Fan With Short Aero-Intake: A Multi-Objective Optimization Study with Modeling of Flow Coupling” *J. Eng. Gas Turbine. Power*, pp. 1–15, Jul. 2025, doi: 10.1115/1.4070340.

[7] L. Boscagli, D. MacManus, R. Christie, and C. Sheaf, “Effect of Unsteady Fan-Intake Interaction on Short Intake Design” *J. Eng. Gas Turbine. Power*, vol. 146, no. 3, Mar. 2014, doi: 10.1115/1.4063768.

[8] A. Peters, “Ultra-Short Nacelles for Low Fan Pressure Ratio Propulsors” 2014.

[9] F. Tejero, M. Robinson, D. G. MacManus, and C. Sheaf, “Multi-objective optimisation of short nacelles for high bypass ratio engines” *Aerosp. Sci. Technol.*, vol. 91, pp. 410–421, Aug. 2019, doi: 10.1016/j.ast.2019.02.014.

[10] M. Robinson, D. G. MacManus, R. Christie, C. Sheaf, and N. Grech, “Nacelle design for ultra-high bypass ratio engines with CFD based

optimisation” *Aerosp. Sci. Technol.*, vol. 113, Jun. 2021, doi: 10.1016/j.ast.2020.106191.

[11] S. Zantopp, D. MacManus, and J. Murphy, “Computational and experimental study of intake ground vortices” *Aeronautical Journal*, vol. 114, no. 1162, pp. 769–784, 2010, doi: 10.1017/S0001924000004255.

[12] A. Castillo Pardo, E. Gunn, T. S. Williams, C. Hall, T. Brandvik, and S. Baralon, “Crosswind aerodynamics of low pressure ratio fans” *Journal of the Global Power and Propulsion Society*, vol. 9, pp. 143–159, 2025, doi: 10.33737/jgpps/205782.

[13] V. Y. T. Chennuru, R. Corral, F. Zhao, S. Rodríguez-Blanco, and M. Vahdati, “Impact of Fan Aerodynamics on Inlet Distortion at Crosswind” *J. Turbomach.*, vol. 148, no. 6, Jun. 2026, doi: 10.1115/1.4070233.

[14] T. Piovesan, P. K. Zachos, and D. G. Macmanus, “Total Pressure Distortion Reconstruction Methods from Velocimetry Data within an Aero-engine Intake at Crosswind” 2025. [Online]. Available: www.euroturbo.com

[15] K. U. Kempaiah *et al.*, “High-resolution turbofan intake flow characterization by automated stereoscopic-PIV in an industrial wind tunnel environment” *Meas. Sci. Technol.*, vol. 35, no. 2, Feb. 2024, doi: 10.1088/1361-6501/ad0ea0.

[16] A. F El-Sayed and M. S Emeara, “Aerodynamics of intakes of high bypass ratio (hbpr) turbofan engines” *Int Robot Automat J*, vol. 6, no. 2, pp. 88–97, Jun. 2020, doi: 10.15406/iratj.2020.06.00206.

[17] J. P. Murphy and D. G. MacManus, “Intake ground vortex prediction methods” *J. Aircr.*, vol. 48, no. 1, pp. 23–33, 2011, doi: 10.2514/1.46221.

[18] M. Frascella, “Advanced Analysis Methods for Complex Aerodynamics” 2014.

[19] T. Breuer and N. C. Bissinger, “Basic Principles – Gas Turbine Compatibility – Gas Turbine Aspects” in *Encyclopedia of Aerospace Engineering*, wiley, 2010, pp. 1–12. doi: 10.1002/9780470686652.eae573.

[20] S. Sanchez Villacreses, J. Yao, Y. Yao, and B. Chandra, “Investigation of Microjet Engine Inlet Pressure Distortions at Angled Inflow Velocity Conditions” *Fluids*, vol. 10, no. 2, Feb. 2025, doi: 10.3390/fluids10020049.

[21] U. Doll *et al.*, “Non-intrusive flow diagnostics for unsteady inlet flow distortion measurements in novel aircraft architectures” Apr. 01, 2022, *Elsevier Ltd*. doi: 10.1016/j.paerosci.2022.100810.

[22] F. Auteri *et al.*, “A novel approach for reconstructing pressure from PIV velocity measurements” *Exp. Fluids*, vol. 56, no. 2, pp. 1–16, Feb. 2015, doi: 10.1007/s00348-015-1912-z.

[23] J. J. Charonko, C. V. King, B. L. Smith, and P. P. Vlachos, “Assessment of pressure field calculations from particle image velocimetry measurements” *Meas. Sci. Technol.*, vol. 21, no. 10, 2010, doi: 10.1088/0957-0233/21/10/105401.

[24] J. Zhang *et al.*, “4D Flow MRI Pressure Estimation Using Velocity Measurement-Error-Based Weighted Least-Squares” *IEEE Trans. Med. Imaging*, vol. 39, no. 5, pp. 1668–1680, May 2020, doi: 10.1109/TMI.2019.2954697.

[25] F. Scarano, S. Ghaemi, and S. Probsting, “Data reduction from time-resolved tomographic PIV for unsteady pressure evaluation” in *51st AIAA Aerospace Sciences Meeting including the New Horizons Forum and Aerospace Exposition 2013*, 2013. doi: 10.2514/6.2013-771.

[26] N. Sakib, A. Mychkovsky, J. Wiswall, R. Samaroo, and B. L. Smith, “Effect of the boundary conditions, temporal, and spatial resolution on the pressure from PIV for an oscillating flow” 2021.

[27] P. K. Zachos, M. Frascella, D. G. Macmanus, and D. Gil-Prieto, “Pressure flowfield and inlet flow distortion metrics reconstruction from velocity data”

in *AIAA Journal*, American Institute of Aeronautics and Astronautics Inc., 2017, pp. 2929–2941. doi: 10.2514/1.J055585.

[28] X. Liu and J. R. Moreto, “Error propagation from the PIV-based pressure gradient to the integrated pressure by the omnidirectional integration method” *Meas. Sci. Technol.*, vol. 31, no. 5, 2020, doi: 10.1088/1361-6501/ab6c28.

[29] X. Liu, J. R. Moreto, and S. Siddle-Mitchell, “Instantaneous pressure reconstruction from measured pressure gradient using rotating parallel ray method” in *54th AIAA Aerospace Sciences Meeting*, American Institute of Aeronautics and Astronautics Inc, AIAA, 2016. doi: 10.2514/6.2016-1049.

[30] B. W. Van Oudheusden, “PIV-based pressure measurement” *Meas. Sci. Technol.*, vol. 24, no. 3, 2013, doi: 10.1088/0957-0233/24/3/032001.

[31] B. W. Van Oudheusden, F. Scarano, E. W. M. Roosenboom, E. W. F. Casimiri, and L. J. Souverein, “Evaluation of integral forces and pressure fields from planar velocimetry data for incompressible and compressible flows” *Exp. Fluids*, vol. 43, no. 2–3, pp. 153–162, Aug. 2007, doi: 10.1007/s00348-007-0261-y.

[32] L. Li, J. McClure, G. B. Wright, J. P. Whitehead, J. Wang, and Z. Pan, “Error propagation of direct pressure gradient integration and a Helmholtz–Hodge decomposition-based pressure field reconstruction method for image velocimetry” *Exp. Fluids*, vol. 66, no. 5, May 2025, doi: 10.1007/s00348-025-03991-5.

[33] I. Montenegro, “Pressure Flow Field Reconstruction from Experimental TR-PIV Velocity Data” Cranfield University, 2021.

[34] N. Sakib, Z. Pan, J. T. Wiswall, A. G. Mychkovsky, and B. L. Smith, “Experimental investigation on the effect of boundary conditions and spatial resolution on pressure from PIV for oscillating internal flow” *Exp. Fluids*, vol. 65, no. 3, Mar. 2024, doi: 10.1007/s00348-024-03762-8.

[35] S. Rahgozar, Y. Maciel, and P. Schlatter, “Spatial resolution analysis of planar PIV measurements to characterize vortices in turbulent flows” *Journal of Turbulence Rahgozar˙et˙al˙JOT Journal of Turbulence*, vol. 00, no. 00, pp. 1–44, 2013, doi: 10.1080/14685240YYxxxxxxx.

[36] T. Piovesan, A. Giannouloudis, J. H. Rebassa, M. Migliorini, P. Zachos, and D. Macmanus, “MIDAS: A MODULAR SOFTWARE FOR INTAKE FLOW DISTORTION ANALYSIS” 2026.

[37] “A Methodology for Defining Harmonic Indices of Inlet Total-Pressure Distortion for Use in Forced Response Assessment in Turbomachinery - AIR8458” 2026.

Appendices

Appendix A Ethical approval letter



22 July 2026

Dear Mr Fasano ,

Reference: CURES/28851/2026
Project ID: 30499
Title: Total Pressure Field Reconstruction Methods From Velocimetry Data

Thank you for your application to the Cranfield University Research Ethics System (CURES).

We are pleased to inform you your CURES application, reference CURES/28851/2026 **has been reviewed. You may now proceed with the research activities you have sought approval for.**

If you have any queries, please contact CURES Support.

We wish you every success with your project.

Regards,

CURES Team

Appendix B Complete Pictures

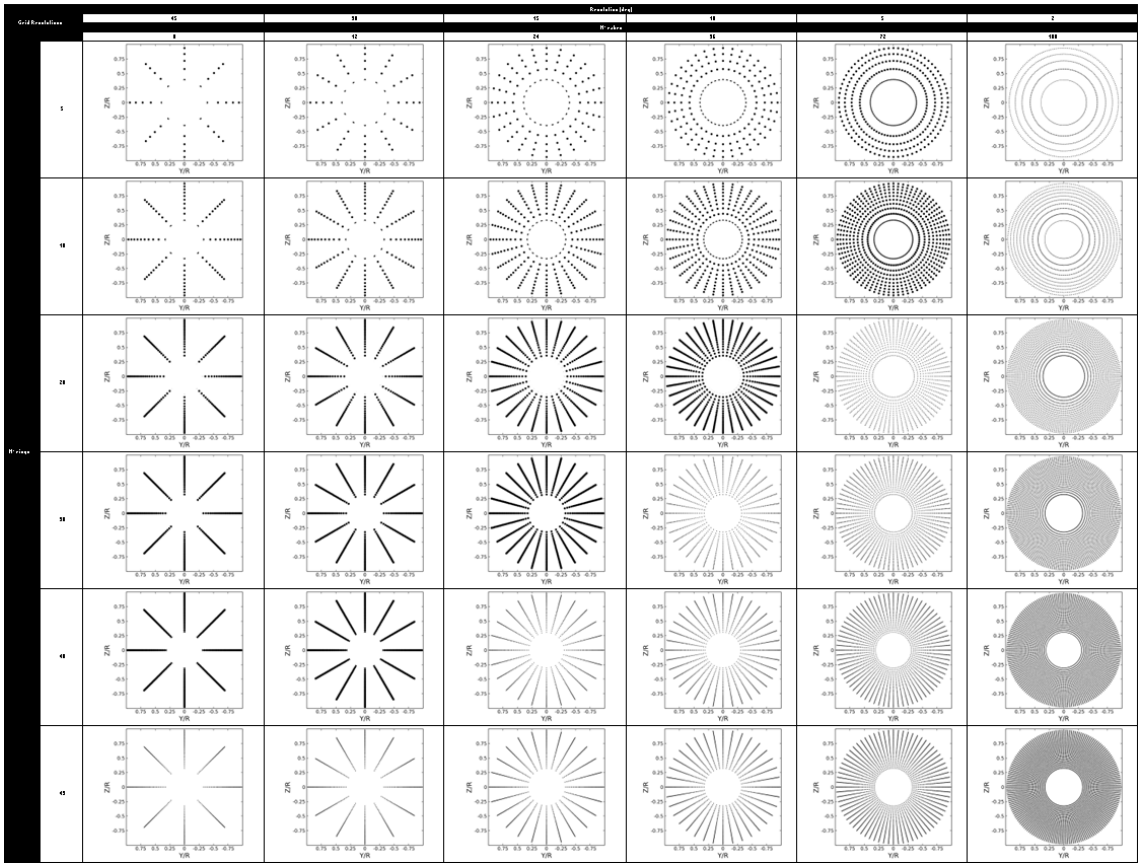


Figure B-1 The complete set of resolutions studied.

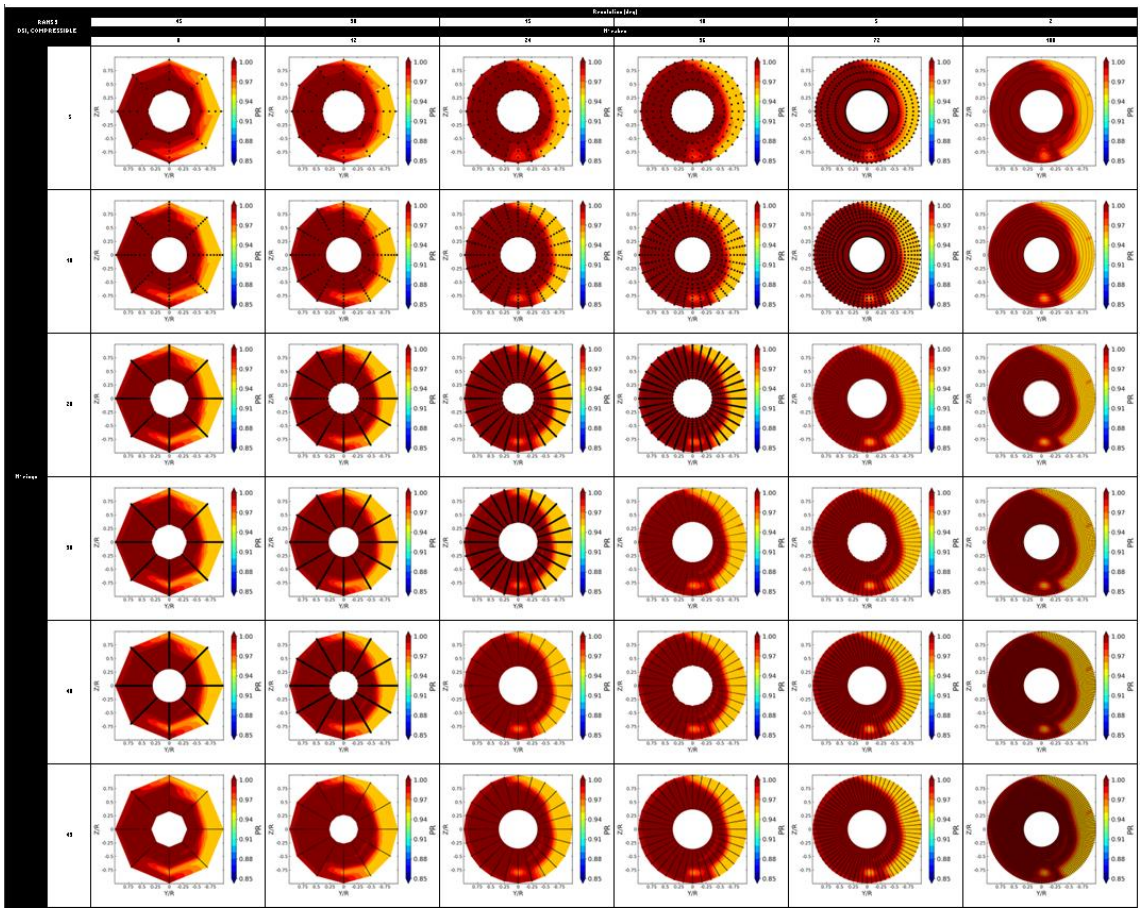


Figure B-2 Full set of CFD ground truth – Diffusion Driven Separation.

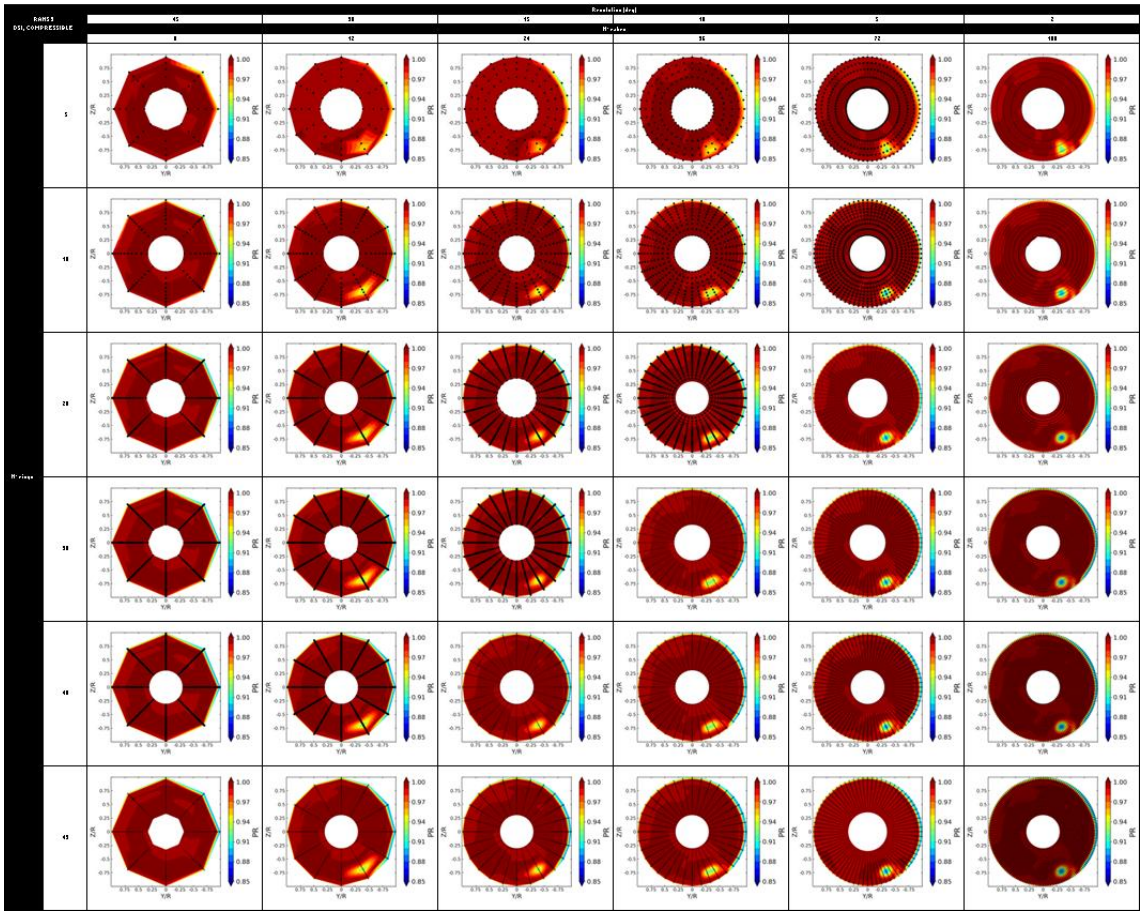


Figure B-3 Full set of CFD ground truth – Attached Flow.

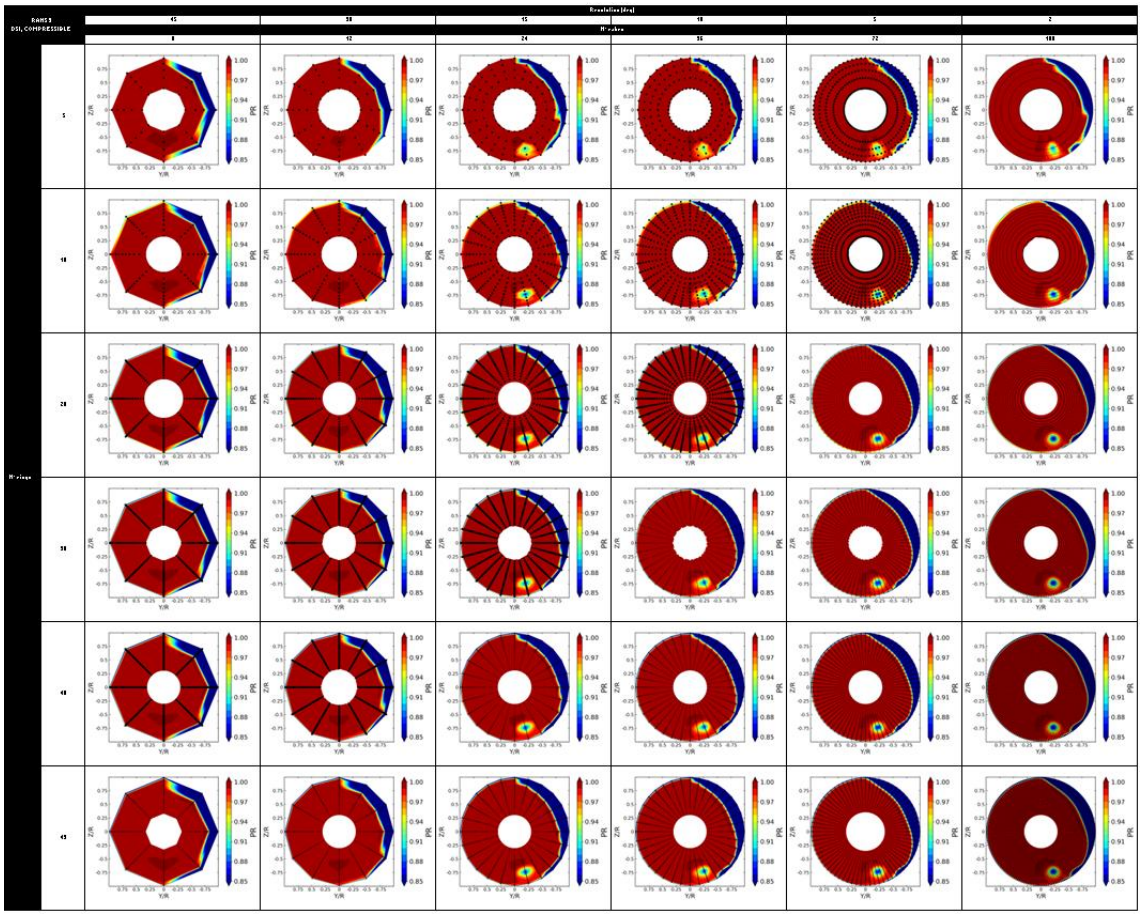


Figure B-4 Full set of CFD ground truth – Shock Driven Separation.

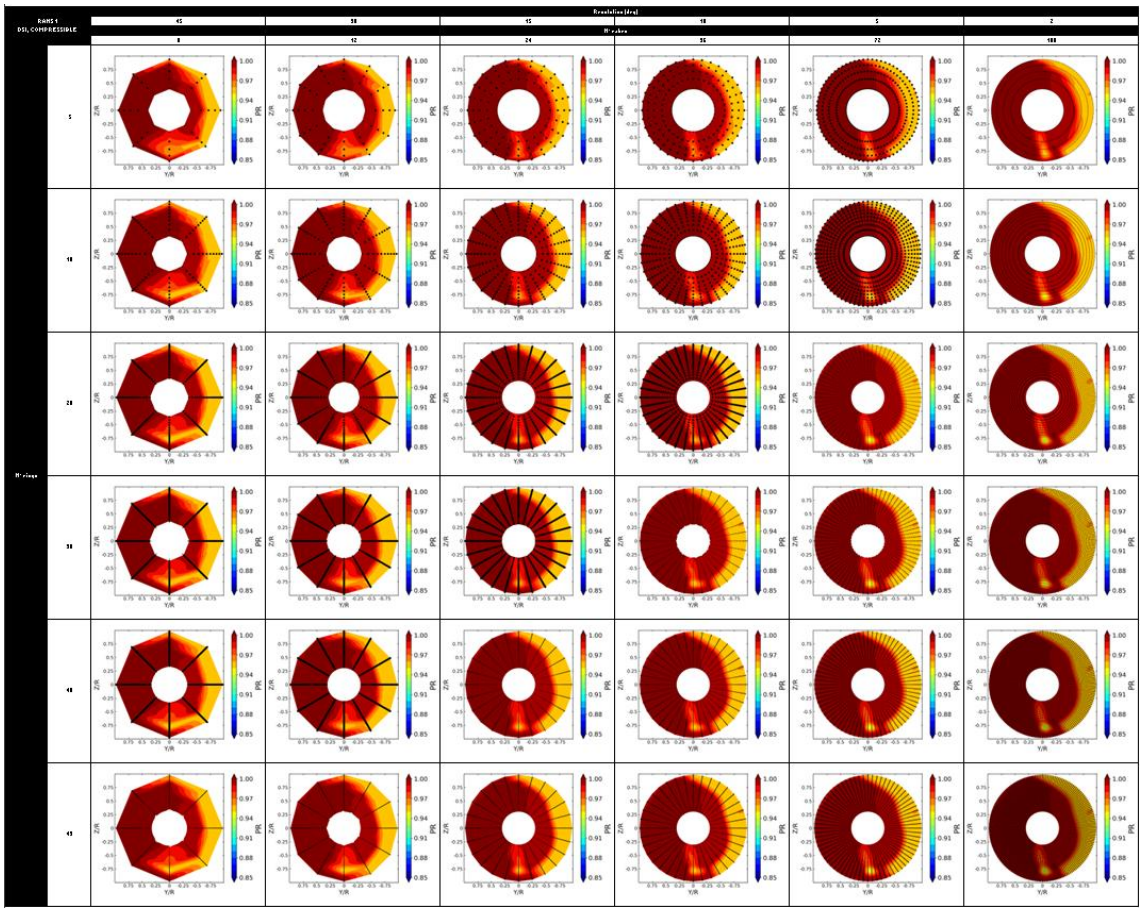


Figure B-5 Full set of CFD reconstructed flowfield – Diffusion Driven Separation.

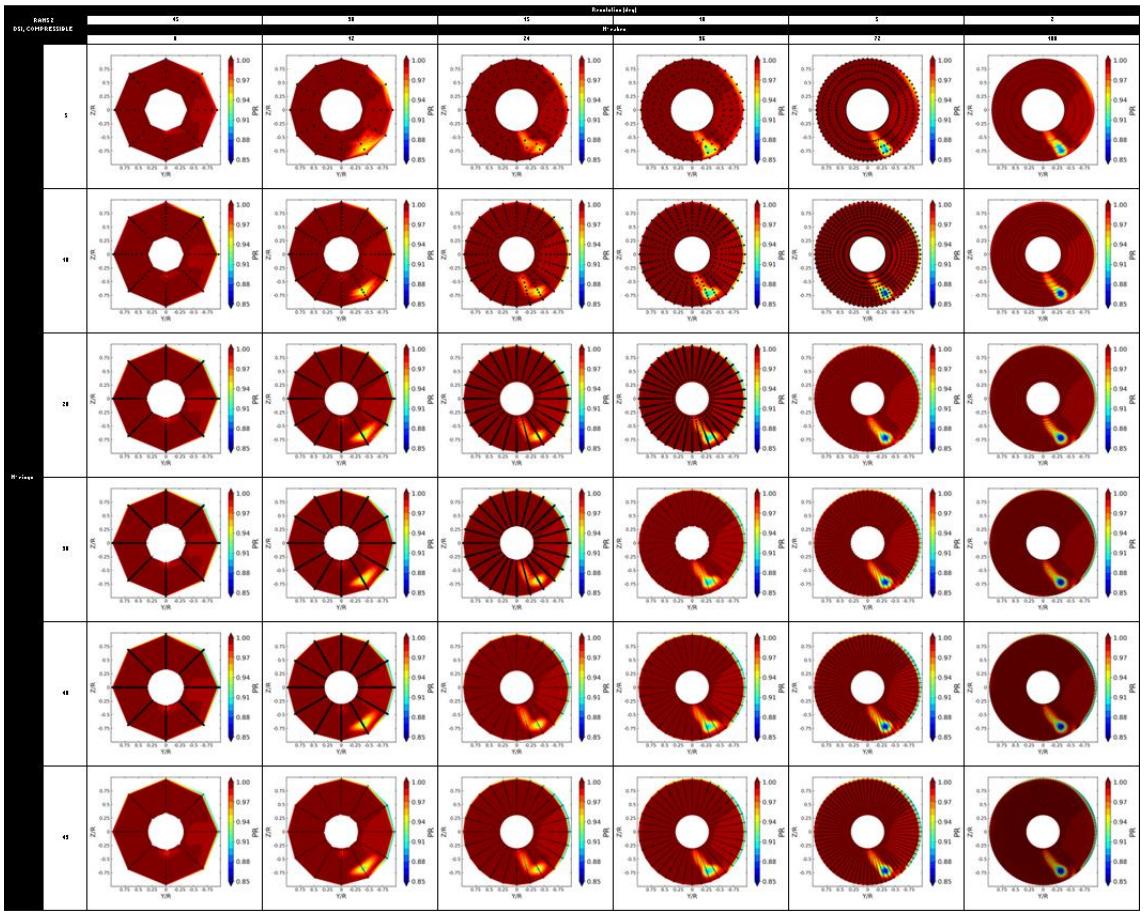


Figure B-6 Full set of CFD reconstructed flowfield – Attached Flow.

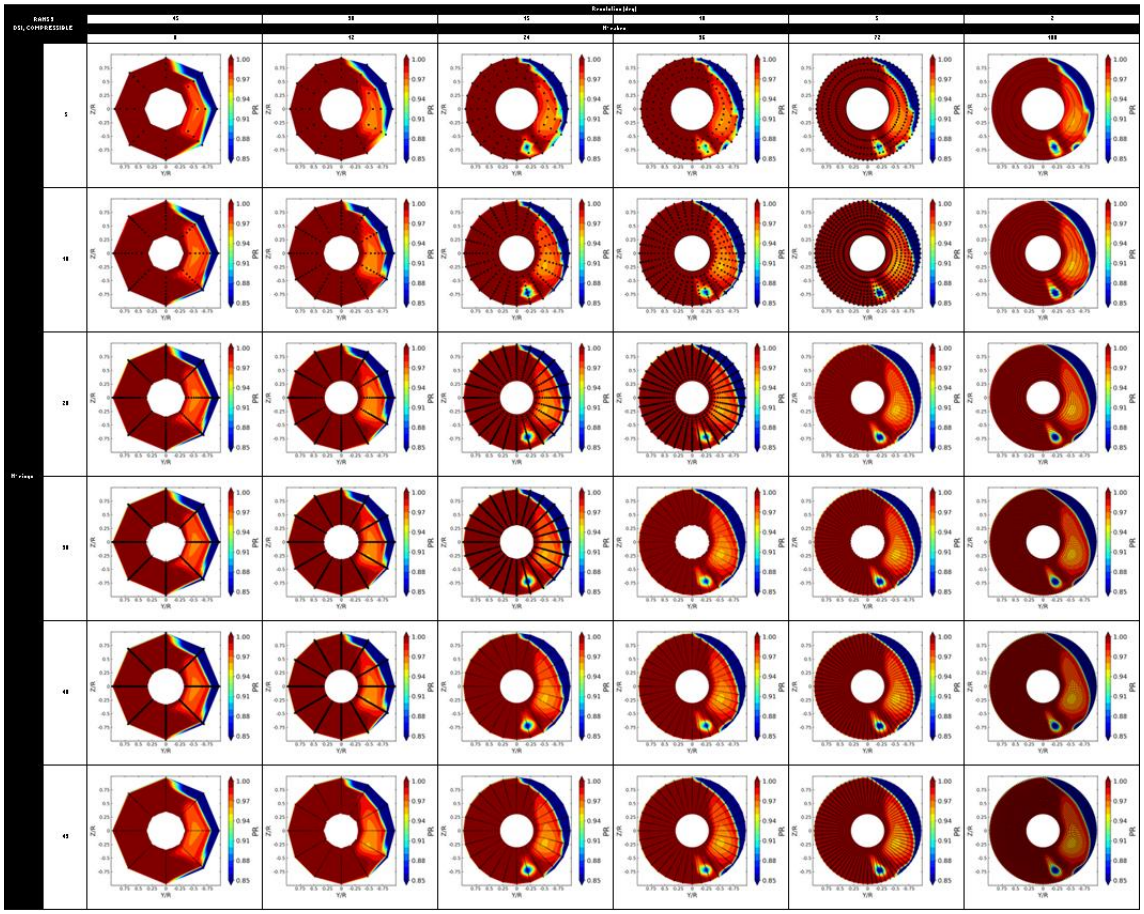


Figure B-7 Full set of CFD reconstructed flowfield – Shock Driven Separation.